RITSUMEIKAN

ISSN 1345−1650

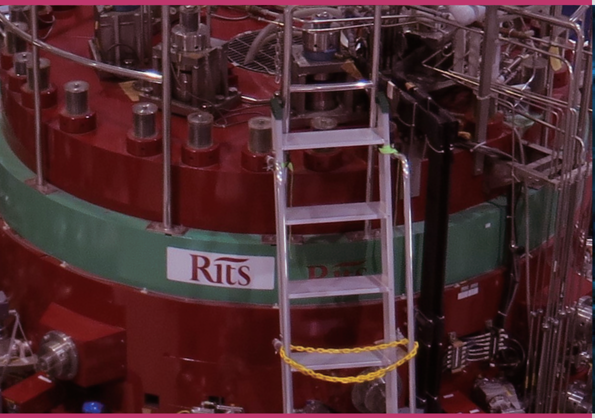

MEMOIRS OF THE SR CENTER

RITSUMEIKAN UNIVERSITY

No.28 Jun 2026

立命館大学
SRセンター紀要

第 28 号

2026 年 6 月

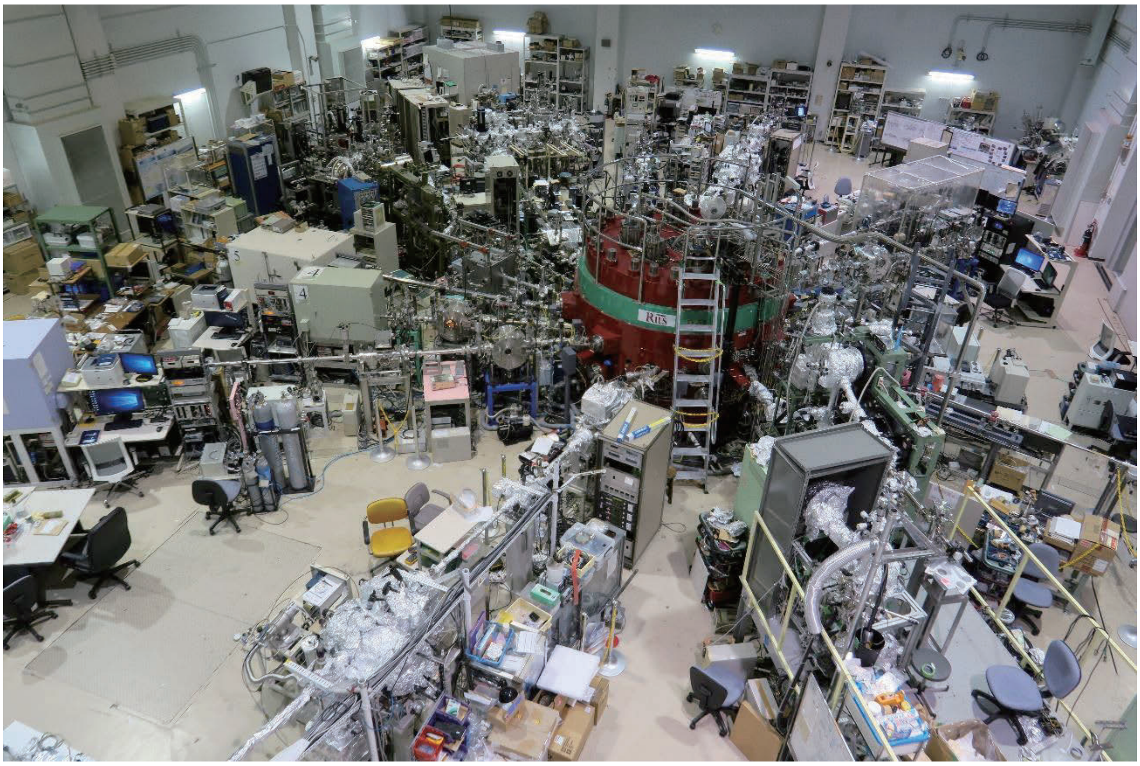

A bird's-eye view of the ring and the beamlines in the SR center.

CONTENTS

PREFACE

RESEARCH ARTICLES

SHORT NOTES

Preface

We are pleased to present our annual report for fiscal year 2025, which summarizes the research activities conducted at the Synchrotron Radiation Center, Ritsumeikan University (RSRC), together with the operational status of the accelerator and beamlines, and a list of publications.

From a historical perspective, fiscal year 2025 may be regarded as the beginning of a challenging period. In addition to persistent inflation, international circumstances further deteriorated, and major countries increasingly prioritized their own national interests. In this context, Aurora, the world's smallest synchrotron radiation storage ring, has now passed 30 years since its relocation to Ritsumeikan University, and issues associated with long-term operation have gradually become more serious. Despite these circumstances, sustained efforts were made by the in-house staff and affiliated faculty members to maximize the activities of the RSRC, and meaningful research outcomes continued to be produced.

The RSRC mainly covers the soft and tender X-ray energy regions. These energy ranges allow X-ray absorption measurements for almost all elements except hydrogen by using K-edges, L-edges, and M-edges, thereby providing essential information for materials science, catalysis, battery research, and environmental studies. Publications were produced using soft X-ray beamlines (BL-2 and BL-11) and tender X-ray beamlines (BL-10 and BL-13). In addition, highly active research in X-ray absorption spectroscopy and imaging using hard X-rays for the K-edge of 3d transition metals was carried out at BL-3 and BL-4, as well as X-ray photoelectron spectroscopy at BL-7. SA-1, a standalone experimental station based on the Al/Cr Kα line, represents another unique activity of the RSRC, where a scanning soft- and hard-X-ray photoemission instrument is installed.

The SR Center continued to support both proprietary and non-proprietary research. The facility was actively utilized not only for academic research and industrial applications, but also for education and training through hands-on synchrotron radiation experiments. On March 23 and 24, 2026, the RSRC hosted students from Ritsumeikan Junior and Senior High School as part of its educational outreach activities.

As synchrotron radiation science continues to play an important role in addressing scientific and societal challenges, the SR Center aims to remain a respected and reliable hub for soft to tender X-ray science and related experimental techniques. We will continue our efforts to contribute to the development of synchrotron radiation science. This issue of the "Memoirs of the Synchrotron Radiation Center, Ritsumeikan University" is intended to help readers understand the activities and potential of the RSRC, and to encourage broader use of our soft and tender X-ray analysis capabilities.

We sincerely welcome comments and suggestions regarding the SR Center, as well as continued visits and use of the facility.

June 2026
Kiyotaka Asakura 朝倉 清高
Director, Synchrotron Radiation Center
Ritsumeikan University

RESEARCH ARTICLES

Chemical State Analysis for Calcination Process of SiO_2-Supported Cr Catalysts

Kakeru Hanano, Hayato Suzuki, and Yasuhiro Inada

Department of Applied Chemistry, Faculty of Life Sciences, Ritsumeikan University, 1-1-1 Noji-Higashi, Kusatsu 525-8577, Japan

The change in the chemical state of the Cr species supported on SiO_2 was analyzed by the XAFS method. It was found that the Cr(III) hydrate was supported on SiO_2 in the early stage of the drying process to prepare the Cr catalyst and that this state was generated regardless of the supported Cr loading. *In situ* XAFS analysis of the transformation processes of the Cr species during the calcination process was carried out under various Cr loadings. The results revealed that the redox behavior of the Cr species strongly depends on the Cr loading amount. A single CrO_3 phase was formed at 500–600 °C at a low loading of 3 wt%, followed by the reduction at higher temperatures. As the Cr loading increased, the fraction of the formed CrO_3 was suppressed, and instead, the reduction to Cr_2O_3 proceeded at lower temperatures. These results suggest that the conversion temperature from CrO_3 to Cr_2O_3 is determined by the balance between the strong interaction with the supporting material due to the dispersion of the Cr species at the low loading and its bulk aggregation at the high loading.

1. Introduction

Cr-based oxides are widely used as catalysts in various oxidation and dehydrogenation reactions. Supported Cr catalysts play important roles in a wide range of reaction systems, including industrial processes, and their catalytic properties are known to strongly depend on the structure and chemical state of the Cr species [1-3]. In these reaction systems, Cr species in the +2 or +3 oxidation states are thought to exhibit catalytic activity [4]. However, Cr_2O_3 is thermodynamically stable and often catalytically inactive [5]. The active species in Cr-based catalysts have not been fully elucidated, and it is thus essential to clarify the changes in the chemical state of the Cr species during the preparation process to construct high-performance Cr-based catalyst systems.

The chemical state of the Cr species is expected to depend on the precursor and supporting material used, drying temperature and time in the impregnation method, and subsequent calcination conditions. A previous study using XAFS combined with diffuse reflectance spectroscopy, Raman spectroscopy, and temperature-programmed reduction analyses has reported that increasing Cr loading promotes the transformation of isolated chromate into polychromate species and Cr_2O_3 clusters, whereas highly dispersed Cr species are preferentially formed at low Cr loadings [6]. However, these XAFS studies were mainly conducted *ex situ* on calcined or reduced samples, and the chemical state evolution of the Cr species during the calcination process has not been directly observed. In this study, SiO_2-supported Cr catalysts were prepared by varying the amount of Cr loading using an impregnation method with a fixed drying temperature of 50 °C, using chromium(III) nitrate as the Cr precursor and SiO_2 as the supporting material. The obtained samples were characterized via X-ray diffraction (XRD) and X-ray absorption fine structure (XAFS) measurements. The chemical state changes during the calcination process were systematically analyzed via *in situ* XAFS measurements. This study revealed that CrO_3 is formed during the calcination process regardless of the Cr loading, but it is reduced to Cr_2O_3 at high temperatures even in an atmosphere containing O_2, and that the conversion temperature strongly depends on the Cr loading. By understanding the changes in the chemical state of the Cr species caused by Cr loading, it is possible to analyze the relationship with the catalytic activity. This information is fundamental for improving the performance of Cr-based catalysts.

2. Experimental

Sample Preparation

$Cr(NO_3)_3 \cdot 9H_2O$ was purchased from Fujifilm Wako Pure Chemical Corporation. SiO_2 used was JRC-SIO-10 distributed by the Catalysis Society of Japan as a reference catalyst with a specific surface area and pore volume of 200 m^2/g and 1.0 cm^3/g, respectively. SiO_2 powder was added to an aqueous solution of $Cr(NO_3)_3 \cdot 9H_2O$, which was acidified with HNO_3, and the mixture was stirred at room temperature. The concentration of the aqueous solution was adjusted to achieve Cr loadings of 3, 5, 10, and 20 wt%. The resulting suspension was dried in air at 50 °C for 72–96 h.

The samples used for Cr loading analysis were calcined under a flow of 10 vol% O_2 diluted with Ar at a heating rate of 10 °C/min. The final temperature was 500 °C for the 3 wt% sample and 1000 °C for the samples with higher loadings (5, 10, and 20 wt%).

Characterization

XRD measurements were performed using an Ultima IV diffractometer (Rigaku) with Cu Kα radiation. The diffraction intensities were recorded in the 2*θ* range of 10°–80°. The Cr loading was determined by X-ray fluorescence (XRF) analysis using a Supermini fluorescent X-ray spectrometer (Rigaku). A calibration curve was constructed using prepared samples in which known amounts of Cr_2O_3 or CrO_3 were physically mixed with SiO_2. CrO_3 was used as the standard for the 3 wt% sample considering its calcination temperature of 500 °C, whereas Cr_2O_3 was used for samples with higher loadings (5, 10, and 20 wt%) because the calcination temperature was 1000 °C.

In Situ XAFS Measurements

In situ XAFS measurements at the Cr K edge were carried out for the calcination processes in the transmission mode at BL-3 of the SR Center (Ritsumeikan Univ.). They were performed under an O_2 gas flow diluted with He at the total flow rate of 100 cm^3/min. The O_2 content in the gas environment was fixed at 10 vol%. The heating rate was 10 °C/min, and the temperature was maintained by stopping the heating during XAFS scans. The amount of sample required for the XAFS measurements was estimated based on the absorption coefficient and filled into a quartz glass ring with an inner diameter of 7 mm. The ring was then placed in a flow-type *in situ* XAFS cell.

The background absorptions in the pre- and post-edge regions of the X-ray absorption near edge structure (XANES) spectrum were calculated using the Athena code [7]. The background absorptions were subtracted from the observed data, and the normalized XANES spectrum was obtained by dividing using the absorption edge jump. The linear combination fitting (LCF) analysis was performed using the normalized XANES spectrum to determine the sample composition.

3. Results and Discussion

3.1. Chemical State of Dried Sample

Figure 1 shows the XRD patterns of the samples dried at 50 °C with different Cr loadings. In all samples, no diffraction lines originating from Cr species were observed, suggesting that the Cr species existed in an amorphous or highly dispersed state.

The XANES spectra of these samples at the Cr K edge are shown in Fig. 2. The white line peak at 6.007 keV is characteristic of Cr(III) hydrate, indicating that it is loaded as a similar hydrate in all samples, regardless of Cr loading. Drying at 50 °C resulted in Cr(III) hydrate being supported on SiO_2 with nitrate ions acting as counterions.

The loading amounts of the four prepared samples were determined using the XRF analysis. The calibration curves obtained by plotting the X-ray fluorescence intensity against the Cr content of the standard samples (CrO_3 and Cr_2O_3) are shown in Fig. 3(A) for the 3 wt% sample and in Fig. 3(B) for the other samples. Based on the observed X-ray fluorescence intensity of the prepared samples, the Cr loadings were determined to be 2.5, 5.6, 9.0, and 22.6 wt%, which are in reasonable agreement with the expected values.

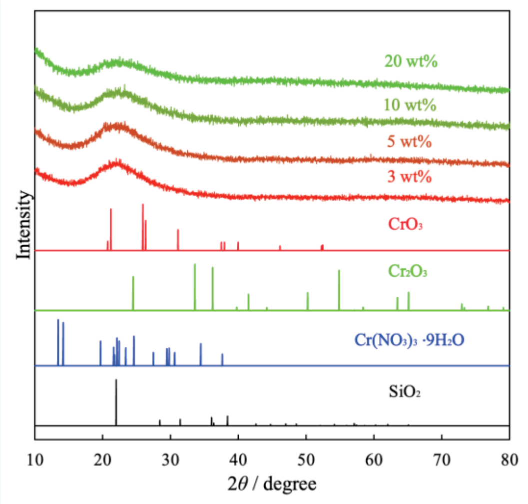

Fig. 1 XRD patterns of SiO_2-supported Cr catalysts dried at 50 °C with different Cr loadings.

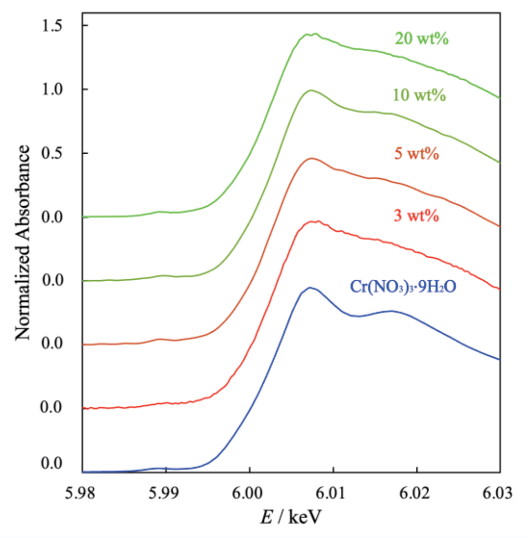

Fig. 2 XANES spectra of SiO_2-supported samples with different Cr loadings.

3.2. Changes in Cr Species during Calcination Process under an Oxygen Atmosphere

Figure 4(A) shows the XANES spectral change during the calcination process under a flow of 10 vol% O_2 diluted with He for the sample with a Cr loading of 2.5 wt%. The intensity of the pre-edge peak at 5.992 keV markedly increased above 140 °C, accompanied by a shift of the absorption edge to the higher energy side. The spectra at 420–560 °C were consistent with that of CrO_3, indicating that the supported Cr(III) hydrate with nitrate ions was oxidized to Cr(VI) during the calcination process.

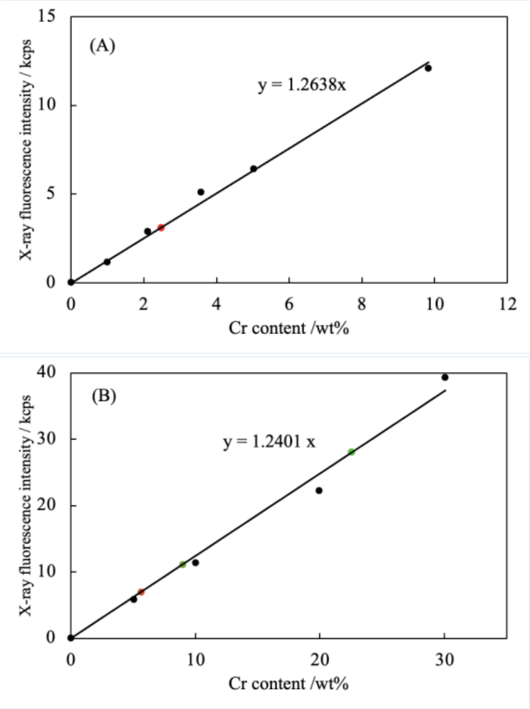

Fig. 3 Results of the XRF measurement based on the calibration curves depicted in (A) and (B).

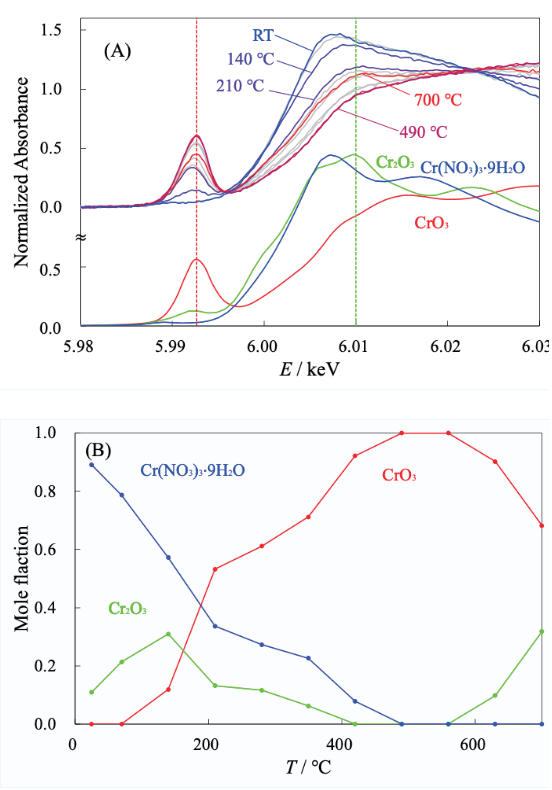

Fig. 4 Change in the XANES spectrum (A) and the mole fraction of the Cr species (B) during the calcination process for the sample with a Cr loading of 2.5 wt%.

Upon further heating to 700 °C, the pre-edge peak intensity decreased slightly, and the absorption edge shifted to the lower energy side, suggesting partial reduction.

The mole fraction of the Cr species was determined using linear combination fitting (LCF) analysis of the observed XANES spectra. In this study, the spectra of $Cr(NO_3)_3 \cdot 9H_2O$, CrO_3, and Cr_2O_3 were used as the standards for the LCF analysis. The determined mole fractions are plotted as a function of temperature in Fig. 4(B). The fraction of CrO_3 exceeded 90% at 420 °C, and a single CrO_3 phase was formed in the temperature range of 490–560 °C. The spectrum at 700 °C shows the coexistence of CrO_3 and Cr_2O_3, suggesting that some CrO_3 was reduced even under an O_2 atmosphere. When the conversion temperature (T_C) is defined as the temperature at which equal amounts of CrO_3 and Cr_2O_3 are present, no such temperature was observed up to 700 °C, whereas the plot in Fig. 4(B) suggests that T_C is located at approximately 750 °C.

The results of a similar *in situ* XAFS analysis are shown in Fig. 5 for the sample with a Cr loading of 5.6 wt%. The pre-edge peak intensity at 5.992 keV increased significantly above 150 °C, and Cr(III) hydrate with nitrate ions was oxidized to CrO_3,

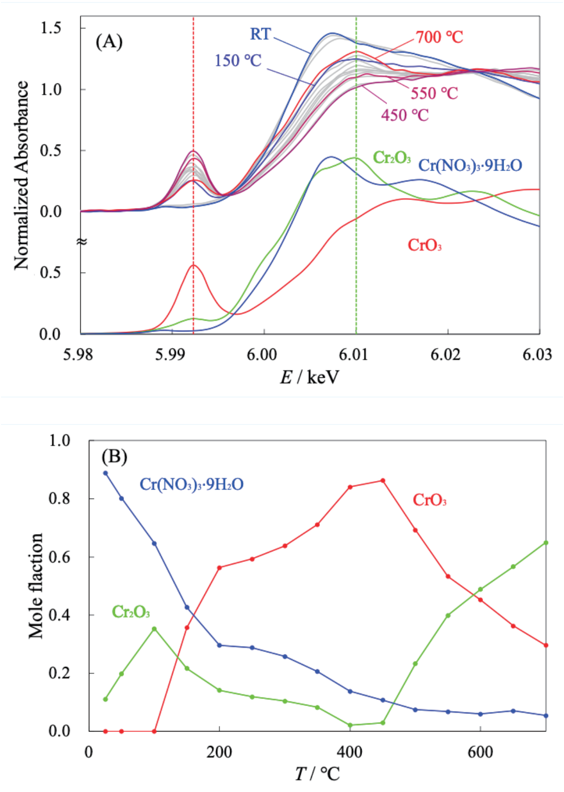

Fig. 5 Change in the XANES spectrum (A) and the mole fraction of the Cr species (B) during the calcination process for the sample with a Cr loading of 5.6 wt%.

similar to that observed at 2.5 wt%. However, the LCF analysis revealed that the maximum proportion of CrO_3 at 450 °C was 86%, indicating that a single CrO_3 phase was not formed and that the reduction reaction to Cr_2O_3 was promoted. At 700 °C, the proportion of Cr_2O_3 reached 60%, and the T_C value was determined to be 590 °C.

Similar results were obtained for the calcination process of samples with Cr loadings of 9.0 and 22.6 wt% as shown in Figs. 6 and 7, respectively. It is common for the nitrate salt of Cr(III) hydrate to be oxidized to CrO_3 at temperatures above 150 °C, and within the range of Cr loadings in this study, the temperature of this oxidation process is constant regardless of the Cr loading. Similarly, CrO_3 was reduced to Cr_2O_3 during further heating; however, the spectrum at 700 °C showed very good agreement with that of Cr_2O_3, and the LCF analyses ind icated that the Cr_2O_3 content exceeded 90% in both cases. This is explained by the lower shift of T_C with increasing Cr loading, and the T_C values for both the 9.0 and 22.6 wt% samples were determined to be 450 °C.

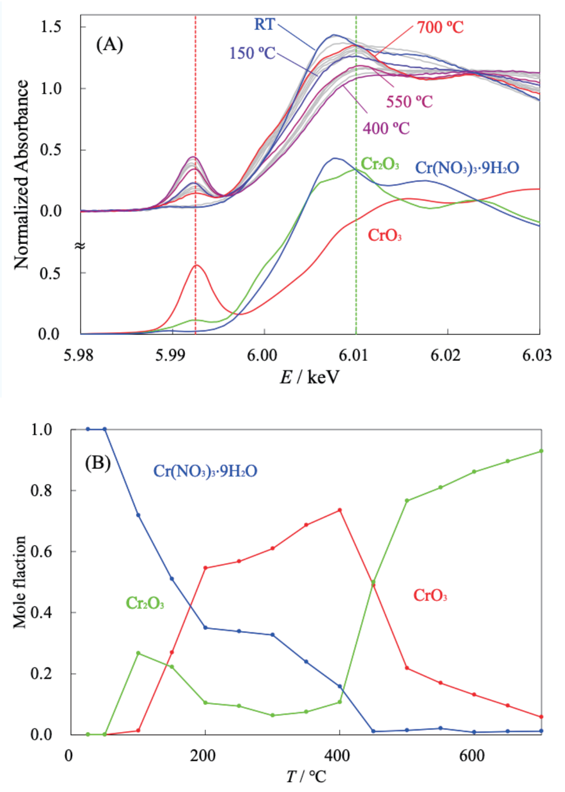

Fig. 6 Change in the XANES spectrum (A) and the mole fraction of the Cr species (B) during the calcination process for the sample with a Cr loading of 9.0 wt%.

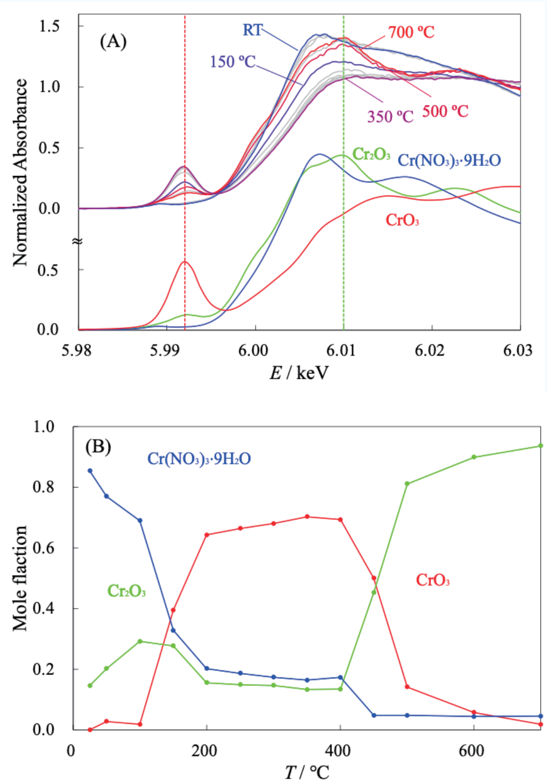

Fig. 7 Change in the XANES spectrum (A) and the mole fraction of the Cr species (B) during the calcination process for the sample with a Cr loading of 22.6 wt%.

3.3. Relationship between Cr loading amount and conversion temperature

In this study, the values of T_C for the reduction from CrO_3 to Cr_2O_3 was determined by *in situ* XAFS analysis under conditions where the Cr loading was varied in the range of 2.5–22.6 wt%. The estimated values of T_C are plotted in Fig. 8 as a function of the Cr loading. As mentioned earlier, the T_C value shifted towards lower temperatures in relation to the amount

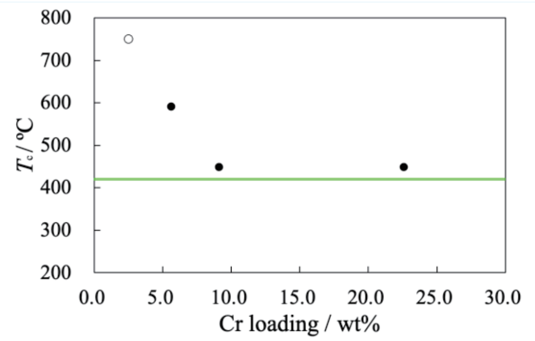

Fig. 8 Conversion temperature for the reduction of CrO_3 to Cr_2O_3 as a function of Cr loading. The value at 2.5 wt% is the predicted value based on Fig. 4. The green line represents the value for bulk oxide.

of Cr loading, up to 10 wt%, converging to *ca.* 450 °C.

It has been reported via the thermogravimetric analysis of bulk $Cr(NO_3)_3 \cdot 9H_2O$ that the conversion to oxide species occurs at 420 °C [8]. The Cr species formed in the 200–400 °C range were analyzed to be a mixture of CrO_3 and Cr_2O_3, which is consistent with the results observed in samples with a Cr loading of 5 wt% or more in this study. The fact that the T_C value depends on the amount of Cr loaded on SiO_2, as revealed in this study, suggests that it is related to differences in the dispersion state of the supported Cr particles. When the Cr loading is low, the interaction of the Cr species with the SiO_2 surface is strengthened, and the CrO_3 particles are stabilized by high dispersion; thus, it is interpreted that a larger energy is required for their conversion to Cr_2O_3. In contrast, when the Cr loading increased, the interactions between the Cr species became dominant, leading to decreased dispersion and behavior similar to that of bulk oxides. Consequently, the T_C value approached the conversion temperature for bulk oxides, and its dependence on Cr loading disappeared.

The same changes in the Cr species as those in this study were also observed on γ-Al_2O_3. The processes are the same as those on SiO_2: the initially supported nitrate salt of Cr(III) hydrate is oxidized to CrO_3 and then reduced to Cr_2O_3 upon heating. However, the reduction temperature of CrO_3 to Cr_2O_3 was approximately 100 °C higher on γ-Al_2O_3 than on SiO_2. This indicates that the interaction between CrO_3 particles and the surface of the supporting material affects the reduction reaction of CrO_3. The higher T_C on γ-Al_2O_3 may originate from the stronger interaction between the dispersed CrO_3 species and the γ-Al_2O_3 surface. Based on the dependence of T_C on the Cr loading, as revealed in this study, it is suggested that at low Cr loadings, CrO_3 particles are highly dispersed and strongly interact with the SiO_2 surface.

4. Conclusions

In this study, SiO_2-supported Cr catalysts were prepared by drying at 50 °C using Cr(III) nitrate as a precursor via the impregnation method. *In situ* XAFS analysis of the reduction process from CrO_3 to Cr_2O_3 was performed under conditions where the Cr loading was varied in the range of 2.5–22.6 wt%. The conversion temperature shifted significantly to lower temperatures as the Cr loading increased up to 10 wt%. In contrast, the change in conversion temperature disappeared at Cr loadings above 10 wt%. It was demonstrated that the conversion temperature at high Cr loadings approached the value for bulk oxides, providing important insights into the calcination process of supported Cr oxide catalysts. The results of this study indicate that the conversion temperature is determined by the balance between dispersion due to interaction with the supporting material at low Cr loading and bulk aggregation at high Cr loading. This provides guidance for controlling the chemical state of Cr species by designing the amount of Cr loading.

Acknowledgement

The SiO_2 used as the supporting material was distributed by the Catalysis Society of Japan as a reference catalyst.

References

[1] J. Handzlik, R. Grybos, and F. Tielens, *J. Phys. Chem. C*, **2016**, *120*, 17594.

[2] E. Groppo, C. Lamberti, S. Bordiga, G. Spoto, and A. Zecchna, *Chem. Rev.*, **2005**, *105*, 115.

[3] A. Wegrzyniak, S. Jarczewski, A. Wegrzynowicz, B. Michorczyk, P. Kustrowski, and P. Michorczyk, *Nanomaterials*, **2017**, *7*, 249.

[4] P. Michorczyk, J. Ogonowski, and K. Zenczak, *J. Mol. Catal. A: Chem.*, **2011**, *349*, 1.

[5] M. S. Kumar, N. Hammer, M. Ronning, A. Holmen, D. Chen, J. C. Walmsley, and G. Oye, *J. Catal.*, **2009**, *261*, 116.

[6] B. M. Weckhuysen, R. A. Schoonheydt, J. M. Jehng, I. E. Wachs, S. J. Cho, R. Ryoo, S. Kijlstra, and E. Poels, *J. Chem. Soc., Faraday Trans.*, **1995**, *91*, 3245.

[7] B. Ravel and M. Newville, *J. Synchrotron Rad.*, **2005**, *12*, 537.

[8] L. Gubrynowicz and T. Stromich, *Thermochim. Acta,* **1987**, *115*, 137.

Origin of Spectral Distortion in Ni L-edge Fluorescence XAS: Role of Emission Processes Revealed by RIXS-based Simulations

Daisuke Shibata[1]

1) Research Organization of Science & Engineering, Ritsumeikan University, 1-1-1 Noji-Higashi, Kusatsu 525-8577, Japan

Self-absorption effects in fluorescence yield X-ray absorption spectroscopy (FY-XAS) often cause spectral distortion when measuring transition-metal L edges. In this study, I investigated the self-absorption effect in partial fluorescence yield X-ray absorption spectroscopy (PFY-XAS) using NiO as a model system. Experimental PFY-XAS spectra were compared with simulations based on analytical models and calculations derived from resonant inelastic X-ray scattering (RIXS) spectra. I demonstrate that the spectral distortion observed in PFY-XAS using 2p–3d fluorescence originates from the difference between the absorption coefficient and the fluorescence emission spectrum. The self-absorbed PFY-XAS spectra can be reproduced by incorporating the energy distribution of emitted fluorescence obtained from RIXS calculations. Furthermore, simulations using the voxel method reveal the particle-size dependence of the self-absorption effect in powder samples. In contrast, PFY-XAS using 2p–3s fluorescence closely reflects the absorption coefficient and allows straightforward correction of self-absorption. These results clarify the origin of spectral distortion in PFY-XAS and provide guidelines for quantitative analysis of L-edge XAS spectra.

1. Introduction

3d transition-metal elements such as Mn, Fe, Ni, Cu possess partially filled 3d orbitals and therefore exhibit rich electronic and magnetic properties, which arise from the additional freedom of spin and orbital configurations of 3d electrons. Theorettical approaches are blocked by the dual nature of 3d electron i.e., itineracy and localization. L-edge X-ray absorption spectra (XAS) of 3d transition metals can directly monitor the unoccupied electronic state with its element and orbital selective information [1,2]. The L-edge XAS of 3d transition element is located at the soft-X-ray region (mainly less than 1000 eV), a conventional transmission mode measurement in air is not available. Instead, total electron yield (TEY) or partial fluorescence yield (PFY) is often used. The TEY method is affected by surface impurity and charge up of the sample. On the other hand, the PFY method provides the bulk information of the sample though the PFY gives distorted spectra due to the self-absorption (over absorption) effect if the sample is concentrated [3,4]. For the flat surface sample, analytical formula can be applied as shown in eq. (1).

$$I_f = \frac{k_X I_0 \mu_X(E)}{\mu_{tot}(E) + \mu_{tot}(E_f)\frac{\sin\alpha}{\sin\gamma}} \times \left(1 - \exp\left(-\frac{\mu_{tot}(E)}{\sin\alpha}d - \frac{\mu_{tot}(E_f)}{\sin\gamma}d\right)\right) \tag{1}$$

k_X,I_0,μ_X,$\mu_{tot}(E)$,$\mu_{tot}(E_f)$,α,γ and d are branching ratio between fluorescence and Auger processes, incident X-ray intensity, absorption coefficient of the absorbing element, total absorption coefficient at the fluorescence energy, grazing angle of incidence and emission, and sample thickness respectively. The total absorption coefficient can be expressed as $\mu_{tot}(E) = \mu_X(E) + \mu_{BG}(E)$ where $\mu_{BG}(E)$ represents the background absorption coefficient from other elements. To overcome the self-absorption, the inverse partial fluorescence yield (IPFY) method was proposed [5]. When X-rays are incident on a material, not only the target element but also other elements in the sample emit fluorescence if their absorption edges lie below the incident photon energy. The fluorescence intensity of these coexisting elements is proportional to the transmitted X-ray intensity and therefore reflects the attenuation of the incident beam caused by self-absorption. In this way, IPFY provides spectra that are essentially free from self-absorption distortions. Nevertheless, the IPFY method cannot be applied when suitable coexisting elements are absent. In such cases, conventional fluorescence-yield measurements must be used and the self-absorption effect cannot be avoided.

I have proposed a new self-absorption correction method for the correction of powder, called a Voxel method which I have demonstrated to work well in the O K-edge of powder [6]. However, when either flat-surface method or Voxel method was applied to the PFY -XAS of Ni L-edge spectra of NiO thin film, the PFY-XAS could not well be corrected. Figure 1 shows the measured PFY-XAS of NiO thin film with different incident angles and the simulated PFY-XAS calculated based on the TEY-XAS spectra. They showed much different spectra and angular dependence. In the normal incidence the large first peak with well-separated second peak appears while in the grazing incidence, the second peak becomes larger than the first one. The simulated PFY based on the TEY-XAS had a strong peak with a small high energy shoulder which exhibited a similar angular dependency to the experimental PFY-XAS but the first peak intensity never becomes smaller than that of the second shoulder.

In this study, I therefore re-examine the mechanism of self-absorption at the L absorption edge and investigate how it can be simulated.

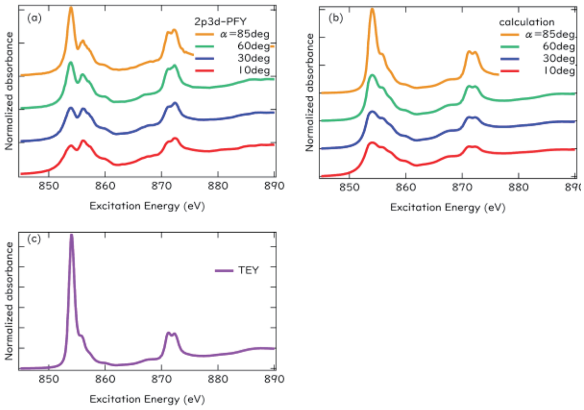

Fig. 1 (a) Experimental PFY-XAS spectrum of a 250-nm-thick NiO thin film measured using 2p–3d fluorescence.
(b) Simulated PFY-XAS spectrum including self-absorption effects calculated from the TEY-XAS absorption coefficient using the flat-surface model.
(c) TEY-XAS spectrum used as the reference absorption coefficient.

2. Experimental and Analysis

2.1 Experimental

XAS measurements were carried out at BL-11 of the SR Center at Ritsumeikan University.

The incident X-ray beam was monochromatized using a varied line-space grating with 1200 lines/mm, and the beam was focused by a toroidal mirror. Total electron yield (TEY) signals were measured through the sample current, while partial fluorescence yield (PFY) signals were detected using a silicon drift detector (SDD) manufactured by TechnoAP. The active area of the SDD detector was 50 mm², and the distance between the sample and the detector was approximately 25 mm. Because the SDD was positioned perpendicular to the incident beam direction, the emission angle γ is given by $\gamma = 90° - \alpha$ where α denotes the incident grazing angle.

The sample used in this study was a NiO thin film with a thickness of 250 nm deposited on a Si substrate. The obtained spectra were processed using the Athena software package [7], where background subtraction and normalization were performed.

2.2 X-ray absorption and emission

When X-rays with energy corresponding to the L absorption edge of a 3d transition metal are incident on a material, a 2p core hole is first created and an electron is excited to an unoccupied state. This process corresponds to the primary absorption process measured by XAS and is represented as follows:

$$\mu \propto \sum_{f} |\langle f|T_a|g\rangle|^2 \delta\left(E_f - E_g - \omega\right) \quad (2)$$

where g, and f denote the ground and final states, ω and E are incident photon energy and system energy, T is transition operator, respectively.
Subsequently, the core hole is filled by electrons from higher energy levels, and fluorescence photons are emitted according to the energy difference between the states. Figure 2 schematically illustrates the electronic transitions responsible for fluorescence emission. Figure 2(a) corresponds to the 3d → 2p transition, while Fig. 2(b) represents the 3s → 2p transition. In PFY measurements of the L edge of 3d transition metals, several fluorescence channels can be observed. Among them, 2p–3d fluorescence and 2p–3s fluorescence are particularly important. Because the intensity of 2p–3d fluorescence is typically the strongest, PFY-XAS measurements often use this channel.

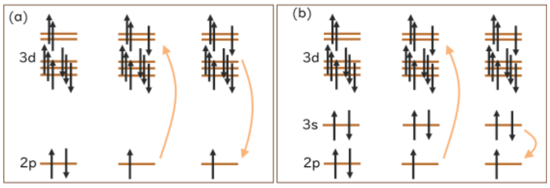

Fig. 2 Schematic illustration of fluorescence processes following L-edge X-ray absorption in transition metals.
(a) 2p–3d fluorescence process, where a 3d electron fills the 2p core hole.
(b) 2p–3s fluorescence process, where a 3s electron decays to the 2p core level.

In 2p-3d PFY-XAS measurements, the detected fluorescence corresponds to the same physical process measured in resonant inelastic X-ray scattering (RIXS) [8]. Therefore, if the RIXS spectrum is known, the PFY-XAS spectrum can be obtained by integrating the RIXS intensity over the emitted photon energy. The RIXS spectrum can be described by the Kramers–Heisenberg formula

$$F(\Omega,\omega)=\sum_{f}\left|\sum_{m}\frac{\langle f|T_e|m\rangle\langle m|T_a|g\rangle}{\Omega+E_g-E_m-i\Gamma_m}\right|^2 \times\delta\left(\Omega+E_g-\omega-E_f\right) \tag{3}$$

where m denotes intermediate states, Ω is emission photon energy, Γ_m represents the spectral broadening due to the core-hole lifetime in the intermediate state.

2.3 Calculation

When calculating L-edge spectra of 3d transition metals, the multiplet model plays a central role [1]. During X-ray absorption, the electronic configuration changes from $2p^6 3d^n \rightarrow 2p^5 3d^{n+1}$ Because the radial wave functions of the 2p core hole and 3d valence electrons strongly overlap, the Coulomb interaction between them becomes significant. These interactions, which are not fully screened and can exceed the magnitude of spin-orbit coupling in the core shell, produce multiplet splitting and strongly influence the electronic states. Furthermore, the electronic structure of transition-metal ions is affected by crystal-field effects and charge transfer between the metal ion and surrounding ligands. Various computational methods have been developed to evaluate these spectra. These programs can broadly be classified into semi-empirical codes and first-principles codes. Semi-empirical codes determine interaction parameters empirically or experimentally. Examples include the program by Thole et al. [9], Tanaka's program [10], XCLAIM[11], and Quanty[12,13]. Because the number of parameters is limited, these methods are widely used for systems with relatively high symmetry. In contrast, first-principles codes perform calculations based on the atomic structure without relying on empirical parameters. These approaches allow charge-transfer effects from bands to be incorporated naturally but often require a deeper understanding of the underlying computational methods.

In this study, the Ni L-edge spectrum of NiO was calculated using the Quanty program. Ni ions were modeled in O_h symmetry corresponding to a NiO_6 cluster. The parameters used in the spectral calculations were taken from previous studies [10,12,14] (Table 1). The spin configuration of Ni was assumed to be isotropically distributed. NiO has a Néel temperature of 523 K, and at room temperature it exhibits antiferromagnetic order with ferromagnetic alignment within the {111} planes and antiferromagnetic coupling between adjacent planes. However, the magnetic structure within the X-ray beam spot of the thin film is not necessarily uniform. This reflects the fact that there is no guarantee that the magnetic structure on the thin film used in this case will be uniform within the spot range.

Table 1 Parameters from XPS and DFT calculations.

U_{dd}	Δ	U_{pd}	U_{sd}
7.3	4.7	8.5	6.0
V_{e_g}	$V_{t_{2g}}$	$10Dq$	T_{pp}
2.06	1.21	0.56	0.72
ζ_{3d}	$F_{dd}^{(2)}$	$F_{dd}^{(4)}$	ζ_{2p}
0.08	11.14	6.87	11.51
$F_{2p3d}^{(2)}$	$G_{2p3d}^{(1)}$	$G_{2p3d}^{(3)}$	ζ_{3p}
6.67	4.92	2.80	1.40
$F_{3p3d}^{(2)}$	$G_{3p3d}^{(1)}$	$G_{3p3d}^{(3)}$	
12.87	15.89	9.58	

3. Results and Discussion

3.1 calculation using RIXS spectrum

Figure 3 shows the calculated XAS spectrum for the NiO_6 cluster together with the spectrum obtained by the total fluorescence yield (TFY) method. Although the overall shapes are similar, small differences can be observed. This difference arises because XAS spectra are calculated from first-order perturbation processes, whereas fluorescence spectra involve intermediate states.

Figure 4 shows the calculated RIXS spectrum at the Ni L edge according to eq. (3). The vertical axis represents the incident photon energy, and the horizontal axis corresponds to the energy loss.

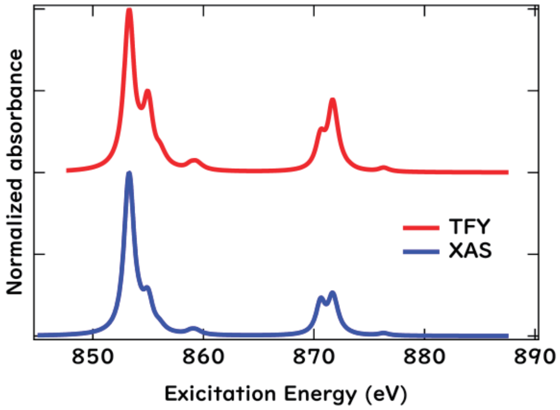

Fig. 3 Calculated spectra of NiO obtained from multiplet calculations using the Quanty program. The XAS spectrum corresponds to the absorption coefficient, while the TFY-XAS spectrum represents the fluorescence yield obtained by integrating all emitted photon energies.

The 2p–3d fluorescence exhibits multiple peak structures with Lorentzian broadening. These structures correspond to elastic scattering and inelastic fluorescence processes and reflect the ligand-field splitting described by the Tanabe–Sugano diagram [15]. By integrating the RIXS intensity along the energy-loss axis, the PFY spectrum can be obtained. The energy loss notation is insufficient because the energy loss must be converted to the energy of the emitted light and the background should be added, which was not considered in the Laurentian broadening process. Figure 5 shows the 2D color map of excitation energy (y axis) and emission energy (x-axis). This spectral map is called $S_X(E,E_f)$ and the equation (1) is modified as follows.

$$I_{PFY} \propto \frac{k_X I_0 S_X(E,E_f)}{\mu_{tot}(E)+\mu_{tot}(E_f)\frac{\sin\alpha}{\sin\gamma}} \times \left(1-\exp\left(-\frac{\mu_{tot}(E)}{\sin\alpha}d-\frac{\mu_{tot}(E_f)}{\sin\gamma}d\right)\right) \tag{4}$$

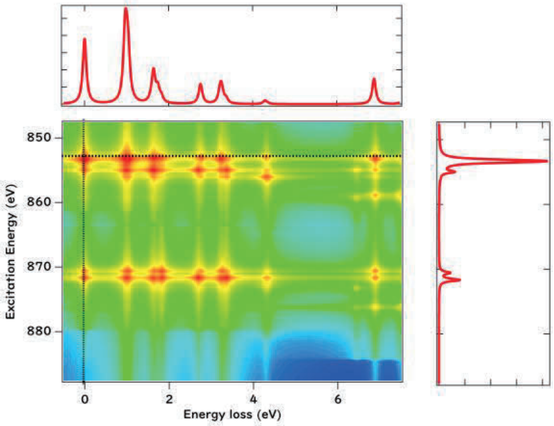

Fig. 4 Calculated RIXS spectrum of the Ni L edge for a NiO₆ cluster.
The vertical axis represents the incident photon energy, and the horizontal axis shows the energy loss (difference between incident and emitted photon energies).

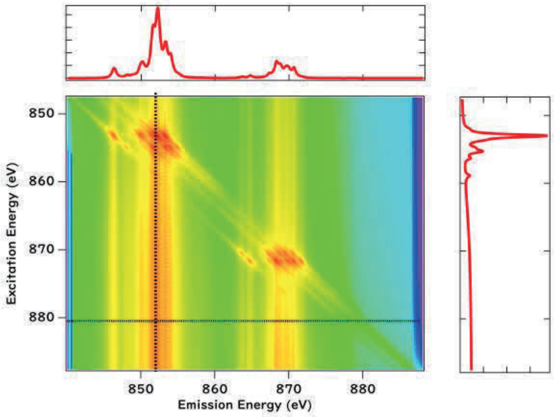

Fig. 5 Fluorescence intensity map derived from the RIXS calculation.
The upper panel and right panel represent line profiles along the dashed lines in the RIXS map.

The resulting simulation spectrum is shown in Fig. 6. The peak structures and the reversal of the relative intensities are successfully reproduced, indicating that the calculation accurately captures the self-absorption mechanism.

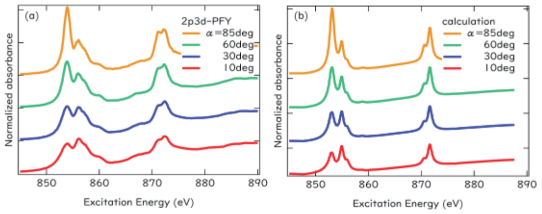

Fig. 6 (a) Experimental PFY-XAS spectrum of NiO measured using 2p–3d fluorescence.
(b) Simulated PFY-XAS spectrum including the energy distribution of emitted fluorescence derived from the RIXS calculation.

3.2 PFY-XAS of NiO power

So far, the analytical solution based on a flat-surface model has been discussed. However, real materials are often in powder form and may have complex shapes. To treat arbitrary geometries, simulations can be performed using the voxel method [6].

Figure 7(a) shows experimental PFY-XAS spectra of NiO powder. Figure 7(b) shows simulations of self-absorption spectra for NiO powder particles with different radii, assuming a single spherical particle. When the particle radius is smaller than about 10 nm, the self-absorption effect becomes weak, and the spectrum approaches the thin-film limit. When the radius exceeds 100 nm, the self-absorption effect saturates and no further change occurs even if the particle size increases. This corresponds to the infinite-thickness limit in the flat-surface model. Powder particle sizes are generally in the μm order, so this limit corresponds to the actual sample and shows good agreement in the relative peak intensities.

Interestingly, the particle-size dependence differs from that observed at the O-K absorption edge [6], where the thin-film limit occurs at approximately 10 nm and the infinite-thickness limit at about 500 nm. This difference originates from the magnitude of the absorption coefficient. At the O-K edge, the maximum absorption coefficient is approximately

μ_{tot} 100000 cm^{-1}, whereas at the Ni L_3 edge it reaches approximately 250000 cm^{-1}. Therefore, self-absorption saturation occurs at smaller particle sizes for the L edge.

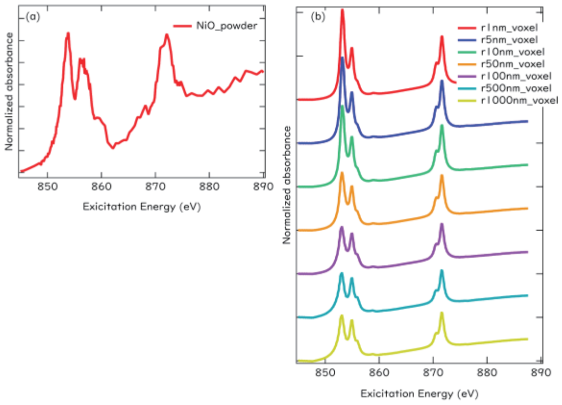

Fig. 7 (a) Experimental PFY-XAS spectrum measured for NiO powder.
(b) Simulated PFY-XAS spectra for spherical NiO particles with different radii, illustrating the particle-size dependence of self-absorption.

3.3 2p-3s fluorescence

So far, I have focused on 2p–3d fluorescence, but 2p–3s fluorescence must also be considered. This fluorescence originates from the transition of an electron from the 3s orbital to a 2p core hole created during X-ray absorption. In 3d transition metals, the emitted photon energy of 2p - 3s is typically 50–130 eV lower than that of 2p–3d fluorescence.

Figure 8(a) shows the energy distribution of fluorescence detected by the SDD. The 2p–3s fluorescence peak appears next to the 2p–3d fluorescence peak of Ni. Although the energy resolution of the SDD is approximately 80 eV, the difference between the two fluorescence energies can still be resolved. By selecting the region of interest (ROI) in the detector:

780–900 eV → 2p–3d fluorescence
600–780 eV → 2p–3s fluorescence

can be measured separately. Unlike 2p–3d fluorescence, 2p–3s fluorescence is not affected by the final state of the $2p^5 3d^{n+1}$ configuration, and its spectral shape is therefore expected to follow the XAS spectrum. Although it is still a two-photon process and can be influenced by polarization effects [16], previous studies have shown that when the fluorescence is fully integrated, the fluorescence spectrum matches the XAS spectrum.

Figure 8(b) shows the fluorescence spectra and XAS spectra calculated using Quanty. The two spectra coincide almost perfectly.

Because the emitted fluorescence energy lies outside the absorption edges, the absorption coefficient does not exhibit strong structures at the emission energy. Therefore, the self-absorption calculation follows the analytical expression given by eq. (1).

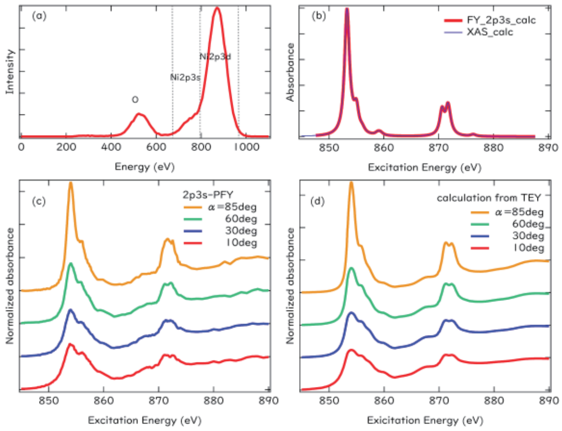

Fig. 8 (a) Energy distribution of emitted fluorescence measured by the SDD detector, showing the separation between 2p–3d and 2p–3s fluorescence.
(b) Comparison between the calculated XAS spectrum and the fluorescence spectrum corresponding to the 2p–3s transition.
(c) Experimental PFY-XAS spectrum measured using 2p–3s fluorescence.
(d) Simulated spectrum obtained from the TEY-XAS absorption coefficient.

Figures 8(c) and 8(d) compare experimental PFY-XAS spectra obtained from 2p–3s fluorescence with simulations based on TEY-XAS spectra. The agreement between experiment and calculation is very good, indicating that the correction of self-absorption is straightforward in this case. However, the drawback of 2p–3s fluorescence is its lower intensity, which requires longer acquisition times to obtain spectra with low noise.

3.4 Discussion

The present results clarify the physical origin of the spectral distortion observed in PFY-XAS at the L edge of transition metals. While self-absorption effects in fluorescence detection have been widely recognized, the present study demonstrates that the conventional analytical description is insufficient for interpreting PFY spectra when the detected fluorescence originates from 2p–3d transitions.

The conventional self-absorption model assumes that the detected fluorescence intensity is directly proportional to the absorption coefficient of the incident photon energy. Under this assumption, the spectral distortion arises solely from the energy dependence of attenuation of the incident X-ray within the sample. The analytical expression derived from this model therefore predicts only a monotonic suppression of spectral intensity and cannot reproduce changes in the relative peak intensities of the absorption features. However, the experimental PFY-XAS spectra of NiO show a clear reversal of the relative peak intensities at the L_3 edge, particularly under grazing-incidence conditions. This behavior cannot be explained within the conventional framework. The present calculations demonstrate that this discrepancy originates from the intrinsic energy dependence of the fluorescence spectrum itself.

In PFY measurements based on 2p–3d fluorescence, the detected signal corresponds to an energy-integrated intensity of the resonant inelastic X-ray scattering process. Consequently, the PFY spectrum reflects not only the absorption coefficient but also the structure of the RIXS spectral distribution. Because the fluorescence spectrum consists of multiple multiplet-derived peaks, the relative contributions of different absorption channels vary with the incident photon energy. Incorporating this energy-dependent fluorescence spectrum into the self-absorption calculation naturally reproduces the experimentally observed peak reversal. These results indicate that the distortion of PFY-XAS spectra arises from two distinct mechanisms:

1. self-absorption
2. multiplet effects

The interplay between these two effects produces the pronounced spectral distortions observed in 2p–3d PFY-XAS. In contrast, PFY spectra based on 2p–3s fluorescence behave very differently. Because the 3s electron is weakly coupled to the 3d valence shell, the final states of the emission process are much less sensitive to the multiplet structure of the intermediate configuration. As a result, the fluorescence spectrum closely follows the absorption coefficient. In this case the PFY intensity can be described accurately by the analytical self-absorption formula, as confirmed by the good agreement between experiment and simulation. The present results therefore indicate an important distinction between primary and secondary optical process.

4. Conclusions

The self-absorption effect at the L absorption edge was investigated experimentally and theoretically using NiO as a model system.

PFY-XAS measurements at the L edge can be performed using either 2p–3d fluorescence or 2p–3s fluorescence. While 2p–3d fluorescence provides strong intensity, its spectral shape is strongly influenced by multiplet effects and experimental geometry, including the incident angle, emission angle, and polarization conditions. The self-absorbed PFY-XAS spectra obtained from 2p–3d fluorescence can be reproduced by calculations based on the RIXS spectrum. These calculations can also be performed using the voxel method to account for realistic particle geometries. For NiO, the self-absorption effect becomes weak when the particle size is about 10 nm, while it saturates when the particle size reaches approximately 200 nm. In contrast, the self-absorbed PFY-XAS spectra obtained from 2p–3s fluorescence can be accurately reproduced using TEY-XAS spectra and the analytical self-absorption formula.

More generally, the present analysis highlights that 2p-3d PFY-XAS should be regarded as a geometry-dependent measurement that reflects both the electronic structure and the photon-transport process inside the material. Accurate interpretation therefore requires unified treatment of electronic excitation processes and photon attenuation effects. The approach developed in this study provides such a framework by combining multiplet-based RIXS calculations with self-absorption simulations.

Because many transition-metal systems are commonly measured using fluorescence detection, these findings have important implications for the interpretation of PFY-XAS spectra in a wide range of materials. In particular, the approach presented here can be extended to other transition-metal oxides and correlated electron systems, where multiplet effects and strong electron interactions play essential roles in determining the spectral line shape.

Acknowledgement

I am very grateful to NIPPON STEEL TECHNOLOGY Co., Ltd. for supplying the sample. I thank T. Ohta and K. Asakura for fruitful discussions.

References

[1] F. M. de Groot, and A. Kotani, Core Level Spectroscopy of Solid, CRC Press, **2008**.

[2] F. de Groot, *Coord. Chem. Rev.*, **2005**, *249*, 31

[3] L. Tröger, D. Arvanitis, K. Baberschke, H. Michaelis, U. Grimm, and E. Zschech, *Phys. Rev. B*, **1992**, *46*, 3283

[4] S. Eisebitt, T. Böske, J. -E. Rubensson, and W. Eberhardt, *Phys. Rev. B*, **1993**, *47*, 14103.

[5] A. J. Achkar, T. Z. Regier, H. Wadati, Y.-J. Kim, H. Zhang, and D. G. Hawthorn, *Phys. Rev. B*, **2011**, *83*, 081106.

[6] D. Shibata, T. Ohta, Y. Orikasa, K. Ito, and K. Asakura, *e-J. Surf. Sci. Nanotech*., **2025**, *23*, 36

[7] B. Ravel, and M. Neville, *J. Synchrotron Rad.*, **2005**, *12*, 537.

[8] L. J. P. Ament, M. van Veenendaal, T. P.

Devereaux, J. P. Hill, and J. van den Brink, *Rev. Mod. Phys.,* **2011**, *83*, 705

[9] B. T. Thole, G. V. D. Laan, J. C. Fuggle, G. A. Sawatzky, R. C. Karntak, and J. -M.Esteva, *Phys. Rev. B*, **1985**, *32*, 5107.

[10] A. Tanaka, and T. Jo, *J. Phys. Soc. Jpn.*, **1994**, *63* 2788.

[11] J. Fernández-Rodríguez, B. Toby, and M. van Veenendaal, *J. Electron Spectros. Relat. Phenomena,* **2015**, *202*, 81.

[12] M. W. Haverkort, M. Zwierzycki, and O. K. Andersen, *Phys. Rev. B*, **2012**, *85*, 1.

[13] M. W. Haverkort, *J. Phys. Conf. Ser.,* **2016**, *712*, 012001.

[14] A. E. Bocquet, T. Mizokawa, K. Morikawa, A. Fujimori, S. R. Barman, K. Maiti, D. Sarma, Y. Tokura and M. Onoda, *Phys. Rev. B*, **1996**, *53*, 1161.

[15] H. Kamimura, S. Sugano, and Y. Tanabe, Ligand Field Theory and Its Applications, Shokabo Co., Ltd., **1969**.

[16] S. Imada, and F. M. de Groot, *J. Electron Spectros. Relat. Phenomena*, **2025**, *280*, 147538.

P K-edge XAS Study of Thermally Degraded $LiPF_6$ Electrolyte Solutions in Ethylene Carbonate–Ethyl Methyl Carbonate Solvent

Yuta Shiomi[1], Takeru Hamada[1], Akinori Irizawa[2], Keiji Shimoda[3], Chengchao Zhong[1], Ken-ichi Okazaki[2] and Yuki Orikasa[1]

1) Department of Applied Chemistry, Ritsumeikan University, 1-1-1 Noji-Higashi, Kusatsu 525-8577, Japan

2) Research Organization of Science and Technology, Ritsumeikan University, 1-1-1 Noji-Higashi, Kusatsu 525-8577, Japan

3) Ritsumeikan Global Innovation Research Organization, Ritsumeikan University, 1-1-1 Noji-Higashi, Kusatsu 525-8577, Japan

P K-edge X-ray absorption near-edge structure (XANES) measurements of liquid $LiPF_6$/ethylene carbonate (EC)–ethyl methyl carbonate (EMC) electrolytes were conducted to evaluate the chemical state changes of phosphorus in lithium-ion battery electrolyte during high-temperature storage. The samples consisted of an initial electrolyte and a degraded electrolyte stored at 80°C for 72 hours. Significant color change was observed in the electrolyte after high-temperature storage, confirming the progression of thermal degradation. While Raman spectroscopic analysis of the degraded sample was hindered by an increased fluorescent background, P K-edge XANES provided spectral information. In the pristine electrolyte, a primary peak was observed near 2154 eV, which is attributed to the electronic state of PF_6^- influenced by ion-pairing with Li^+ and its coordination environment in the liquid phase. For the electrolyte after high-temperature storage, a decrease in the 2154 eV component and an increase in the higher-energy component near 2158 eV were confirmed. These results suggest that the local electronic state and coordination environment around $LiPF_6$ change due to thermal degradation. Furthermore, the change in peak intensity ratios demonstrates that P K-edge XANES is an effective analytical method for tracking the thermal degradation behavior of $LiPF_6$-based electrolytes.

1. Introduction

Lithium-ion batteries (LIBs) are utilized in a wide range of applications, including electric vehicles and stationary energy storage systems, and there is an increasing demand for higher energy density and power density. Consequently, operation under high-voltage and high-temperature conditions has become increasingly important; however, such conditions are known to accelerate electrolyte decomposition, leading to performance degradation and shortened battery durability [1]. Particularly under high-temperature conditions, the decomposition reactions of electrolyte salts and solvents are enhanced, which destabilizes the electrode/electrolyte interface [2]. Therefore, understanding the thermal degradation mechanisms of electrolytes at the molecular and electronic levels can contribute to the development of highly durable LIBs.

In previous studies of LIBs, analytical techniques such as nuclear magnetic resonance (NMR), fourier transform infrared spectroscopy (FT-IR), and X-ray photoelectron spectroscopy (XPS) have been widely employed to analyze the degradation of electrode interfaces and electrolytes [3,4]. While NMR and FT-IR are applicable to electrolytes in the liquid state and are useful for identifying decomposition products and functional groups, methods that directly evaluate the electronic state and local chemical state of specific elements derived from electrolyte salts in the liquid state remain scarce. Furthermore, surface analysis techniques like XPS carry the risk of altering the original chemical state of the liquid sample during the processes of sample washing, drying, and introduction into a vacuum. Thus, there is an expectation for the establishment of methods that can directly analyze electrolytes in the liquid state and evaluate the chemical state of elements derived from electrolyte salts under conditions close to the battery reaction environment. Soft X-ray absorption spectroscopy is a sensitive technique for analyzing the electronic state and local structure of light elements and is highly useful in battery material research [5,6]. Specifically, measuring the absorption edges of elements containing electrolyte salts and organic solvents—such as phosphorus, oxygen, and fluorine—enables the identification of decomposition products and the evaluation of changes in coordination states. In the hard X-ray region, analyses of battery materials and electrolytes using XAS and total scattering are progressing [7], and examples of XAS measurements targeting liquid electrolytes have been reported [8]. While XAS measurement of liquid samples itself is feasible [9], to the best of our knowledge, no studies have reported on evaluating the chemical state of phosphorus derived from electrolyte salts in $LiPF_6$-based carbonate which is widely used as LIBs electrolytes using P K-edge XAS in the liquid state.

In this study, P K-edge XAS was applied to the bulk of $LiPF_6$/EC–EMC carbonate electrolytes

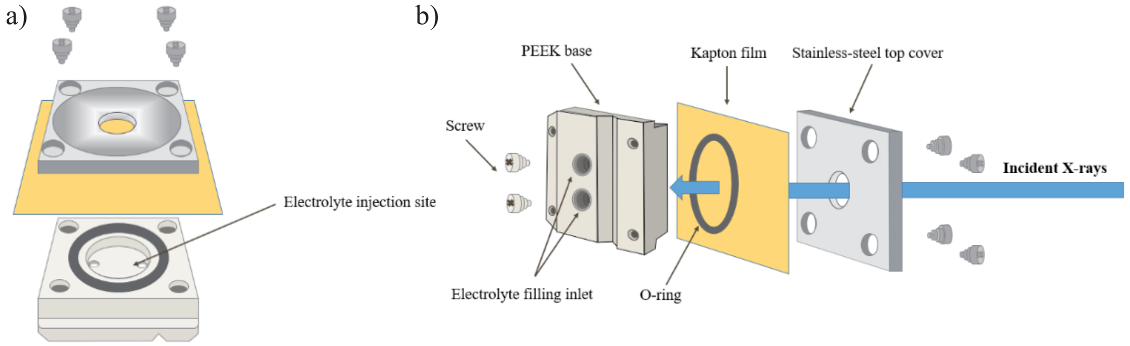

Fig. 1 a) Schematic illustration of the liquid cell for liquid-phase XAS measurements. b) Layout of each component.

degraded by high-temperature storage. Measurements were conducted at room temperature in the liquid state, and changes in the chemical state of phosphorus derived from the electrolyte salt due to thermal degradation were evaluated based on P K-edge X-ray absorption near-edge structure (XANES). We aimed to obtain insights into the decomposition reactions of $LiPF_6$-based electrolytes and changes in phosphorus-containing species under high-temperature conditions, while also assessing the effectiveness of P K-edge XANES for the bulk analysis of liquid electrolytes.

2. Experimental

The electrolyte solution employed was 1.0 mol dm^{-3} $LiPF_6$ in ethylene carbonate (EC) and ethyl methyl carbonate (EMC) (3:7 v/v, Kishida Chemical). Both the initial electrolyte and a thermally degraded electrolyte, which was maintained at 80°C for 72 hours in a thermostatic chamber, were used as samples. To prevent any exposure to the atmosphere, all samples were handled under an argon atmosphere glove box. Raman spectroscopic measurements were conducted within an argon-filled glove box using a PR-1w spectrometer (JASCO Corp.) with 785 nm excitation and an exposure time of 5 seconds to evaluate the structural changes induced by high-temperature storage. For XAS measurements, a specialized liquid cell was used, as shown in the schematic in Fig. 1, consisting of a polyether ether ketone (PEEK) base and a stainless-steel top cover equipped with a Kapton tape X-ray transparent window. The base and cover were sealed with an O-ring to ensure a leak-proof and airtight configuration. The electrolyte was injected into the cell through an inlet on the rear of the base after assembly to minimize gas entrapment, with the entire process performed inside the glove box. This cell was then transported to the measurement chamber using a transfer vessel. P K-edge XAS measurements were performed in the fluorescence yield mode at BL-13 of the Ritsumeikan University SR Center. In addition to the liquid electrolyte samples, the XAS spectrum of $LiPF_6$ powder (Kishida Chemical) was also measured as a reference for peak assignment and comparison of the phosphorus chemical states.

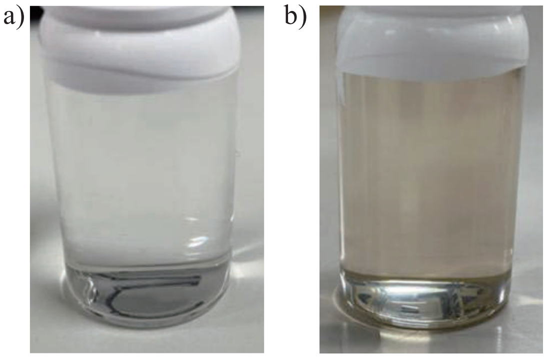

Fig. 2 Photographs of the $LiPF_6$/EC–EMC electrolyte before and after high-temperature storage: a) initial and b) after storage at 80°C for 72 hours.

3. Results and Discussion

Fig. 2 shows photographs of the $LiPF_6$/EC–EMC electrolyte before and after storage in a thermostatic chamber at 80°C. A comparison of (a) and (b) reveals a distinct color change of the electrolyte after storage at 80°C, suggesting that conventional LIB electrolytes undergo significant degradation in high-temperature environments. This color change is attributed to the thermal decomposition of the solvent and the electrolyte salt. In particular, $LiPF_6$ is known for its low thermal stability, generating decomposition products such as PF_5 and HF at elevated temperatures [3]. It is inferred that these decomposition products further react with the organic solvents, leading to the formation of complex degradation species that include chromophoric components.

Fig. 3 shows the Raman spectra of the $LiPF_6$/EC–EMC electrolyte before and after storage at 80°C. In the initial electrolyte prior to high-temperature storage, several distinct Raman peaks were observed

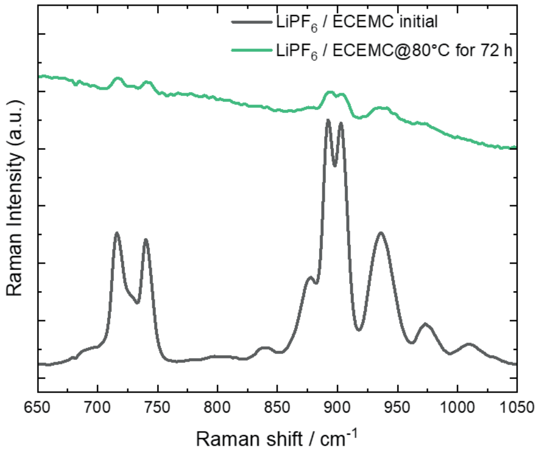

Fig. 3 Raman spectra of a 1.0 mol dm^{-3} LiPF$_6$/EC-EMC solution before and after being held at 80°C for 72 hours.

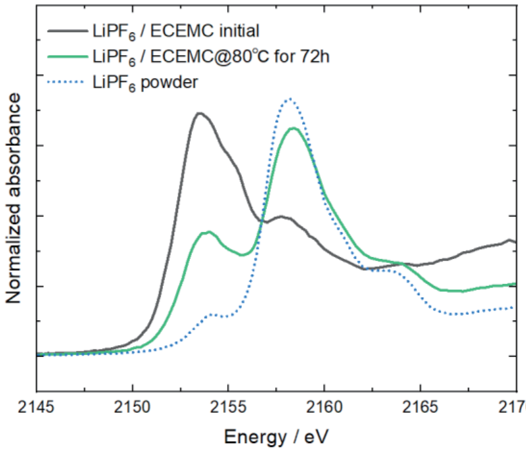

Fig. 4 P K-edge spectra of LiPF$_6$ powder before and after holding a 1.0 mol dm^{-3} LiPF$_6$/EC-EMC solution at 80°C for 72 hours.

in the 700–950 cm^{-1} region. The peak centered around 740 cm^{-1} corresponds to the P–F symmetric stretching vibration of the PF$_6^-$ anion [10]. In LiPF$_6$-based electrolytes, this P–F stretching vibration band is known to reflect Li$^+$– PF$_6^-$ interactions and ion-pair formation; thus, its peak position and profile vary depending on the existing state of the PF$_6^-$ anions, such as free PF$_6^-$ ions, contact ion pairs, and further associated ionic specie [11]. The peak splitting near 740 cm^{-1} observed in this study suggests that the PF$_6^-$ anions do not occupy a single uniform chemical environment, but rather exist in a variety of Li$^+$–PF$_6^-$ interaction states or multiple ion-associated configurations within the EC–EMC mixed solvent.

Meanwhile, the peak located near 900 cm^{-1} is primarily attributed to the ring-breathing mode of EC [10]. In LiPF$_6$-containing carbonate electrolytes, it has been reported that the ring-breathing mode of free EC appears at approximately 893 cm^{-1}, whereas the EC component coordinated to Li$^+$ undergoes a high-wavenumber shift to around 903 cm^{-1} [10]. In the spectra obtained in this study, multiple peaks were similarly observed in the corresponding wavenumber region, which likely reflects the heterogeneity of the Li$^+$ solvation environment within the EC–EMC mixed solvent.

However, for the electrolyte stored at 80 °C, the fluorescent background increased with increasing storage time, resulting in a significant decrease in the Raman peak intensities. The formation of fluorescent products associated with the thermal degradation of electrolytes has been previously reported [12]. In this study as well, it is considered that the degradation species generated during high-temperature storage strongly interfered with the Raman measurements. Consequently, it was difficult to analyze the bands derived from the PF$_6^-$ anion and the carbonate solvents with sufficient reliability in the degraded electrolyte. These results indicate that while Raman spectroscopy is effective for analyzing the solvation structures and ion association states in pristine or slightly degraded LiPF$_6$/EC–EMC electrolytes, it has inherent limitations in evaluating the chemical states within the bulk of severely degraded electrolytes.

Fig. 4 shows the P K-edge XANES spectra of the LiPF$_6$ electrolyte before and after high-temperature storage, alongside that of LiPF$_6$ powder as a reference sample. For the LiPF$_6$ powder, a characteristic absorption peak was observed near 2158 eV, and this energy position is in good agreement with previous reports for the PF$_6^-$-derived peak in crystalline LiPF$_6$ [13]. On the other hand, in the pristine LiPF$_6$ electrolyte (prior to high-temperature treatment), the primary peak was observed at a lower energy of approximately 2154 eV. Because this peak is located at a lower energy compared to the LiPF$_6$ powder, it is considered to reflect the solvation state of the PF$_6^-$ anion in the solution or differences in its coordination environment with Li$^+$. In other words, because the local electronic state surrounding PF$_6^-$ in the liquid phase differs from that in solid LiPF$_6$, it is inferred that a chemical shift occurs in the P K-edge absorption energy. A minor shoulder peak was also observed around 2155 eV, which might be attributed to intermediate decomposition products of PF$_6^-$ or complex coordination states in the liquid phase; however, its exact origin requires further investigation.

In the spectra following high-temperature storage, the intensity of the peak near 2154 eV decreased significantly. Conversely, an increase in the higher-energy component around 2158 eV was observed.

Given that $LiPF_6$ is the sole phosphorus-containing component in the electrolyte employed in this study, this higher-energy component is highly likely to originate from phosphorus-containing degradation products formed via the thermal decomposition of $LiPF_6$. Representative candidates for these products include POF_3, $Li_xPO_yF_z$, and phosphate-based compounds. It is postulated that changes in the local coordination structure and electronic state around the phosphorus center in these species are reflected as the shift in the absorption edge energy.

Furthermore, focusing on the peak intensity ratio between the features near 2154 eV and 2158 eV, a distinct trend was confirmed: as the degradation progressed, the lower-energy peak attenuated while the higher-energy peak intensified. These results suggest that the peak intensity ratio derived from P K-edge XANES can serve as an effective indicator for tracking the thermal degradation behavior of $LiPF_6$.

4. Conclusions

In this study, liquid-phase P K-edge XANES measurements were conducted on $LiPF_6$/EC–EMC carbonate electrolytes to evaluate the changes in the chemical state of phosphorus within the electrolyte bulk induced by high-temperature storage. Visual inspection revealed distinct discoloration of the electrolyte after storage at 80°C for 72 hours, confirming the occurrence of thermal degradation.

In the pristine electrolyte, a primary peak was observed near 2154 eV, which is presumed to reflect the solvation state of the PF_6^- anion and its coordination environment with Li^+ in the liquid phase. Conversely, following high-temperature storage, a decrease in the 2154 eV component and a concurrent increase in the higher-energy component near 2158 eV were observed. This suggests that the local electronic state and coordination environment surrounding $LiPF_6$ are altered as a result of thermal degradation.

Furthermore, the change in the peak intensity ratio with advancing degradation demonstrates the potential of P K-edge XANES as an effective analytical technique for tracking the thermal degradation behavior of $LiPF_6$-based electrolytes. Additionally, the successful application of the liquid XAS cell developed in this study demonstrated the feasibility of directly measuring the bulk of liquid electrolytes under strictly air-free conditions.

Acknowledgement

This work was supported by JST, The Green Technologies for Excellence (GteX) Program, Grant Number JPMJGX23S3. The authors would like to thank Prof. Takizawa (Ritsumeikan University) for valuable advice regarding the design of the liquid XAFS cell.

References

[1] C. L. Campion, W. Li and B. L. Lucht, *J. Electrochem. Soc.*, **2005**, 152, A2327.

[2] Z. W. Lebens-Higgins, S. Sallis, N. V. Faenza, F. Badway, N. Pereira, D. M. Halat, M. Wahila, C. Schlueter, T.-L. Lee, W. Yang, C. P. Grey, G. G. Amatucci and L. F. J. Piper, *Chem. Mater.*, **2018**, 30,958.

[3] H. Zhang, Y. Zhao, X. Li, H. Wang, L. Wang, Y. Song, F. Qiao, J. Wang and J. Xu, *Adv. Sci.*, 2**025**, 12, e03151.

[4] S. Wilken, M. Treskow, J. Scheers, P. Johansson and P. Jacobsson, *RSC Adv.*, **2013**, 3, 16359.

[5] K. Nakanishi, D. Kato, H. Arai, H. Tanida, T. Mori, Y. Orikasa, Y. Uchimoto, T. Ohta and Z. Ogumi, *Rev. Sci. Instrum.*, **2014**, 85, 084103.

[6] Y. Orikasa, K. Yamamoto, T. Shimizu and Y. Uchimoto, *Chem. Phys. Rev.*, **2022**, 3, 011305.

[7] K. Fujii, M. Matsugami, K. Ueno, K. Ohara, M. Sogawa, T. Utsunomiya and M. Morita, *J. Phys. Chem. C.*, **2017**, 121, 22720.

[8] Y. Zhang, G. Wan, N. H. C. Lewis, J. Mars, S. E. Bone, H.-G. Steinrück, M. R. Lukatskaya, N. J. Weadock, M. Bajdich, O. Borodin, A. Tokmakoff, M. F. Toney and E. J. Maginn, *ACS Energy Lett.*, **2021**, 6, 3458.

[9] K. Sato, G. Mori, T. Kiyosu, T. Yaji, K. Nakanishi, T. Ohta, K. Okamoto and Y. Orikasa, *Sci. Rep.*, **2020**, 10, 7362.

[10] K. Mukai, T. Inoue, Y. Kato and S. Shirai, *ACS Omega*, **2017,** 2, 864.

[11] S.-D. Han, S.-H. Yun, O. Borodin, D. M. Seo, R. D. Sommer, V. G. Young Jr. and W. A. Henderson, *J. Phys. Chem. C*, **2015**, 119, 8492.

[12] L. C. Fernandez, A. R. Neale, F. Braga, I. V. Sazanovich, R. Kostecki and L. J. Hardwick, *Phys. Chem. Chem. Phys.*, **2019**, 21, 23833.

[13] M. Shakouri, W. M. Holden, Y. Hu, Q. Xiao, R. Igarashi, B. Schreiner, M. Bree, M. Li, W. Li, X. Sun and T.-K. Sham, *Electron. Struct.*, **2020**, 2, 047001.

SHORT NOTES

Measurement of the Intensity Distribution of Betatron Oscillations and Synchro-Betatron Oscillations in the Stored Electron Beam Profile

Yasukazu Yamamoto
The SR Center, Ritsumeikan University, 1-1-1 Noji-Higashi, Kusatsu 525-8577, Japan

At the SR Center of Ritsumeikan University, radio frequency knockout (RFKO) method is used to control beam size and beam lifetime during routine operation [1]. In this study, we investigated the two-dimensional distribution of betatron oscillation intensity along the beam profile. In addition, we tried to investigate the distribution of the synchro-betatron oscillation intensity.

Measurement system was composed of the radiation detector (APDM: avalanche photodiode module, C5658 HAMAMATSU), spectrum analyzer and PC was constructed behind the beam extraction port BL-9 at the atmosphere [2]. A thick beryllium flat mirror was set to reflect the primary ray by 90° to extract the visible component in the vacuum chamber. This visible ray through the optical glass window to divide the vacuum and atmosphere was reflected again by an aluminum flat mirror and introduced into the measurement system. The stored beam profile was magnified strongly by the conventional profile monitor using objective lens and magnifying lens. The radiation detector was scanned using the micrometer on the beam profile in vertical and horizontal direction. For the operating condition of RFKO, the center of frequency was 57.618 MHz in agreement with vertical betatron frequency, deviation of frequency modulation 200 kHz, sweep frequency 2.9 kHz. Store beam current was about 50 mA at every measurement.

In figure 1 (a) and (b), we show the beam profile and betatron oscillation intensity distribution, respectively. It can be seen that the beam profiles are similar to a Gaussian distribution in both the horizontal and vertical directions. On the other hand, the distribution of betatron oscillation intensity shows a dip along the horizontal axis in the central region. This indicates that at least some of the electrons in the bunch are moving coherently due to forced oscillations induced by electrodes installed within the beam duct.

Figure 2 shows the measurement results for vertical scanning under synchro-betatron oscillation conditions. Its shape is similar to that observed in betatron oscillations. However, the intensity of the synchro-betatron oscillation is weak, even though the beam profile is equivalent to that under betatron oscillation conditions.

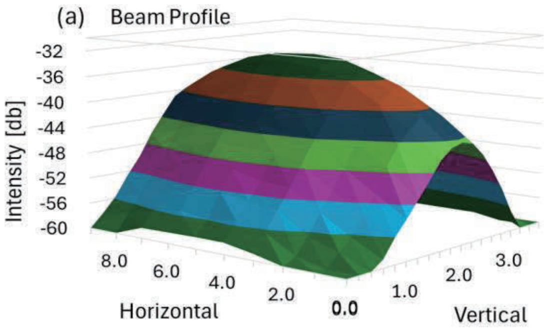

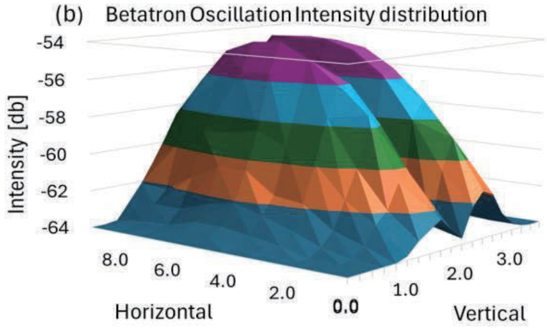

Figure 1 (a): Beam profile and (b): Betatron oscillation intensity distribution.

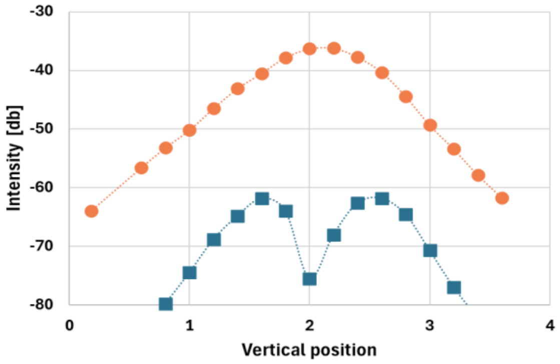

Figure 2: Beam profile (circles) and intensity distribution of synchro-betatron oscillation (squares).

References

[1] I. Sakai, Y. Yamamoto, T. Mitsuhashi, D. Amano and H. Iwasaki, *Nucl. Instrum. Methods A,* **2002**, *480,* 373.

[2] Y. Yamamoto, *Proc. IBIC2012*, 524-526.

F K-edge XAFS Study of Carbon Nanotube Adding to Graphite Anode for Lithium-ion Battery

Minami Ota[1], Takeru Hamada[1], Yuta Shiomi[1], Daisuke Shibata[2], Akinori Irizawa[2], Chengchao Zhong[1], Keiji Shimoda[3], Ken-ichi Okazaki[2] and Yuki Orikasa[1]

1) Department of Applied Chemistry, Ritsumeikan University, 1-1-1 Noji-Higashi, Kusatsu 525-8577, Japan
2) Research Organization of Science and Technology, Ritsumeikan University, 1-1-1 Noji-Higashi, Kusatsu 525-8577, Japan
3) Ritsumeikan Global Innovation Research Organization, Ritsumeikan University, 1-1-1 Noji-Higashi, Kusatsu 525-8577, Japan

Lithium-ion batteries suffer from severe performance degradation at elevated temperatures above 60 °C, which limits their application under high-temperature operating conditions. In particular, when the battery temperature reaches approximately 70–120 °C, the solid electrolyte interphase (SEI) formed on the anode surface can decompose, leading to continuous electrolyte decomposition and a decrease in battery performance. Previous studies have reported that silicon–graphite composite electrodes using carbon nanotubes (CNTs) as conductive additives exhibit better cycling stability than those using carbon black (CB) [1]. This improvement has been attributed to the ability of CNTs to maintain the electronic conduction network and stabilize the electrode structure against the volume changes of silicon. However, the influence of CNT conductive additives on the chemical composition of the SEI, particularly under high-temperature conditions, has not yet been sufficiently clarified. In this study, we investigated the effect of CNT conductive additives on the surface chemistry of graphite-based anodes after high-temperature cycling using soft X-ray absorption spectroscopy (XAS).

Graphite electrodes were prepared by mixing mesocarbon microbeads (MCMB) and polyvinylidene fluoride (PVDF) binder at a 9:1 mass ratio, while CNT-containing electrodes used MCMB/PVDF/CNT = 8.92:1:0.08. Slurries were coated onto Cu foil and tested in Li half-cells with 1.0 mol dm^{-3} $LiPF_6$ in EC/EMC (3:7, v/v). Cells were cycled between 0.005–3.0 V, including one cycle at 80 °C after initial cycling at 25 °C. After cycling, electrodes were recovered in an Ar glove box and analyzed by F K-edge XAS at BL-2, Ritsumeikan University SR Center.

Figure 1 shows the F K-edge XAS spectra of the graphite electrodes after high-temperature cycling. The spectrum of LiF powder is also shown as a reference. Both the electrodes with and without CNTs exhibited a main peak at approximately 692 eV and a weak shoulder at several eV higher energy. These spectral features are similar to those observed for LiF, indicating that LiF was formed on the graphite electrode surface after high-temperature cycling. Since LiF is generally produced through the decomposition of $LiPF_6$ and/or $LiPF_6$-derived species, the observed spectra suggest the formation of a fluorine-containing inorganic SEI layer under high-temperature conditions. No clear difference was observed between the F K-edge spectra of the electrodes with and without CNTs. Therefore, the improved cycling stability previously reported for CNT-containing electrodes is likely not due to a significant change in the LiF-rich inorganic SEI composition, but rather to other factors such as maintenance of the conductive network and mechanical stabilization of the composite electrode structure.

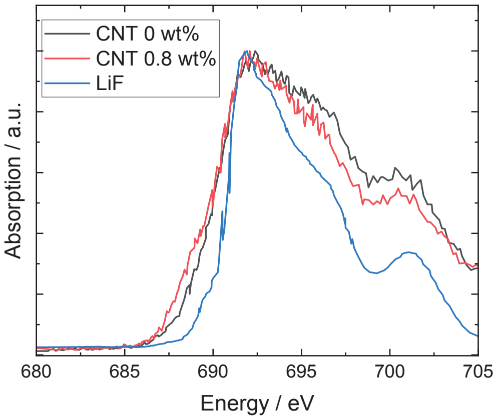

Fig. 1 F K-edge XAS of graphite electrodes with and without CNT after one cycle at 80 °C.

Acknowledgement

This work was supported by JST, The Green Technologies for Excellence (GteX) Program, Grant Number JPMJGX23S3. CNT was provided by Prof. Shiraishi (Gumma University).

References

[1] Y. Kim, M. Kim, N. Kim, H. Cha, S. Kim, J. Sung, and J. Cho, *Energy Storage Materials.*, **2025**, *74*, 103983

[2] T. Hamada, D. Shibata, C. Zhong, K. Shimoda, K. Okazaki, and Y. Orikasa, *Mem. SR Center Ritsumeikan Univ.*, **2025**, *27*, 3-5

Degradation Mechanism Analysis of Lithium-ion Battery Graphite Anode using Soft X-ray Absorption Spectroscopy

Takeru Hamada[1], Yuta Shiomi[1], Yutaro Goto[1], Daisuke Shibata[2], Akinori Irizawa[2], Chengchao Zhong[1], Keiji Shimoda[3], Ken-ichi Okazaki[2] and Yuki Orikasa[1]

1) Department of Applied Chemistry, Ritsumeikan University, 1-1-1 Noji-Higashi, Kusatsu 525-8577, Japan

2) Research Organization of Science and Technology, Ritsumeikan University, 1-1-1 Noji-Higashi, Kusatsu 525-8577, Japan

3) Ritsumeikan Global Innovation Research Organization, Ritsumeikan University, 1-1-1 Noji-Higashi, Kusatsu 525-8577, Japan

Lithium-ion batteries are required to operate under diverse environmental conditions for the application of electric vehicle, drone and adjustment of data center. In particular, at elevated temperatures, battery degradation is accelerated due to increasing resistance between electrode and electrolyte. However, the reaction mechanisms and degradation factors at the electrode-electrolyte interface under high-temperature conditions have not been fully understood. In this study, we investigated the electrode surface film on graphite anodes using three different electrolytes via X-ray absorption spectroscopy (XAS).

Graphite composite electrodes were assembled into half-cells in an Ar-filled glovebox, using lithium metal foil as the counter electrode. Three types of electrolytes were used: 1.0 M $LiPF_6$ in ethylene carbonate (EC)/ethyl methyl carbonate (EMC) (3:7 in volume ratio), 1.0 M LiFSI in dimethyl carbonate (DMC), and 5.5 M LiFSI in DMC. Following two pre-cycles at 25 °C, galvanostatic charge-discharge measurements were conducted at 0.1C at either 25 or 80 °C (voltage window: 0.005–3.0 V). After cycling, the electrodes were washed with DMC, and their surface chemical states were analyzed by XAS at the SR Center, Ritsumeikan University (BL-13). The samples were transferred to the measurement chamber from the glovebox without air-exposure. P and S K-edge XAS were measured in total electron yield (TEY) mode.

Figure 1(a) and (b) show the P K-edge XAS spectra of the samples using 1.0 M $LiPF_6$ in EC:EMC, and S K-edge XAS spectra of the samples using 1.0 M and 5.5 M LiFSI in DMC, respectively. In the P K-edge spectra, peaks corresponding to P-O bonds and salt-derived decomposition products were observed at approximately 2153 eV and 2158 eV, respectively. At elevated temperatures, the intensity of the P-O peak decreased, whereas that of the salt-derived decomposition products increased. Given that P-O compounds are inherently thermally stable, this decrease in peak intensity is presumably driven by the co-exfoliation of the inorganic P-O compounds as the organic components in the surface film thermally decompose and detach. Furthermore, the increase in the salt-derived peak suggests the ongoing thermal decomposition of the $LiPF_6$ salt itself. In the S K-edge spectra, three main peaks were detected: SO_4^{2-} at 2482 eV, S (VI) at 2480 eV, and S(IV) at 2478 eV. Variations dependent on electrolyte concentration and temperature were predominantly observed for the 2480 eV and 2478 eV peaks. The intensity of the 2480 eV peak increased at elevated temperatures in both low- and high-concentration electrolytes. This peak is attributed to compounds formed through the decomposition of organic species and their subsequent reactions with anions at high temperatures. In contrast, the S(IV) peak at 2478 eV was observed exclusively in the high-concentration electrolyte. Previous computational studies have also reported that tetravalent sulfur compounds, such as LiNSO, are generated via anion decomposition in high-concentration systems[1]. This peak originates from products formed by the preferential reductive decomposition of anions in the high-concentration electrolyte.

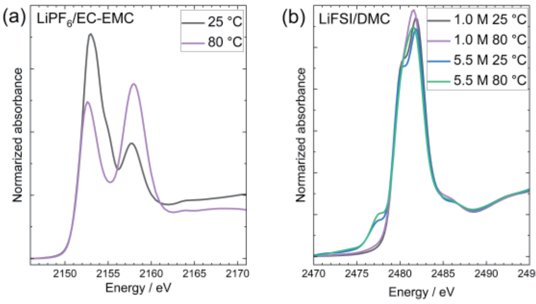

Fig. 1 (a) P and (b) S K-edge XAS spectra of the cycled electrodes for 1.0 M $LiPF_6$/EC:EMC and LiFSI/DMC, respectively.

Acknowledgement

This work was supported by JST, The Green Technologies for Excellence (GteX) Program, Grant Number JPMJGX23S3.

References

[1] Y. Liu, Q. Sun, P. Yu, Y. Wu, L. Xu, H. Yang, M. Xie, T Cheng, and W. A. Goddard, *J. Phys. Chem. Lett.* **2021**, *12*, 2922–2929

XAFS Analysis of Temperature-Programmed Reduction Process of NiO Particles Supported on SiO_2 by CH_4

Haku Tsukuda, Kodai Ohta, and Yasuhiro Inada
Department of Applied Chemistry, Graduate school of Life Sciences, Ritsumeikan University,
1-1-1 Noji-Higashi, Kusatsu 525-8577, Japan

Supported Ni catalysts exhibit high catalytic activity in reactions such as steam reforming and partial oxidation of CH_4 [1]. Ni is an abundant and inexpensive alternative to precious metals and is expected to be used as a promising alternative catalyst material [2]. In this study, NiO particles with controlled size were prepared on SiO_2 using an impregnation method with organic additives. *In situ* XAFS analysis was performed on the NiO particles during the temperature-programmed reduction process under a CH_4 gas flow. We have clarified the chemical state change of the Ni species as a function of temperature.

Malonic acid and SiO_2 were added to an aqueous solution of $Ni(NO_3)_2$, dried at 70 °C for 72 h, and the obtained powder was subsequently calcined at 600 °C for 3 h in air. As the pretreatment, the sample was subjected to a reduction treatment under an H_2 gas flow, followed by an oxidation treatment under an O_2 gas flow. *In situ* XAFS measurements were carried out up to 700 °C under a flow of CH_4 diluted with He (10 vol%) at BL-3 of the SR Center (Ritsumeikan University).

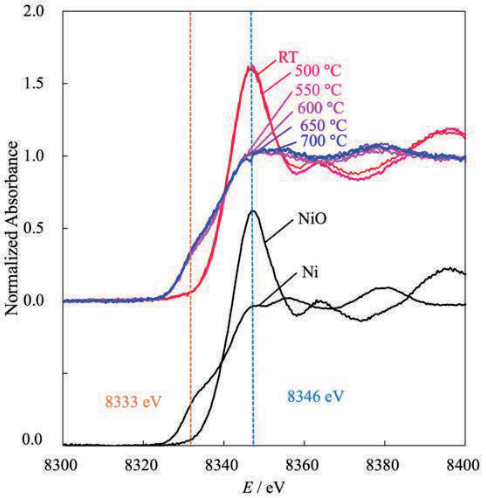

Fig. 1. XANES spectral change during the temperature-programmed reduction process of NiO supported on SiO_2 under a CH_4 gas flow.

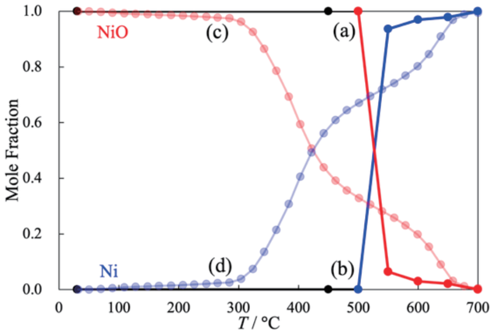

Fig. 2. Composition changes of the Ni species during the reduction process under a flow of CH_4 (a and b) and H_2 (c and d) [3].

The observed XANES spectral change is shown in Fig. 1. The initial spectrum was consistent with that of NiO. The decrease in the white line intensity and the low-energy shift of the absorption edge occurred in a narrow temperature range from 500 °C to 550 °C. Then, the spectra above 550 °C were in agreement with that of metallic Ni. Figure 2 shows the temperature dependence of the composirtion of the Ni species calulated by the linear combination fitting analysis of the XANES spectrum. The changes during the corresponding process under a flow of diluted H_2 are also plotted in Fig. 2. The reduction begins at a lower temperature of *ca*. 300 °C under H_2, and the second stage of the reduction above 450 °C has been interpreted as being due to NiO stabilized at the interface with SiO_2 [3]. Under a CH_4 atmosphere, the reduction started at a higher temperature of 500 °C, but the reduction of all NiO was completed at a lower temperature of 550 °C. It is considered that when metallic Ni is generated on the particle surface by the reduction with CH_4, it acts as a cracking catalyst of CH_4 and the formed H_2 promotes the reduction of the remaining NiO. Furthermore, the formation of carbon tubes associated with the CH_4 cracking is interpreted as causing the detachment of Ni particles from the SiO_2 surface [4]. As a result, the stabilizing effect of NiO at the interface with SiO_2 disappeared, and the reduction of NiO proceeded rapidly within a narrow temperature range of 500–550 °C.

References

[1] A. P. E. York, T. Xiao, and M. L. H. Green, *Top. Catal.*, **2003**, *22*, 345.
[2] S. Z. Tasker, E. A. Standley, and T. F. Jamison, *Nature*, **2014**, *509*, 299.
[3] E. Novitasari, A. Azuma, K. Ohta, M. Katayama, Y. Niwa, M. Kimura, and Y. Inada, *Next Mater.*, **2025**, *8*, 100738.
[4] S. Takenaka, S. Kobayashi, H. Ogihara, and K. Otsuka, *J. Catal.*, **2002**, *217*, 79.

Effect of Crystal Phase on XAFS of Manganese Oxide

Mizuki Fujita[1], Kiyotaka Asakura[2], and Yasuhiro Inada[1]
1) Department of Applied Chemistry, Graduate School of Life Sciences, Ritsumeikan University, 1-1-1 Noji-Higashi, Kusatsu 525-8577, Japan
2) SR Center, Ritsumeikan University, 1-1-1 Noji-Higashi, Kusatsu 525-8577, Japan

MnO_2 has various crystal structures, including α, β, γ, δ, ε, and λ phases, and these structures are deeply related to differences in the catalytic properties. The crystal structure of MnO_2 is composed of MnO_6 octahedral units that share edges and vertices, forming various tunnel and layered structures [1]. In this study, MnO_2 samples with different crystal phases were synthesized and characterized by XRD and XAFS measurements. The aim was to establish a method for evaluating the crystal structure of MnO_2 using XAFS by analyzing the relationship between XAFS spectra and crystal structure in detail.

The samples of α-, β-, γ-, δ-, and ε-MnO_2 were prepared by hydrothermal and redox methods using different Mn(II) precursors and oxidizing agents. For α- and β-MnO_2, $MnSO_4\cdot5H_2O$ and $KClO_3$ were used, and the crystal phase was controlled by changing the reaction temperature. γ-MnO_2 was prepared using $MnCl_2\cdot4H_2O$ and $KMnO_4$, whereas $MnSO_4\cdot5H_2O$ and $KMnO_4$ were used for δ-MnO_2 and ε-MnO_2. The obtained powder was washed, dried, and the crystal structure was confirmed by XRD. The XAFS measurements were carried out at the Mn K-edge at BL-3 in the SR Center (Ritsumeikan Univ.).

Figure 1 shows the XANES spectra for various MnO_2 phases. β-MnO_2 exhibited a shift of the white line peak toward higher energy, along with a slight increase in the pre-edge peak intensity. In contrast, δ-MnO_2 showed a shift toward lower energy with a slightly decreased pre-edge peak intensity. However, it is difficult to quantitatively discuss the relationship between crystal structure and XANES spectra based on the present results, and further understanding requires more detail analysis regarding the electronic state near the valence level. The Fourier transforms of the EXAFS oscillation functions for various MnO_2 phases are shown in Fig. 2. All these Fourier transforms were well reproduced using the atomic arrangements reported for each crystal structure. β-MnO_2 showed relatively strong Mn–Mn peaks, indicating a highly ordered structure due to its rutile-type framework. In contrast, ε-MnO_2 exhibited weaker peaks, suggesting a large structural disorder, which can be explained by approximately 50% Mn deficiency. The low-intensity third shell peak shown by δ-MnO_2 is ascribed by its layered structure. This study revealed that the EXAFS information is useful for distinguishing the crystal structure of MnO_2.

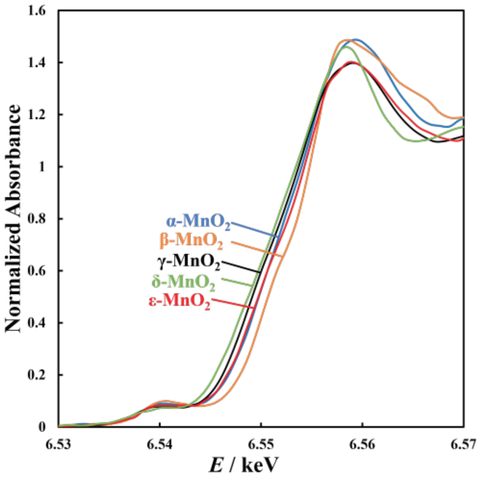

Fig. 1 XANES spectra at the Mn K-edge for various MnO_2 phases.

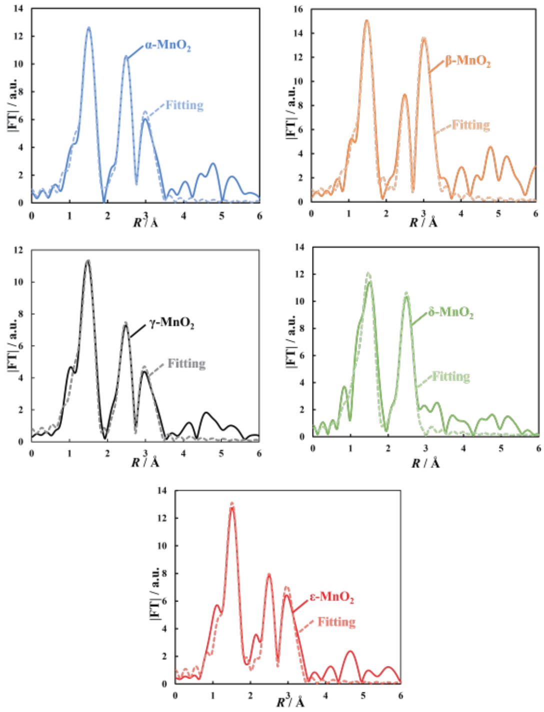

Fig. 2 Fourier transforms of EXAFS oscillation functions for various MnO_2 phases.

Reference

[1] D. Gangwar and C. Rath, *Appl. Surf. Sci.*, **2021**, *557*, 149693.

Chemical State Analysis for Calcination Process of Chromium Catalyst Supported on γ-Alumina

Hayato Suzuki, Kakeru Hanano, and Yasuhiro Inada
Department of Applied Chemistry, Graduate School of Life Sciences, Ritsumeikan University,
1-1-1 Noji-Higashi, Kusatsu 525-8577, Japan

Cr catalyst supported on γ-Al_2O_3 is widely used in dehydrogenation reactions of light alkanes, such as propane dehydrogenation. Understanding the oxidation states of the active species in Cr catalysts is important in the petrochemical industry, because chromium has multiple stable oxidation states [1,2]. It has been reported that the chemical state of the Cr species depends on the Cr loading, the characteristics of the supporting material, and the preparation method [3]. In this study, γ-Al_2O_3-supported Cr catalysts with variable Cr loadings were prepared using the impregnation method, and the chemical state changes of the Cr species during the calcination process were analyzed via *in situ* XAFS technique.

The powder of γ-Al_2O_3 was suspended in an aqueous solution of $Cr(NO_3)_3$ acidified with nitric acid, and dried in air at 120 °C for 36 h. The obtained powder was calcined by heating up to 700 °C under a flow of 10 vol% O_2 gas diluted with He. *In situ* XAFS measurements were performed at the Cr K edge at BL-3 in the SR Center (Ritsumeikan Univ.).

Figure 1 shows the XANES spectral change during the calcination process for the Cr catalyst (20 wt%), along with the temperature change of the X-ray absorbance at 5.992 keV and 6.007 keV. The initial spectrum matched that of the precursor $Cr(NO_3)_3 \cdot 9H_2O$, and no significant changes were observed up to 150 °C. The pre-edge peak intensity increased from 150 °C to 250 °C, and the spectrum at 250 °C was consistent with that of CrO_3. Upon further heating, the pre-edge peak disappeared, and the absorption edge shifted to a lower energy, resulting in the appearance of a white line peak around 6.007 keV. The spectrum at 700 °C was similar to that of Cr_2O_3. Figure 2 shows the composition changes of the Cr species during the calcination process. The oxidation from the precursor to CrO_3, which occurs around 170 °C, is thought to be the result of nitrate ions or O_2 molecules acting as oxidizing agents. It was found that CrO_3 is unstable at high temperatures and undergoes the deoxygenation to form Cr_2O_3 even in the presence of O_2. The conversion temperature at which the amounts of CrO_3 and Cr_2O_3 become equal was 538 °C for a 20 wt% sample, as shown in Fig. 2. The conversion temperature was 629 °C and 700 °C with the Cr load of 10 wt% and 3 wt%, respectively. The decrease in the Cr loading shifted the conversion temperature to higher, suggesting that the dispersion of CrO_3 increased at lower Cr loading. The results of this study provided valuable information regarding the preparation conditions for the Cr catalysts supported on γ-Al_2O_3.

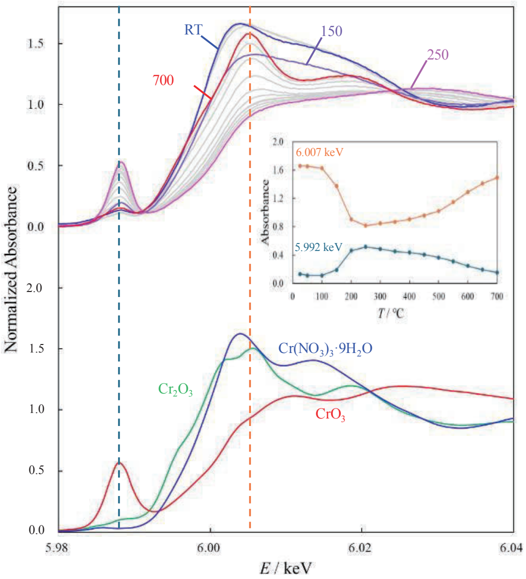

Fig. 1 XANES spectral change during the calcination process for the Cr catalyst (20 wt%), along with the temperature change of the X-ray absorbance at 5.992 keV and 6.007 keV.

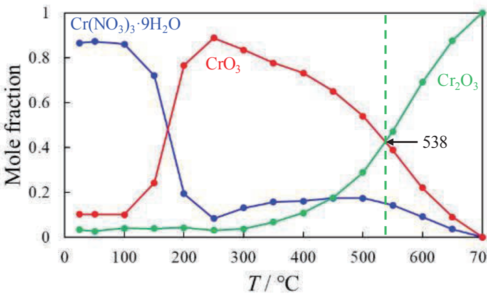

Fig. 2 Composition changes of the Cr species as a function of temperature.

References

[1] Z. Zhang, D. He, Z. Huang, S. He, J. Lu, and Y. Luo, *ACS Appl. Mater. Interfaces*, **2021**, *13*, 19873.

[2] A. Wegrzyniak, S. Jarczewski, A. Wegrzynowicz, B. Michorczyk, P. Kuśtrowski, and P. Michorczyk, *Nanomaterials*, **2017**, *7*, 249.

[3] B. Grzybowska, J. Słoczynski, R. Grabowski, K, Wcisło, A. Kozłowska, J. Stoch, and J. Zielinski, *J. Catal.*, **1998**, *178*, 698.

Chemical State Analysis for Oxygen Dissociation Process of Manganese Oxide Catalyst Supported on γ-Alumina

Yume Okamoto and Yasuhiro Inada
Department of Applied Chemistry, Graduate School of Life Sciences, Ritsumeikan University,
1-1-1 Noji-Higashi, Kusatsu 525-8577, Japan

Catalytic oxidation has been widely studied for the removal of volatile organic compounds (VOCs) [1]. In particular, manganese oxide catalysts are promising research targets because they have multiple oxidation states and are known to exhibit a self-reduction reaction even under oxygen-containing atmospheres [2]. In this study, γ-Al_2O_3-supported manganese oxide catalysts were prepared by the incipient wetness method, and *in situ* XAFS measurements were performed during the heating process.

An aqueous solution of $Mn(NO_3)_2 \cdot 6H_2O$ was added to γ-Al_2O_3, and the sample was dried at 60 °C in air for 8 days. The sample was further calcined at 300 °C in air for 30 min. XAFS measurements were performed at the Mn K edge at BL-3 in the SR Center (Ritsumeikan Univ.). As shown in Fig. 1, the spectrum of the sample with only drying treatment still contains features derived from the aqueous solution of manganese(II) nitrate, which is the precursor. These features were not observed after calcination, indicating that the sample was completely converted to MnO_2 by calcination.

To elucidate the crystalline phase of MnO_2, EXAFS analysis was performed on XAFS spectra measured at BL-12C of PF (KEK). The obtained Fourier transform function is shown in Fig. 2, and it was found that β-type MnO_2 existed in the prepared sample.

Figure 3 shows the change in the XANES spectrum obtained by *in situ* XAFS measurements during the heating process up to 700 °C under a 10 vol% O_2 flow. The state of β-MnO_2 was maintained up to 540 °C, and the absorption edge shifted to lower energy at 560 °C. The spectrum at above 600 ºC was consistent with that of Mn_2O_3. *In situ* XAFS measurements were also performed under a He flow. The conversion to Mn_2O_3 occurred at 440 °C, and further deoxygenation to Mn_3O_4 proceeded at 530 °C.

The precursor was completely converted to β-MnO_2 by calcination, and deoxygenation proceeded at around 560 °C under a 10 vol% O_2 flow. Further investigation under different O_2 contents is required to clarify the deoxygenation mechanism. This study contributes to a better understanding of the preparation and deoxygenation behavior of MnO_2 catalyst supported on γ-Al_2O_3.

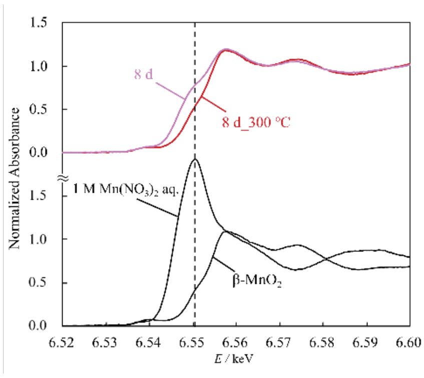

Fig. 1 XANES spectra of the dried and calcined samples.

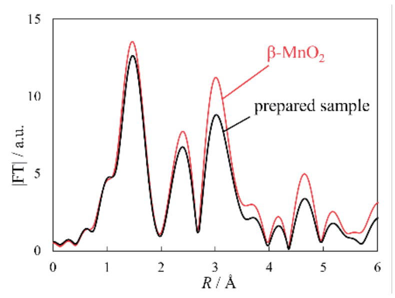

Fig. 2 Fourier transform function of the prepared sample and β-MnO_2.

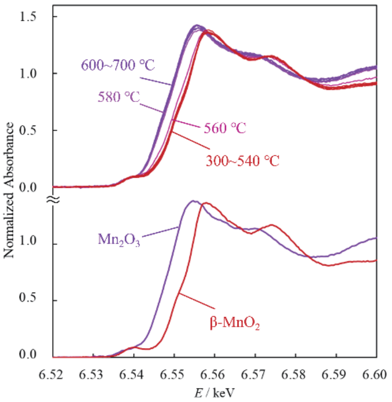

Fig. 3 XANES spectral change during the heating process up to 700 °C under a 10 vol% O_2 flow.

References

[1] Z. Wang, Y. Qin, F. Pan, Z. Li, W. Zhang, F. Wu, D. Chen, W. Wen, and J. Li, *Ind. Eng. Chem. Res.*, **2018**, *57*, 7374.

[2] S. C. Kim and W. G. Shim, *Appl. Catal. B*, **2010**, *98*, 180.

Local Structure Analysis of $Ln_{0.7}Sr_{2.3}F_{2.7}S_2$ (Ln = La, Nd, Gd) by Lanthanide L_3-edge EXAFS

**Yuto Fujioka[1], Chengchao Zhong[1], Keiji Shimoda[2],
Ken-ichi Okazaki[3], and Yuki Orikasa[1]**

1) *Department of Applied Chemistry, Ritsumeikan University, Kusatsu 525-8577, Japan*
2) *Ritsumeikan Global Innovation Research Organization, Ritsumeikan University, Kusatsu 525-8577, Japan*
3) *Research Organization of Science and Technology, Ritsumeikan University, Kusatsu 525-8577, Japan*

Fluorosulfide La-Ba-F-S has been reported as a new fluoride-ion conductor [1], and its Sr analogue possesses potentially high ionic conductivity comparable to that of the benchmark tysonite $La_{0.9}Ba_{0.1}F_{2.9}$. It is well known that partial substitution of La with other elements can modify the F^- conduction pathway and is an effective approach for further improving ionic conductivity. However, the influence of hetero-element substitution cannot be directly investigated using X-ray diffraction (XRD). On the other hand, extended X-ray absorption fine structure (EXAFS) analysis enables element-specific investigation of the local structure around rare-earth elements. However, to the best of our knowledge, no such analysis has been reported for fluoridesulfide compounds. In general, the absorption edge energies of rare-earth K-edge are relatively high above 30 keV, limiting the availability of suitable synchrotron radiation facilities. In contrast, L-edge absorption energies are on order of several keV, allowing measurements to be carried out at a wider range of facilities. In this study, XAFS measurements at the La, Nd and Gd L_3-edge were performed for (Ln = La, Nd, Gd) in order to analyze the local structure around lanthanide species.

$Ln_{0.7}Sr_{2.3}F_{2.7}S_2$ (Ln = La, Nd, Gd) were synthesized using a conventional solid-state reaction method. LaF_3(99.9%), NdF_3(99.9%), GdF_3(97.0%), SrF_2(99.5%) were weighed according to the stoichiometric rations, while SrS(99%) was added in 10 mol% excess to compensate for possible sulfur loss during heat treatment. The mixed powders were pressed into pellets with a diameter of 10 mm, and vacuum-sealed in a glass tube. The pellets were calcined twice at 1050 °C for 40 h with an intermediate grinding. XRD measurements were carried out to identify the crystal phases of the synthesized samples. XAFS measurements at the La, Nd and Gd L_3-edge were performed at BL-4 of Ritsumeikan University SR Center in a transmission mode.

The XRD patterns for $Ln_{0.7}Sr_{2.3}F_{2.7}S_2$ exhibit the same overall profile, except for a shift in the peak. The lattice constants decreased in the order of La > Nd > Gd, consistent with decrease in the ionic radii of the lanthanide ions. Figure 1 shows the k^2-weighted EXAFS oscillations at the Ln L_3-edges for $Ln_{0.7}Sr_{2.3}F_{2.7}S_2$ (Ln = La, Nd, and Gd). The oscillation periods differ among the La, Nd, and Gd samples, indicating differences in the interatomic distances around the Ln ions.

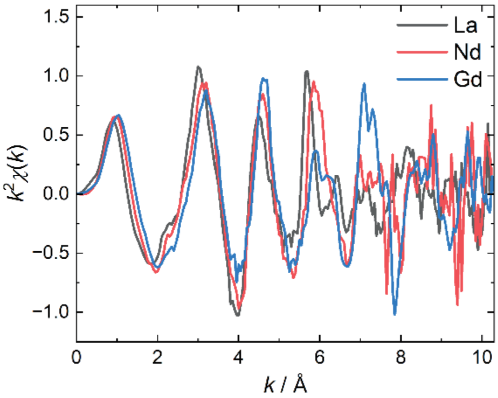

Fig. 1 EXAFS oscillations of $Ln_{0.7}Sr_{2.3}F_{2.7}S_2$ (Ln = La, Nd, Gd).

The Fourier-transformed spectra from the EXAFS oscillations are shown in Fig. 2. $La_{0.7}Sr_{2.3}F_{2.7}S_2$ appears to exhibit a more distorted peak for second coordination shell around 2.2 Å, suggesting that the medium-range local structure around La differs from those around Nd and Gd.

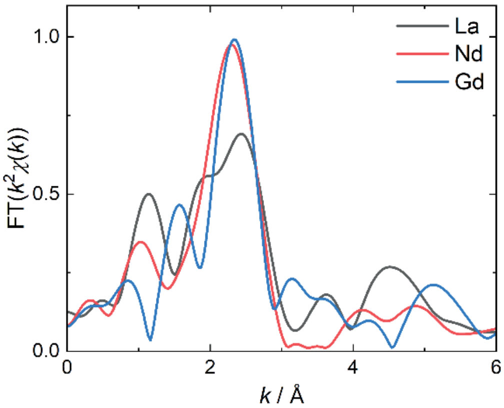

Fig. 2 The Fourier transforms of the Ln L_3-edge EXAFS for $Ln_{0.7}Sr_{2.3}F_{2.7}S_2$ (Ln = La, Nd, Gd).

References

[1] S. Tachibana, C. Zhong, T. Tojigamori, H. Miki, T. Matsunaga, and Y. Orikasa, *J. Mater. Chem. A*, **2024**, *12*, 14419.

Upgrade of Surface preparation system at BL-7

Naoyuki Maejima and Masaru Takizawa
Department of Physical Sciences, Facalty of Science & Engineering, Ritsumeikan University, 1-1-1 Noji-Higashi, Kusatsu 525-8577, Japan

Two photoelectron spectroscopy systems, Display-type spherical mirror analyzer (DIANA) and SCIENTA SES2002, are installed at the linearly polarized soft x-ray beamline BL-7 of the SR Center, Ritsumeikan University, for the investigation of surface electronic states using synchrotron radiation in the photon energy range of 10–200 eV.[1] Surface cleaning has been performed in the SES2002 system using Ar$^+$ sputtering and mechanical polishing prior to photoelectron spectroscopy measurements. In order to investigate the electronic structure of clean surfaces and thin films grown on them, an electron-beam heating system and a low-energy electron diffraction (LEED) system were newly installed.

The components and assembled configuration of the heating sample holder are shown in Figure 1(a) and (b), respectively. A hole was made at the center of the standard sample holder used at the SR center, and a commercially available bushing-type ceramic insulator was inserted into the hole to allow the EB heating filament to approach the backside of the sample. As a result, the filament can be inserted from the backside of the sample (Fig. 1(b)) while the sample holder is mounted on a transfer rod, and heating up to at least 900 °C has been confirmed using a tantalum sample holder. Using this heating system, the Cu(111) surface was cleaned by repeated cycles of Ar$^+$ sputtering (0.5 keV) and annealing (600 °C). The prepared Cu(111) samples exhibited a 1x1 LEED pattern as shown in Figure 2. Angle-resolved photoemission spectroscopy (ARPES) measurements were performed on the cleaned Cu(111) sample using synchrotron radiation at photon energies of 20, 70, and 140 eV. The obtained ARPES spectra along the $\bar{\Gamma}$- $\bar{K}$ direction at photon energies of 20, 70, and 140 eV are shown in Fig. 3(a), (c), and (e), while their second-derivative spectra are shown in Fig. 3(b), (d), and (f), respectively. The Shockley surface state was clearly observed near a detection angle of 0° in measurements at 20 eV (Fig. 3(a)) and 70 eV (Fig. 3(c)). This result indicates the successful preparation of a clean surface. In contrast, it was not observed at 140 eV, which can be attributed to the complex photoemission cross section of the Shockley surface state of Cu(111).[2]

In summary, a surface preparation system has been successfully installed at BL-7, and ARPES measurements have been demonstrated using this system.

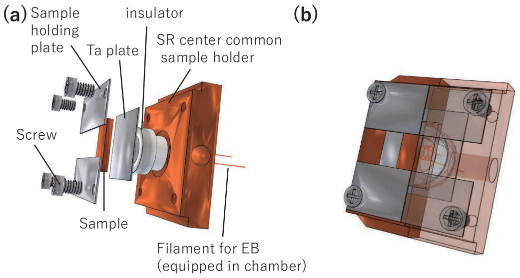

Fig. 1. (a) Components of the heating sample holder. (b) Assembled sample holder (the right half is shown semi-transparently).

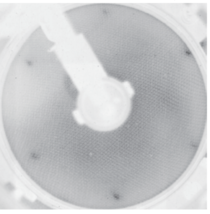

Fig. 2 1x1 LEED pattern of Cu (111) clean surface at 100eV measured by BACK-DISPLAY LEED-AUGER OPTICS MODELS BDL450IR.

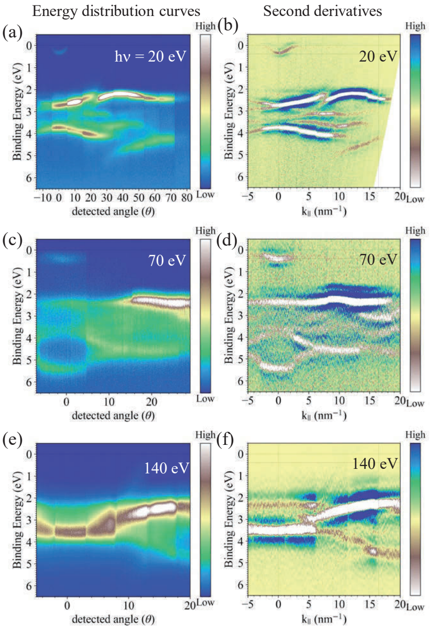

Fig. 3 (a), (c), (e) ARPES spectra obtained at photon energies of 20, 70, and 140 eV and (b), (d), (f) their second derivatives.

References

[1] M. Takizawa, *MEMOIRS OF THE SR CENTER RITSUMEIKAN UNIVERSITY.* **18** (2016) 115.
[2] Lobo-Checa, *et al.*, *Phy. Rev. B*, **84** (2011) 245419.

Orientation Angle Changes of Vapor-Deposited Pentacene on an Annealing $SrTiO_3$ Substrate

Masashige Fujiki, Naoyuki Maejima, and Masaru Takizawa
Department of Physical Sciences, Faculty of Science and Engineering, Ritsumeikan University, Noji-Higashi 1-1-1, Kusatsu 525-8577, Japan

Devices using organic semiconductors have attracted considerable attention in recent years because they can be manufactured at low cost, are lightweight and flexible, and have a low environmental impact compared to inorganic semiconductors. However, their applications are limited due to their lower carrier mobility compared to inorganic semiconductors. To improve the performance of organic semiconductor devices, controlling molecular orientation is essential. Pentacene, which has high carrier mobility among organic semiconductors, has been studied as a transistor material. It is a polycyclic aromatic compound composed of five linearly fused benzene rings. It is well known that the molecular orientation of pentacene is strongly influenced by the substrate and its surface condition, although many aspects remain unclear. Previous studies have shown that molecular orientation depends on the substrate: on insulating substrates, molecules tend to orient more perpendicular to the surface [1], while on conductive substrates, they tend to orient more parallel to the surface [2]. In this experiment, to clarify the influence of the substrate, we evaluated molecular orientations using near-edge X-ray absorption fine structure (NEXAFS) measurements.

The measurements were performed at BL-8 of the SR Center, Ritsumeikan University. The substrate used in this experiment was prepared by annealing $SrTiO_3$ at 830°C for 30 minutes under ultrahigh vacuum ($\sim 10^{-8}$ Pa). Pentacene was deposited at a rate of 0.6 Å/min using a quartz crystal monitor under ultrahigh vacuum ($\sim 10^{-6}$ Pa). The NEXAFS measurements were performed at room temperature under ultrahigh vacuum (8×10^{-8} Pa). The spectra were recorded in partial electron yield mode, and the orientation angle of pentacene was evaluated by curve fitting.

For samples deposited for 10–100 s, the intensity of the peak corresponding to the $1s\rightarrow\pi^*$ transition was stronger at an incident angle of 60° than at 0°. In contrast, samples deposited for 150–500 s exhibited the opposite trend. These results indicate that pentacene is nearly parallel to the surface in samples with deposition times of less than 100 s, and tilted in samples with deposition times exceeding 150 s.

Since the spectral line shapes differ depending on the deposition time, the spectra were decomposed using the spectrum for 10 s deposition (representing a purely parallel orientation) and that for 500 s deposition (representing a purely perpendicular orientation). As shown in Fig. 2, peaks derived from pentacene were successfully reproduced. In addition, the composition ratio of the spectra showed that the contribution from the perpendicular component increases as the deposition time increases. These results suggest that increasing the deposition time increases the fraction of perpendicularly orientated pentacene, resulting in a transition of the overall molecular orientation from a lying (parallel) state to a standing (perpendicular) state.

These findings indicate that the molecular orientation of pentacene gradually transitions from a parallel to a perpendicular configuration with increasing deposition time.

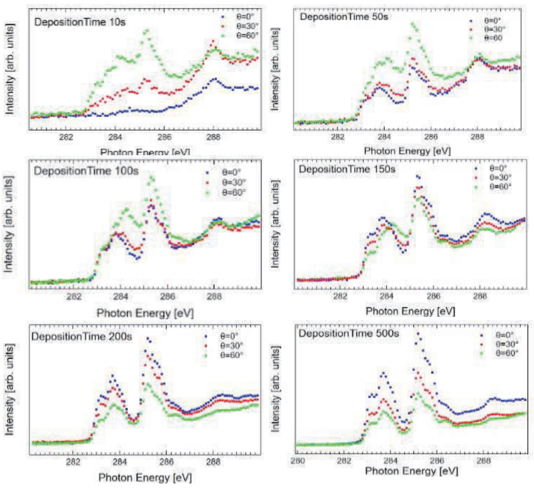

Fig. 1 NEXAFS spectra of pentacene on the $SrTiO_3$ substrate.

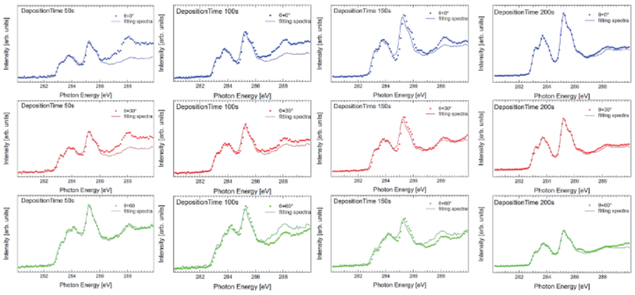

Fig. 2 Results of linear combination fitting for spectra obtained at (photon incidence angles of) 0°, 30°, and 60°.

References

[1] G. Yoshikawa *et al.*, Surf. Sci. **600**, 2518 (2006).
[2] G. Bavdek *et al.*, Langmuir **24**, 767 (2008).

Surface State Changes of $SrTiO_3$(100) Induced by Variation in Sputtering Incidence Angle

Masaya Sakai, Naoyuki Maejima, and Masaru Takizawa
Department of Physical Sciences, Faculty of Science and Engineering, Ritsumeikan University, 1-1-1 Noji-Higashi, Kusatsu 525-8577, Japan

Strontium titanate ($SrTiO_3$, STO) is a transition metal oxide with a perovskite structure and has been widely studied as a substrate for the epitaxial growth of oxide thin films due to its excellent chemical stability. In recent years, attention has also been focused on its high dielectric constant and unique surface electronic states, making it a promising substrate material for low-voltage organic field-effect transistors (FETs). However, sputtering treatment during surface preparation alters these stable surface electronic states, and insulating STO can become conductive. This change significantly affects the molecular orientation of deposited organic thin films. Therefore, in this study, STO(100) substrates were sputtered under different incident angles, and their surface states were investigated using near-edge X-ray absorption fine structure (NEXAFS) and ultraviolet photoelectron spectroscopy (UPS) measurements.

The experiments were conducted at BL-8 of the SR Center at Ritsumeikan University. Nb-doped (0.05 wt%) STO(100) substrates, polished to a mirror finish on one side, were used. First, untreated STO substrates were prepared, and sputtering was then performed in the measurement chamber using a sputter gun operated at an acceleration voltage of 1.0 kV and a filament emission current of 20 mA for 30 minutes. Ar gas was used for sputtering, and the incident angle was set either parallel (90°) or perpendicular (0°) to the substrate surface. UPS and NEXAFS measurements were carried out on the substrates.

Figure 1 shows the valence band spectra of STO measured by UPS after surface treatment under different conditions. The peak around 1.0 eV is attributed to Ti 3*d* defect states, indicating the reduction of Ti^{4+} to Ti^{3+}. A significant difference in peak intensity was observed between Ar^+ sputtering incident angles of 90° and 0°. This suggests that 90° incidence (parallel to the substrate surface) minimizes the ion penetration depth, limiting the sputtering effect to the near-surface region and preventing damage to the subsurface, thereby preserving the insulating properties of the surface [1]. These results indicate that the sputtering process exhibits a clear angular dependence.

Figure 2 shows the Ti *L*-edge NEXAFS spectra. Peak splitting is observed in the energy ranges of approximately 455–460 eV and 461–465 eV. This splitting originates from crystal field splitting of the Ti–O bonds, where the lower-energy peaks are attributed to the t_{2g} orbitals and the higher-energy peaks to the e_g orbitals. Compared with the untreated STO surface, the peak splitting becomes significantly distorted after Ar^+ sputtering, as shown in Fig. 2. This indicates that Ar^+ sputtering strongly disrupts the local Ti–O structure and reduces the symmetry of the system, resulting in an amorphous-like STO surface [2].

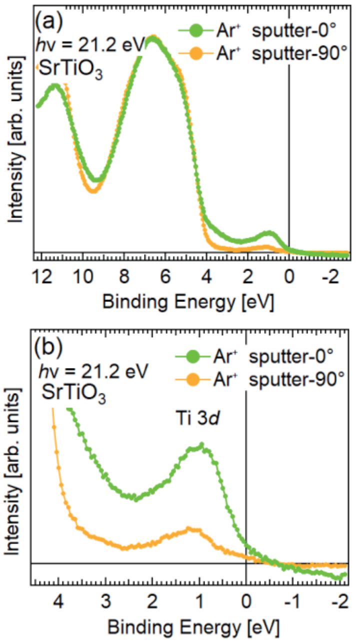

Figure 1. Valence band spectra of STO measured by UPS after surface treatment under different sputtering conditions: (a) wide-range and (b) near the Fermi level.

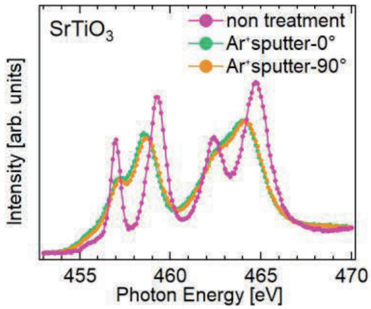

Figure 2. Ti *L*-edge NEXAFS spectra of STO before and after Ar^+ sputtering.

References

[1] Y. K. Wakabayashi *et al.*, J. Appl. Phys. **137**, 095305 (2025).
[2] J. E. Medvedeva *et al.*, Phys. Rev. Mater. **6**, 075605 (2022).

Local Structure Analysis of Amorphous Zirconia by Tender X-ray Absorption Fine Structure

Hideki Hashimoto[1], Yuta Shuseki[2], Takato Abe[1], Manami Yamada[1],
Juan Carlos Palomares Gines[2] , Toyonari Yaji[3], Atsunobu Masuno[2]
1) Applied Chemistry and Chemical Engineering Program, Kogakuin University, 2665-1 Nakano, Hachioji, Tokyo 192-0015, Japan
2) Graduate School of Engineering, Kyoto University, Kyotodaigaku-Katsura, Nishikyo-ku, Kyoto 615-8520, Japan
3) The SR Center, Ritsumeikan University, 1-1-1 Noji-Higashi, Kusatsu 525-8577, Japan

Zirconia is widely used as a crystalline material because of its excellent heat resistance, corrosion resistance, and mechanical strength. In contrast, amorphous zirconia is expected to be a high-permittivity material, however, its atomistic structure, *e.g.*, the local coordination environment around Zr, has not yet been clarified. Although our previous Zr *K*-edge XAFS measurements suggested that the average Zr–O coordination number in amorphous zirconia is approximately seven, this was not consistent with other structural analysis results. In this study, we carried out Zr L_2- and L_3-edge XANES experiments [1,2], which are sensitive to the local structure around Zr, to clarify the features of the ZrO_n polyhedra in amorphous zirconia.

Zr *L*-edge XAFS experiments were carried out at the tender X-ray beamline BL-10 of the SR Center, Ritsumeikan University. The incident beam was monochromatized using a Ge(111) double-crystal. Samples were mounted on a carbon sheet and placed in a high-vacuum chamber. X-ray absorption spectra were collected in the fluorescence yield mode. The photon energy was calibrated using the white line peak at 2153.00 eV in the P K-edge XANES spectrum of a $FePO_4$.

Fig. 1 shows the XANES spectra obtained in this study. The Zr $L_{2,3}$-edge XANES spectra mainly originate from transitions from the 2p orbitals to the 4d orbitals, and strongly reflect the coordination number, symmetry, and Zr–O bond distance of the ZrO_n polyhedra [1,2]. For $Ca_3ZrSi_2O_9$ with ZrO_6, two peaks corresponding to crystal-field splitting were clearly observed. In contrast, for m-ZrO_2 with highly distorted ZrO_7, the separation between the two peaks was unclear. In addition, no clear splitting was observed for $ZrSiO_4$ with ZrO_8. The Zr $L_{2,3}$-edge XANES spectra of amorphous zirconia were clearly different from those of six-coordinated $Ca_3ZrSi_2O_9$ and eight-coordinated $ZrSiO_4$, and showed similar spectral shape to seven-coordinated m-ZrO_2. This indicates that the ZrO_n polyhedra in amorphous zirconia have a local structure similar to the highly distorted seven-coordinated polyhedra found in m-ZrO_2. In addition, the splitting energies at the L_3- and L_2-edges of amorphous zirconia were slightly smaller than those of m-ZrO_2. This may reflect either a slightly longer Zr–O bond distance or a greater distortion of the ZrO_n polyhedra in amorphous zirconia. These results suggest that the amorphous zirconia samples prepared in this study have relatively highly coordinated and highly distorted ZrO_n polyhedra, in contrast to the six-coordinated polyhedra commonly found in conventional oxide glasses. Such a local structure is close to that of highly coordinated polyhedra reported for densely packed Al_2O_3–SiO_2–ZrO_2 glasses synthesized by aerodynamic levitation method [1], suggesting a densely packed atomic arrangement in amorphous zirconia.

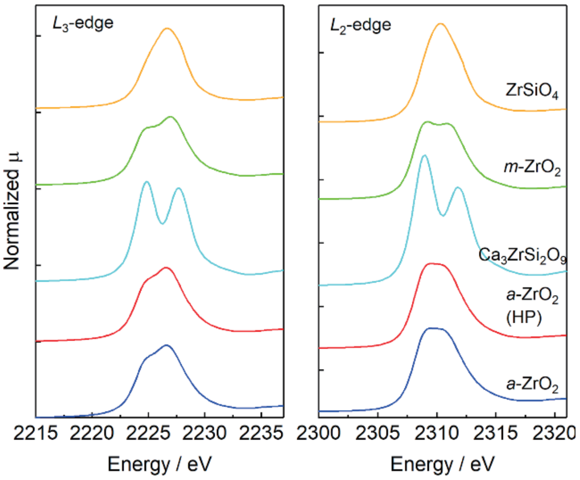

Fig. 1 Zr $L_{2,3}$-edge XANES spectra of amorphous zirconia (a-ZrO_2), amorphous zirconia treated at 6 GPa at room temperature (a-ZrO_2 (HP)), and the reference samples $Ca_3ZrSi_2O_9$, m-ZrO_2, and $ZrSiO_4$.

References

[1] A. Masuno *et al.*, *Acta Mater.* **2025**, *283*, 120549.
[2] M. Ficheux *et al.*, *J. Non-Cryst. Solids* **2020**, *539*, 120050.

Investigation of the Charge-Discharge Reaction Mechanism of an SiO_2/C Anode Prepared from Rice Husks Using XAFS

Ayuko Kitajou [1], Sota Matsumoto [1], Toyonari Yaji [2], Yuki Orikasa [3]

1) *Graduate School of Sciences and Technology for Innovation, Yamaguchi University, 2-16-1 Tokiwadai, Yamaguchi Ube, 755-8611, Japan*
2) *The SR Center, Ritsumeikan University, 1-1-1 Noji-Higashi, Kusatsu, Shiga, 525-8577, Japan*
3) *Department of Applied Chemistry, Ritsumeikan University, 1-1-1 Noji-Higashi, Kusatsu, Shiga, 525-8577, Japan*

Silicon oxide–based anode materials have attracted increasing attention for next-generation lithium-ion batteries because of their high theoretical capacity and improved cycling stability compared with silicon anodes. However, because SiO and SiO_2 have lower electrical conductivity than carbon and silicon, the use of a high content of conductive additives (e.g., carbon black) is required when they are employed as anodes. Therefore, designing carbon composite materials in which SiO or SiO_2 is uniformly dispersed is considered essential for improving the overall electrochemical performance. Recently, examples focusing on biomass as a precursor for such anode materials have begun to be reported [1)]. Among these, rice husks are considered a promising precursor because they consist of a composite of silicates and organic compounds such as cellulose and lignin, which are required for the preparation of SiO_2/C. However, their reversible capacity remains limited to about 200–400 mAh/g, which is comparable to that of graphite anodes [2, 3)]. Electrochemical characterization has revealed that SiO^2/C derived from rice husks exhibits a lower reversible capacity than SiO_2/C obtained from a model material consisting of a lignin–SiO_2 mixture. To investigate the origin of this difference, the oxidation state of Si in the electrodes was examined after lithium insertion and extraction.

Figure 1 shows the Si K-edge XANES spectra measured at the points indicated in Figure 2 using (a) PFY mode and (b) TEY mode. These measurements were carried out at BL-10 at the SR Center of Ritsumeikan University. In the initial state, a clear peak was observed at 1846 eV, and the peak position remained unchanged up to a state of charge (SOC) of 63% in both PFY and TEY modes. Upon further lithiation to SOC = 100%, the peak position shifted toward lower energy. In addition, a new peak appeared at approximately 1840 eV at SOC = 100%; however, its relatively low intensity suggests that the conversion reaction to metallic silicon was limited. Furthermore, even after the delithiation process, neither the peak features nor the position of the Si K-edge XANES spectra changed. These results indicate that the conversion reaction of SiO_2 during lithium insertion is essentially irreversible, and that recombination between lithium-containing oxide/silicate phases and metallic Si does not readily occur during delithiation. Moreover, the overall extent of spectral change in the Si K-edge XANES spectra was smaller than that observed previously for the model material. This suggests that the electrochemical activity of SiO_2 in the SiO_2/C-RH composite is lower than that in the model material. Such reduced activity is considered to be responsible for the decrease in reversible capacity.

References

[1] W. Tao, C. Xu, P. Gao, K. Zhang, X. Zhu, D. Wu, and J. Chen, *J. Coll. Interface Sci.*, **2024**, 669, 902.
[2] Y. Abe, M. Tomioka, M. Kabir, and S. Kumagai, *Scientific Reports*, **2022**, 12, 975.
[3] S. Kumagai, Y. Abe, M. Tomioka, and M. Kabir, *Scientific Reports*, **2021**, 11(1), 15784.

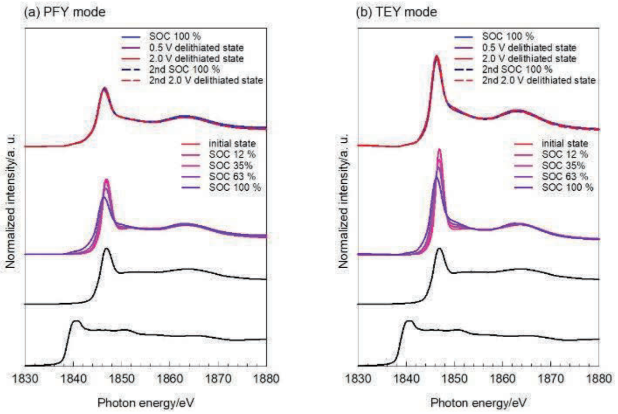

Fig. 1 Si K-edge XANES spectra of various electrodes measured in (a) PFY mode and (b) TEY mode.

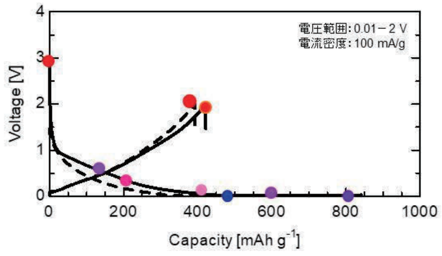

Fig. 2 Charge–discharge curves of the obtained samples and the corresponding measurement points.

Local Structure Analysis of Electrolyte and Electrode Materials Being Applicable in Oxide-Based All-Solid-State Batteries by Soft X-ray Absorption Fine Structure Measurements

Tomonari Takeuchi[1], Yushi Fujita[1], Toyoki Okumura[1], Daisuke Shibata[2], and Toyonari Yaji[2]

1) National Institute of Advanced Industrial Science and Technology (AIST), 1-8-31 Midorigaoka, Ikeda, Osaka 563-8577, Japan
2) SR Center, Ritsumeikan University, 1-1-1 Noji-Higashi, Kusatsu 525-8577, Japan

Among the currently developed next-generation battery systems, all-solid-state batteries (ASSB) have advantages to show higher volumetric energy density, and in addition, oxide-based ASSB show higher safety because of the absence of flammable organic liquid electrolyte. For realizing high-performance oxide-based ASSB, the most important issue is the development of oxide-based solid electrolyte with high ionic conductivity.

Recently, pyrochlore-type solid electrolyte ($Li_{1.25}La_{0.58}Nb_2O_6F$; LLNOF) has been reported to show higher ionic conductivity (*ca*. 7 mS/cm as bulk conductivity [1]) than those reported so far for oxide-based electrolytes. Such higher ionic conductivity nearly corresponds to liquid electrolytes and would be plausibly applicable for assembling ASSB. This material can be prepared by conventional solid-state reaction, as well as using spark-plasma-sintering equipment [2]. Although the resulting LLNOF samples from both synthesis routes showed similar XRD patterns, the oxidation state should be checked because of the difference in the synthesis conditions.

In the present study, we have carried out Nb L-edge X-ray absorption fine structure (XAFS) measurements for the LLNOF samples prepared by conventional solid-state reaction (SS sample) and using SPS equipment (SPS sample) in order to examine the oxidation state and local structure of Nb. We also carried out Co and Mn L-edge XAFS measurements for $LiCoO_2$-Li_2MnO_3 (LCMO) cathode materials, assuming to assemble the (LCMO+LLNOF)/LLNOF/Li ASSB. In this case, $Li_{3.5}Ge_{0.5}V_{0.5}O_4$ (LGVO) solid electrolyte [3] was practically used instead of LLNOF because of the established ASSB assembling method using LGVO. XAFS measurements were carried out at the beamlines BL-10 and 11 in the Synchrotron Radiation Center, Ritsumeikan University. Spectra were taken with the total electron yield (TEY) mode.

Figure 1 shows the measured Nb L-edge XAFS spectra for the LLNOF SPS and SS samples. The spectra for NbO, NbO_2, and Nb_2O_5 are also shown for comparison. The LLNOF samples showed similar spectra irrespective of the synthesis routes, and the edge positions were close to that of Nb_2O_5, indicating that the valence of Nb was 5+ in both samples.

Figure 2 shows the Co L-edge XAFS spectra for the LCMO samples before electrochemical test and after charge and discharge. For Li extraction and insertion reactions, the edge position shifts to higher and lower energy, indicating that Co shows oxidation and reduction, respectively. Thus, the present LCMO sample was confirmed to be applicable as cathode material in ASSB.

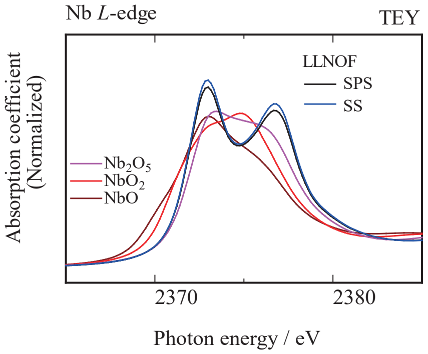

Fig. 1 Nb L-edge XAFS spectra for the LLNOF SPS and SS samples.

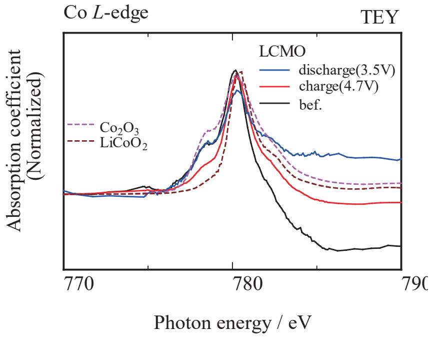

Fig. 2 Co L-edge XAFS spectra for the LCMO samples before electrochemical test and after charge and discharge.

References

[1] A. Aimi, et al., *Chem. Mater.*, **36**, 3717 (2024).
[2] Y. Fujita, et al., *ACS Materials Lett.*, **8**, 1080 (2026).
[3] T. Okumura et al., *ACS Appl. Energy Mater.*, **4**, 30 (2021).

Si K-edge XAS Study on Charged and Discharged Si Anode of All-solid-state Battery

Nodoka Ishikawa[1], Toyonari Yaji[2], Chengchao Zhong[1], Keiji Shimoda[3],
Ken-ichi Okazaki[2], and Yuki Orikasa[1]

1) *Department of Applied Chemistry, Ritsumeikan University, Kusatsu 525-8577, Japan*
2) *Research Organization of Science and Technology, Ritsumeikan University, Kusatsu 525-8577, Japan*
3) *Ritsumeikan Global Innovation Research Organization, Ritsumeikan University, Kusatsu 525-8577, Japan*

Silicon (Si) for lithium alloyed host has an extremely high theoretical capacity compared to graphite, making it a promising candidate for anode materials in lithium-ion batteries and all-solid-state batteries. However, significant volume changes associated with lithium alloying and dealloying lead to poor cyclability due to particle pulverization, mechanical degradation of the composite electrode structure, and continuous electrolyte decomposition. Although degradation analyses of Si anodes have been conducted primarily using liquid electrolytes, the degradation behavior could be different in solid electrolytes due to crack formation and mechanical contact loss at the interface [1]. While reaction mechanisms in liquid and solid electrolytes have been reported individually, how the Li–Si reaction and structural evolution behavior differ between liquid and solid electrolytes for the same Si active material remains poorly understood. Therefore, this study investigates differences in lithiation and delithiation behavior between liquid- and solid-electrolyte systems using half-cells using Si anode by Si K-edge X-ray absorption spectroscopy (XAS).

Si particles with an average diameter of 8 µm were used as the active material. Half-cells using composite electrodes were assembled and charge-discharge measurements were performed at 0.05C rate. After the initial charged, the cells were disassembled and transferred into XAS measurement chamber without air-exposure. Si K-edge XAS measurements were conducted at the beamline BL-10 of the SR Center, Ritsumeikan University, using the partial fluorescence yield (PFY) mode.

Figure 1(a) and (b) show Si K-edge X-ray absorption near edge structure (XANES) spectra of Si composite electrodes for all-solid-state cells and liquid-electrolyte cells, respectively. The spectra were collected from pristine electrodes and electrodes lithiated to 1500 mAh g^{-1}.

In the all-solid-state cell, no appreciable change in the peak position or spectral shape was observed after lithiation. In contrast, after lithiation, the liquid-electrolyte cell showed a marked decrease in the intensity of the absorption peak near 1841 eV, which is characteristic of crystalline Si. This spectral change suggests that Li alloying altered the electronic structure of crystalline Si, consistent with the formation of a lithiated Si phase with enhanced metallic character, whereas the crystalline Si structure was largely retained in the all-solid-state cell.

These results indicate that the lithiation behavior of Si differs substantially between the two electrolyte systems. The limited spectral change observed in the all-solid-state cell suggests that the Li–Si reaction might be suppressed or proceeded heterogeneously under the present conditions, possibly due to restricted Li transport and/or insufficient mechanical contact at the Si/solid-electrolyte interface.

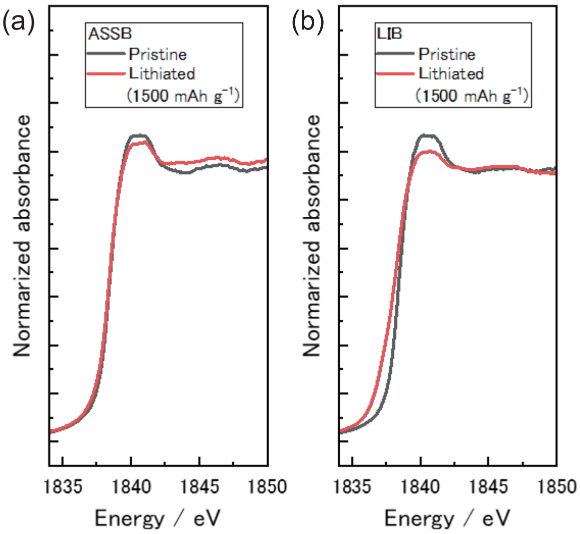

Figure 1. Si K-edge XANES spectra Si composite electrodes measured in PFY mode for (a) all-solid-state cells and (b) liquid-electrolyte cells at pristine, lithiated (1500 mAh g^{-1}) state.

References

[1] M. Matsumoto, Y. Sakka, CC. Zhong, K.Shimoda, KI. Okazaki, H. Yamashige, T. Ozeki, T. Matsui, A. Takeuchi, M. Uesugi, K. Uesugi, and Y. Orikasa, *ACS Nano* , 19, 36527-36535 (2025).

Analysis of Degradation Mechanisms in Sulfur Cathodes Using Soft X-rays

Koki Nakamura[1], **Taichi Kida**[1], **Minako Deguchi**[1], **Daisuke Shibata**[2], **Masashi Ishikawa**[1]
1) Department of Chemistry, Materials and Bioengineering, Kansai University,
3-3-35Yamate-cho, Suita 564-8680, Japan
2) SR Center, Ritsumeikan University, 1-1-1 Noji-Higashi, Kusatsu 525-8577, Japan

Lithium-sulfur (Li-S) batteries hold great promise owing to the high theoretical specific capacity (1672 mAh g^{-1}) and the natural abundance of sulfur. However, their practical application is hindered by critical challenges, most notably the dissolution of sulfur species into the electrolyte. To improve the energy density of Li-S batteries, we have focused on suppressing this dissolution by encapsulating sulfur within porous carbon. In particular, we previously reported that combining this approach with a film-forming electrolyte effectively suppresses the dissolution of intermediate polysulfides, enabling high capacity [1].

However, the initial irreversible capacity and capacity degradation during long-term cycling remain unresolved issues, and their underlying mechanisms have not yet been fully understood. To investigate these mechanisms, in this study, we analyzed the local structure and electronic states of the porous carbon cathode using carbon K-edge X-ray absorption near-edge structure (XANES) spectroscopy.

The electrodes were prepared by mixing a porous carbon-sulfur composite, a conductive additive (acetylene black), and binder (carboxymethyl cellulose and styrene-butadiene rubber) in a predetermined weight ratio to form a slurry, which was coated onto etched aluminum foil and dried. Two-electrode flat cells were assembled using the fabricated cathode, a lithium metal counter electrode, and an electrolyte consisting of 1 M LiTFSI dissolved in fluoroethylene carbonate (FEC) and hydrofluoroether (HFE). After galvanostatic cycling, the cells were disassembled, and the cathodes were washed prior to XANES measurements.

Fig. 1 shows the carbon K-edge XANES spectra of the electrode obtained by TEY. In TEY measurements, peaks attributed to C=C π*, C=O π*, and C–C σ* were clearly observed [2]. Coating components, such as Li_2CO_3 and poly-VC, became prominent after the first discharge and subsequently decreased during charging. This behavior suggests that the SEI undergoes repeated partial dissolution and reformation during cycling, indicating its dynamic and unstable nature.

Fig. 2 presents the corresponding carbon K-edge XANES spectra obtained by PFY. The PFY measurements showed that the C=C π* peak near 284.3 eV decreased in the discharged state. This decrease suggests lithium insertion into the graphite structure of carbon. Such lithium insertion is considered to induce progressive structural degradation of the graphite during repeated charge–discharge cycles, ultimately resulting in irreversible damage to the electrode.

Based on these results, the degradation of this system is attributed to both the instability of the SEI and lithium insertion into the porous carbon. The cycle performance is expected to be improved by optimizing the voltage window, carbon materials, and electrolyte design.

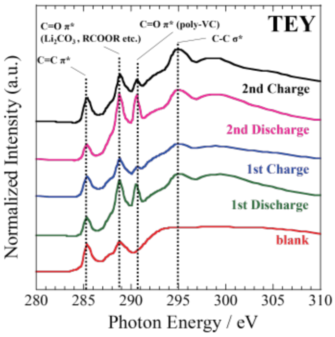

Fig. 1 C K-edge XANES spectra for each state observed in TEY mode.

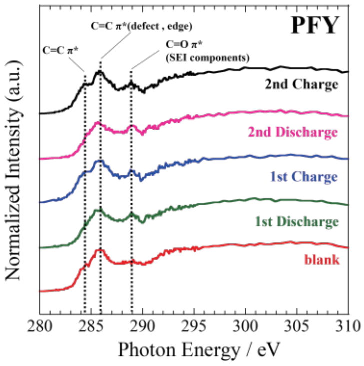

Fig. 2 C K-edge XANES spectra for each state observed in PFY mode.

References
[1] Y. Torii, Y. Matsui, K. Yamamoto, S. Uchida, S. Yamazaki, T. Watanabe, K. Nakanishi, T. Uchiyama, Y. Uchimoto, and M. Ishikawa, *J. Phys. Chem. C*, **2023**, *127*, 15069.
[2] T. Hakari, Y. Kameoka, K. Kishida, S. Ozaki, C. Murata, M. Deguchi, A. Shiratori, Y. Matsui, T. Hosokawa, M. Tanaka, Y. Asari, and M. Ishikawa, *Carbon Energy*, **2024**, *6*, e585.

Surface Analysis on Lanthanum Nickel Oxides for Alkaline Water Electrolysis Anode by O K-edge X-ray Absorption Spectroscopy

Shunsuke Okubo[1], Junichi Kurokawa[1], Daisuke Shibata[2], Chengchao Zhong[1],
Keiji Shimoda[3], Ken-ichi Okazaki[2] and Yuki Orikasa[1]

1) *Department of Applied Chemistry, Ritsumeikan University, 1-1-1 Noji-Higashi, Kusatsu 525-8577, Japan*
2) *Research Organization of Science and Technology, Ritsumeikan University, 1-1-1 Noji-Higashi, Kusatsu 525-8577, Japan*
3) *Ritsumeikan Global Innovation Research Organization, Ritsumeikan University, 1-1-1 Noji-Higashi, Kusatsu 525-8577, Japan*

Perovskite-type nickel oxide catalysts are among the candidate anode materials for alkaline water electrolysis. Previous studies have reported that the surface structure of perovskite oxygen evolution reaction (OER) catalysts can change under OER operating conditions [1], meaning the bulk electronic state may not always correlate with OER activity. A recent study evaluating $LaNiO_3$ and La_2NiO_4 reported that after an alkaline pretreatment, the OER current of La_2NiO_4 increased by a remarkable 45-fold compared to the untreated sample [2]. This suggests that surface modifications induced by alkaline treatment can have a significant impact on OER performance.

In our previous study, while no significant peak changes were observed for $LaNiO_3$ after alkaline treatment, a complete disappearance of the pre-edge peak around 528 eV was confirmed for La_2NiO_4 [3]. This suggests changes in orbital hybridization induced by the alkaline treatment, likely reflecting structural differences between the perovskite and Ruddlesden-Popper (RP) phases; however, the details remain to be fully elucidated. In this study, we focus on $La_3Ni_2O_7$ and $La_4Ni_3O_{10}$, which were not investigated in our previous research, to examine the effects of alkaline treatment on their crystal structure, surface electronic structure, and OER activity.

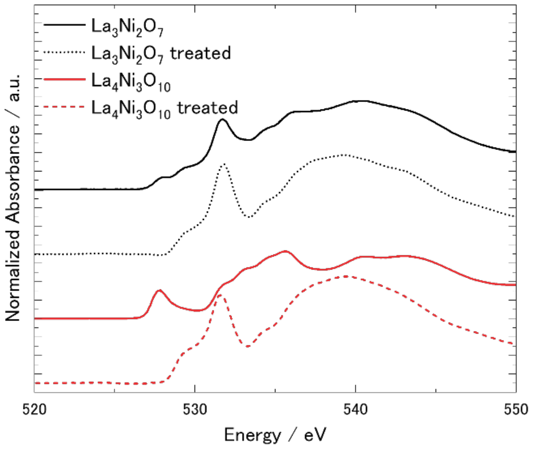

Fig. 1 O K-edge XAS of $La_3Ni_2O_7$ and $La_4Ni_3O_{10}$ powders before and after the alkaline treatment.

Figure 1 shows the O K-edge X-ray absorption spectra of $La_3Ni_2O_7$ and $La_4Ni_3O_{10}$. In the present results, the disappearance of the peak around 528 eV after the alkaline treatment was confirmed for both samples. This trend is consistent with our previous findings for La_2NiO_4, further supporting the idea that these results reflect the structural differences between the perovskite and RP phases.

Considering both the previous and present results, while the surface structure of $LaNiO_3$ with a perovskite-type structure remains relatively stable even after concentrated alkaline treatment, a distinct transformation of the surface structure was confirmed for all three samples possessing RP structure. Regarding this surface structural change, previous studies on perovskite-structured samples have reported that the dissolution of metal atoms leads to the formation of a surface reconstruction layer composed of Ni and O [4]. We currently hypothesize that the surface changes observed in this study occur through a similar mechanism; however, sufficient analysis has not yet been conducted. Therefore, we plan to perform further characterization using X-ray photoelectron spectroscopy (XPS) and energy-dispersive X-ray spectroscopy (EDX) to achieve a detailed understanding of the surface reconstructed layers

References

[1] E. Fabbri, M. Nachtegaal, T. Binninger, X. Cheng, B.-J. Kim, J. Durst, F. Bozza, T. Graule, R. Schäublin, L. Wiles, M. Pertoso, N. Danilovic, K. E. Ayers and T. J. Schmidt, *Nat. Mater.*, **2017**, *16*, 925.

[2] Y.-H. Wu, M. Janák, P. M. Abdala, C. N. Borca, A. Wach, A. Kierzkowska, F. Donat, T. Huthwelker, D. A. Kuznetsov and C. R. Müller, *J. Am. Chem. Soc.*, **2024**, *146*, 11887.

[3] S. Okubo, Y. Ikeda, D. Shibata, C. Zhong, K. Shimoda, K. Okazaki and Y. Orikasa, *Mem. SR Center Ritsumeikan Univ.*, **2025**, 27, 6.

[4] J. H. Montoya, L. C. Seitz, P. Chakthranont, A. Vojvodic, T. F. Jaramillo, J. K. Nørskov, *Nat. Mater.*, **2017**, 16, 70.

Comparative P *K*-edge XAFS Analysis of Black Phosphorus, GaP, and Ni_2P

Naoyuki Maejima and Masaru Takizawa
Department of Physical Sciences, Faculty of Science & Engineering, Ritsumeikan University,
1-1-1 Noji-Higashi, Kusatsu 525-8577, Japan

Phosphorus is a typical element with multiple allotropes, and phosphorene, which is a two-dimensional allotrope of phosphorus, has attracted significant attention due to its intriguing physical properties. X-ray absorption fine structure (XAFS) measurements are able to investigate the electronic states and local coordination of such materials. In this short note, we measured the P *K*-edge XAFS of a Black Phosphorus crystal, a GaP(100) wafer, and a Ni_2P(10-10) single crystal as candidate reference samples for analysis.

Measurements were performed at BL-13 of the SR Center, Ritsumeikan University. P *K*-edge spectra were obtained from a crystalline bulk black phosphorus sample, a GaP(100) wafer, and a Ni_2P(10-10) single crystal using the total electron yield method.

The XANES spectra of black phosphorus, GaP, and Ni_2P are shown in Fig. 1, where the spectra are plotted as black, red, and blue solid lines, respectively. These spectra show features similar to those reported in the literature.[1-3] Although these materials have different oxidation states, 0 for black phosphorus, −III for GaP, and approximately −I for Ni_2P[4], the absorption-edge positions were estimated from the peak in the first derivative of the spectra, resulting in values of 2143.9 eV for black phosphorus and GaP, and 2143.2 eV for Ni_2P, indicating that the absorption-edge position does not simply follow the oxidation state. Previous studies have reported that, in M_2P systems characterized by similar local coordination environments around P atoms despite differences in the overall crystal structures, there is a correlation between the absorption-edge position and the electronegativity difference between metal and P atoms.[4] Furthermore, absorption-edge positions of GaP and red phosphorus, which have the same oxidation state as black phosphorus, can be understood by considering the sum of the electronegativities of atoms surrounding P atoms.[2] Nevertheless, a more comprehensive framework is required to consistently predict absorption-edge trends across these three systems.

Figure 2 shows the Fourier-transformed EXAFS spectra. The peak position of GaP is slightly higher than those of black phosphorus and Ni_2P, which can be attributed to the longer nearest-neighbor distance from the P atoms (2.35 Å for GaP [6], compared to 2.22 Å for black phosphorus [5] and Ni_2P [7]).

In summary, we succeeded in the measurement of P *K*-edge spectra for the reference samples.

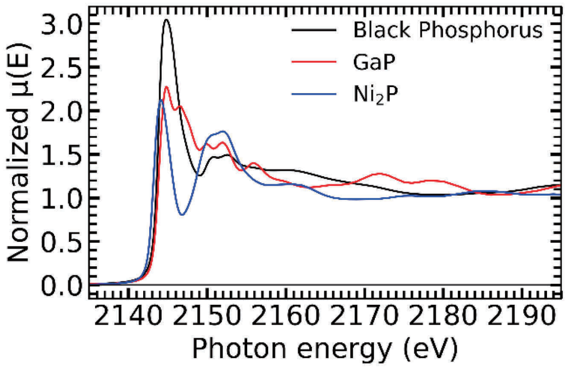

Fig. 1. P *K*-edge XANES spectra of Black Phosphorus (black), a GaP(100) wafer (red) and a Ni_2P(10-10) single crystal (blue).

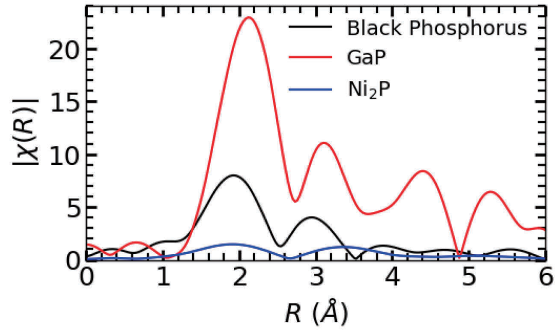

Fig. 2 Fourier-transformed EXAFS spectra of Black Phosphorus (black), a GaP(100) wafer (red) and a Ni_2P(10-10) single crystal (blue).

References

[1] Li, M., *et al.*, *Chem. Mater.*, **33**, (2021) 2029-2036.

[2] Wibowo, R. E., *et al.*, *J. Phys. Chem. C,* **127** (2023) 20582-20593.

[3] Lee, Y., Choi, *et al.*, *J. Mater. Chem. A*, **14** (2026) 988-1000.

[4] Blanchard, Peter ER, *et al.*, *Chem. Mater.,* 20 (2008) 7081-7088.

[5] S. Ichimin, *et al.*, *Physica B,* **190** (1993) 169-176.

[6] Kuz'ma Y.B., *et al.*, *Inorg. Mater.,* **31** (1995) 153-157.

[7] Saravanan, R., *et al.*, *Phys. stat. sol. (b)*, **165** (1991) 67-74.

XPS Insights into the Electrochemical Defluorination of CuF_2 Derivatives in Fluoride-Containing Electrolytes

**Ayaki Ibuka[1], Chengchao Zhong[1], Keiji Shimoda[2], Ken-ichi Okazaki[3],
and Yuki Orikasa[1]**

1) *Graduate School of Life Sciences, Ritsumeikan University, Kusatsu 525-8577, Japan*
2) *Ritsumeikan Global Innovation Research Organization, Ritsumeikan University, Kusatsu 525-8577, Japan*
3) *Research Organization of Science and Technology, Ritsumeikan University, Kusatsu 525-8577, Japan*

Copper fluoride (CuF_2) is a promising positive active material for fluoride shuttle batteries (FSBs) because it has a high theoretical gravimetric capacity of 528 mAh g^{-1} for the reversible conversion reaction of CuF_2 to Cu metal. However, CuF_2 is unstable in the atmosphere and readily reacts with water to form a hydrate ($CuF_2{\cdot}2H_2O$). Furthermore, it has also been suggested that $CuF_2{\cdot}2H_2O$ decomposes to form basic salts, such as copper (II) hydroxyfluoride, in which both fluoride and hydroxide ions are bound to the Cu^{2+} ions in specific ratios of $Cu_{x+1}F_{2x}(OH)_2$: e.g., $Cu_2F_2(OH)_2$ (x=1), $Cu_3F_4(OH)_2$ (x=2), and $Cu_4F_6(OH)_2$ (x=3) [1]. This study utilizes X-ray photoelectron spectroscopy (XPS) to elucidate the defluorination behavior of these CuF_2 derivatives, predominantly composed of $Cu_3F_4(OH)_2$, in an electrolyte solution for FSBs.

Commercially available CuF_2 (TCI, >98%) was used as received. XRD analysis of the material revealed that no diffraction pattern of anhydrous CuF_2, indicating a mixture of copper (II) hydroxyfluoride. The CuF_2 derivative was mixed with acetylene black and a binder to form an electrode sheet. The electrolyte was a solution of tetramethylammonium fluoride (TMAF) and *N*,*N*,*N*-trimethyl-*N*-propylammonium bis(trifluoromethanesulfonyl)amide (TMPA-TFSA) at a molar ratio of 1:50. Galvanostatic defluorination/fluorination was then performed between 0.1 and 1.1 V vs. Pb|PbF_2 at a rate of 0.01C and 298 K. XPS measurements were carried out using a PHI Quantes at SA-1 of the SR Center in Ritsumeikan Univ. with monochromatized Al Kα emission at 1486.7 eV.

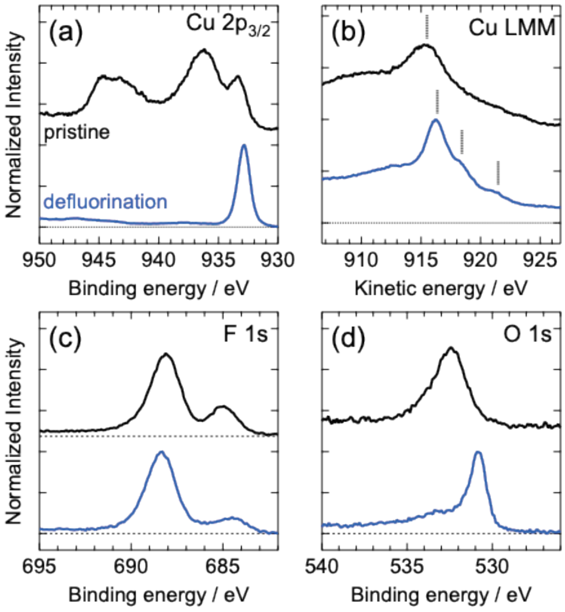

Fig. 1 XPS spectra of (a) Cu $2p_{3/2}$ and (b) Cu LMM Auger electron spectra of the CuF_2 derivatives/C composite electrodes in the pristine state (black) and after defluorination (blue). The corresponding XPS spectra of (c) F 1s and (d) O 1s core levels are also shown.

During the galvanostatic reaction, a defluorination plateau appeared at around 0.4 V with a capacity of approximately 200 mAh (g-CuF_2)$^{-1}$. In the subsequent fluorination, the potential gradually increased to 1.1 V with a capacity of about 100 mAh (g-CuF_2)$^{-1}$. Figure 1 shows the XPS and Auger electron spectra of the CuF_2 derivatives/C composite electrodes before and after defluorination. Fig. 1(a) clearly demonstrates that the peak corresponding to Cu^{2+} species at 936.2 eV disappeared, while a new peak emerged at a lower binding energy of 932.8 eV. Since the Cu 2p spectra of Cu^0 and Cu^+ overlap at this energy, the Cu LMM Auger spectra were analyzed to distinguish these states. In Fig. 1(b), a broad peak at 915.3 eV corresponding to Cu^{2+} was observed in the pristine state. In contrast, after defluorination, a peak assigned to Cu^+ at 916.2 eV and two peaks corresponding to Cu^0 at 918.4 and 921.5 eV emerged. The latter two peaks are the result of multiplet splitting of the Auger transition. In addition, the peak corresponding to Cu-F bonds at 684.7 eV in Fig. 1(c) decreased in intensity, while that for Cu-O bonds at 530.9 eV in Fig. 1(d) appeared after defluorination. These results demonstrate that the CuF_2 derivatives were converted to Cu metal and Cu_2O during the defluorination process. These results were further supported by XRD analysis of the defluorination products.

Reference

[1] P. Ramamurthy and E.A. Secco, *Can. J. Chem.*, **1969**, *47*, 2185.

XPS Study on Lanthanum Nickel Oxide for Alkaline Water Electrolysis Anode

Junichi Kurokawa[1], Shunsuke Okubo[1], Keiji Shimoda[2], Chengchao Zhong[1], Ken-ichi Okazaki[3], and Yuki Orikasa[1]

1) *Department of Applied Chemistry, Ritsumeikan University, 1-1-1 Noji-Higashi, Kusatsu 525-8577, Japan*
2) *Ritsumeikan Global Innovation Research Organization, Ritsumeikan University, 1-1-1 Noji-Higashi, Kusatsu 525-8577, Japan*
3) *Research Organization of Science and Technology, Ritsumeikan University, 1-1-1 Noji-Higashi, Kusatsu 525-8577, Japan*

Nickel-based oxides with a perovskite structure have attracted considerable attention as anodic catalysts for water electrolysis because of their high activity. The perovskite-type water electrolysis catalysts are known to undergo surface structural changes under oxygen evolution reaction (OER) conditions. For example, an active NiOOH surface layer is reportedly formed on the surface of $LaNiO_3$ [1]. In addition, it has been reported that the activity of La_2NiO_4, which possesses a Ruddlesden–Popper structure with a similar composition, is enhanced by alkaline immersion treatment; however, the detailed reason for this improvement has not yet been clarified [2].

In this study, the surface structures of lanthanum nickel oxides, $LaNiO_3$, and Ruddlesden–Popper structure oxides, La_2NiO_4, $La_3Ni_2O_7$ and $La_4Ni_3O_{10}$ were investigated. Both untreated samples and samples immersed in 7 M KOH were compared using X-ray photoelectron spectroscopy (XPS). For all powder samples, the acetylene black was mixed in a mortar for 5 min at a volume ratio of 4:1 for energy calibration. The mixed powders were then pelletized and fixed onto a sample holder using carbon tape. XPS measurements were carried out using a PHI Quantes (ULVAC-PHI) system with Al Kα radiation at Ritsumeikan University SR Center, SA-1.

Fig. 1 shows the Ni 3p core level XPS spectra. Since trivalent $LaNiO_3$ mainly contains Ni^{3+} species, the Ni 3p peak generally appears at approximately 68–71 eV. In contrast, when Ni^{2+} species are present, the peak appears at lower binding energies of approximately 67–69 eV. Therefore, the peak positions are generally expected to appear in the order of La_2NiO_4, $La_3Ni_2O_7$, $La_4Ni_3O_{10}$, and $LaNiO_3$. However, in the present results, the peak positions were observed in the order of $LaNiO_3$, La_2NiO_4, $La_4Ni_3O_{10}$, and $La_3Ni_2O_7$. The Ruddlesden–Popper-type compounds, La_2NiO_4, $La_3Ni_2O_7$, and $La_4Ni_3O_{10}$ exhibited peak shifts toward the higher binding energy side after alkali treatment. Although their original Ni valence states were different (+2, +2.5, and +2.67, respectively), the peak positions after the alkali treatments appeared at nearly the same binding energy. They were observed at higher binding energies than that of $LaNiO_3$ and NiOOH (Ni valence state of +3). These results confirmed that the changes in the Ni 3p spectra after alkali treatment showed different behavior between $LaNiO_3$ and the other samples.

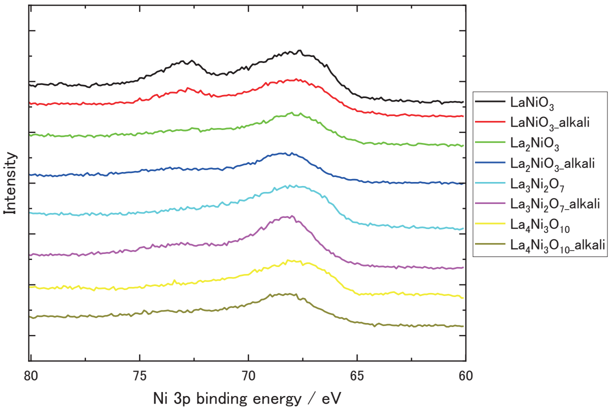

Fig. 1 Ni 3p XPS spectra of $LaNiO_3$, La_2NiO_4, $La_3Ni_2O_7$, and $La_4Ni_3O_7$ before and after alkali treatment.

Reference

[1] Y. Sun, C.-R. Wu, T.-Y. Ding, J. Gu, J.-W. Yan, J. Cheng, and K. H. L. Zhang, *Chem. Sci.*, **2023**, *14*, 5906.

[2] Y.-H. Wu, M. Janák, P. M. Abdala, C. N. Borca, A. Wach, A. Kierzkowska, F. Donat, T. Huthwelker, D. A. Kuznetsov, and C. R. Müller, *J. Am. Chem. Soc.*, **2024**, *146*, 11887.

XPS Study of Interface between Solid Lithium-ion Conductor and Liquid Electrolytes

Yuki Miyaura[1], Keiji Shimoda[2], Chengchao Zhong[1], Ken-ichi Okazaki[3], and Yuki Orikasa[1]

1) *Department of Applied Chemistry, Ritsumeikan University, Kusatsu 525-8577, Japan*
2) *Ritsumeikan Global Innovation Research Organization, Ritsumeikan University, Kusatsu 525-8577, Japan*
3) *Research Organization of Science and Technology, Ritsumeikan University, Kusatsu 525-8577, Japan*

Quasi-solid-state batteries, which operate by adding a liquid electrolyte to a solid electrolyte, are expected to compensate for the disadvantages at the solid-solid interface that occur when using oxide solid electrolytes. However, if the solid electrolyte does not serve as an ion pathway, the overall ionic conductivity becomes low [1]. This is due to the high resistance ($R_{\mathrm{SE/LE}}$) associated with ion transfer at the solid-liquid interface [2]. Therefore, it is important to clarify factors governing this parameter. In this study, we focused on ionic liquids (ILs), for which the origin of this parameter has not yet been fully understood. We investigated how differences in the cation structures of the ILs affect the ion transfer resistance at the solid-liquid interface using electrochemical impedance spectroscopy (EIS) and X-ray photoelectron spectroscopy (XPS).

$R_{\mathrm{SE/LE}}$ was investigated using a two-compartment electrochemical cell containing four electrodes. Each compartment contained two lithium metal electrodes, and was separated by a solid electrolyte. The solid electrolyte was $Li_{1+x+y}Al_x(Ti,Ge)_{2-x}Si_yP_{3-y}O_{12}$ (LATP). The liquid electrolytes were 1 mol dm^{-3} solution of lithium bis(fluorosulfonyl)amide (LiFSA) in 1-ethyl-3-methylimidazolium bis(fluorosulfonyl)amide (EMIFSA), 1-methyl-1-propylpyrrolidinium bis(fluorosulfonyl)amide (Pyr13FSA), and ethylene carbonate (EC) : ethyl methyl carbonate (EMC) (3:7 v/v%). We elucidated this cell using electrochemical impedance spectroscopy (EIS) with a frequency range of 10 mHz to 1 MHz, a potential amplitude of 10 mV, and a temperature range of 263 to 318 K.

After EIS measurements, the LATP samples were washed with acetonitrile in a glove box, XPS measurements were performed using PHI Quantes (ULVAC-PHI) with Al Kα radiation (SR Center, SA-1), and P-2p, N-1s, and Ti-2p core-level spectra were obtained. The binding energy were calibrated using the C-1s peak at 284.6 eV, and the spectra intensity was normalized using the P-2p peak.

The Nyquist plots obtained from impedance measurements showed two semicircles; the lower-frequency semicircle was attributed to $R_{\mathrm{SE/LE}}$. Fitting these semicircles using an equivalent circuit revealed that $R_{\mathrm{SE/LE}}$ decreased in the order of EMIFSA, EC:EMC, and Pyr13FSA.

Fig. 1 shows the core-level XPS spectra of the LATP after EIS using each liquid electrolyte. No significant differences in the binding energies shifts of the N-1s and Ti-2p spectra were observed depending on using the liquid electrolytes. However, the N-1s spectrum of the EMIFSA sample shows intense peaks at 401 eV and 399.5 eV, attributed to decomposition products or residues of imidazolium and LiFSA, respectively. This is probably due to the π-π interactions arising from the aromaticity of the EMIFSA cation, which results in the formation of a dense interfacial layer. It is speculated that this interfacial layer at the solid-liquid interface hinders the lithium-ion transfer, resulting in the increased resistance observed in EIS.

Based on the above results, it was demonstrated that the decomposition products or residues originating from the aromatic EMIFSA cation inhibit lithium-ion transfer at the solid-liquid interface. Therefore, employing non-aromatic cation structures, such as pyrrolidinium, is concluded an effective strategy because it suppresses the formation of a resistive interfacial layer and reduces $R_{\mathrm{SE/LE}}$.

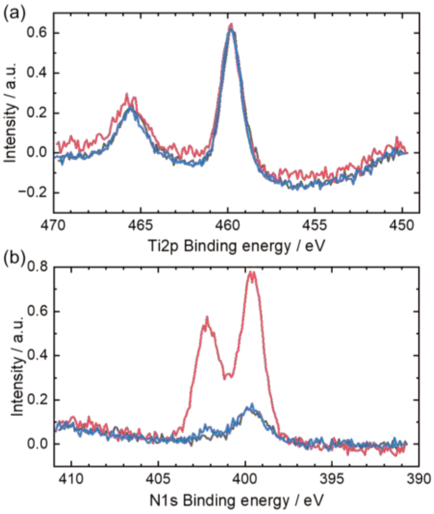

Fig. 1 Core-level XPS spectra of the LATP after EIS using various solutions (black: EC:EMC, red: EMIFSA, blue: Pyr13FSA). (a) Ti-2p, (b) N-1s.

References

[1] M. Liu, *et al.*, *Nat. Nanotechnol.*, **2022**, *17*, 959–967.

[2] T. Suzuki, *et al.*, *Chem. Commun.*, **2025**, *61*, 2953.

STATUS OF THE STORAGE RING

STATUS OF THE STORAGE RING

As a storage ring to be installed at Ritsumeikan University, the superconducting compact storage ring AURORA designed and manufactured by Sumitomo Heavy Industries was chosen, whose details are given elsewhere [1]. After some modifications of the original design, the ring was installed in April 1996 in the Biwako-Kusatsu campus and has successfully been operated since then [2]. Figure 1 shows the storage ring and beamlines in the experimental hall.

Injector is a race-track-type microtron which provides an electron beam of 1 mA at an energy of 150 MeV to the storage ring at a repetition rate of 2 Hz. A 1/2 integer resonance injection method is adopted [3]. The ring is composed of a superconducting weak-focusing single-body magnet, in which the electron orbit is exactly circular with the radius of 0.5 m. The energy of accumulated electron beam is boosted up to 575 MeV synchronously with an increase in the field strength of the magnet. The ring is normally operated at an energy of 575 MeV with an initial beam current of 200 mA. It takes about 100 s to inject an electron beam into the ring and about 8 min to accelerate the electron beam up to 575 MeV. The critical energy of the radiation is 844 eV, higher than that of other rings of approximately the same beam energy. This is due to the smaller radius of the electron orbit in the strong magnetic field, 3.8 T. Table 1 lists the parameters of the ring [4, 5].

Figure 1. Photograph showing the storage ring and beamlines in the experimental hall.

The total operation time of the ring in the fiscal year of 2025 was 778 hours, in which 2 % was used for machine study and tune-up of the ring and all the rest 98 % was used for users' experiments. Integrated beam current (dose, i.e., accumulated beam current multiplied by operation hours) was 58 A･h (ampere-hour). The total user time in the fiscal year was 765 hrs.

In fiscal year 2025, problems due to equipment aging were frequent, including leaks in the cooling water system for the electromagnets, vacuum leaks in the ring vacuum chamber, and helium gas leaks from the helium liquefier system. Maintaining stable operations is becoming increasingly difficult. In recent years, there has been an increase in problems caused by the aging of equipment. Furthermore, in fiscal year 2025, serious problems occurred in the compressor of the helium refrigeration system, and the high voltage power supply for the main ring's RF system was malfunctioning. We plan to conduct several repair and maintenance tasks next fiscal year.

Table 1. Parameters of the injector and storage ring

Injector		
Energy	150	MeV
Repetition	2	Hz
Peak current	1	mA
Pulse width	2	μs
Storage Ring		
Energy	575	MeV
Stored current (e^-)	200	mA
Circumference	3.14	m
Radius of curvature	0.5	m
Field strength	3.8	T
RF frequency	190.86	MHz
Number of cavity	1	
Harmonic number	2	

References

[1] N. Takahashi, *Nucl. Instrum. Methods,* **B24/25** (1987) 425.

[2] H. Iwasaki, Y. Nakayama, K. Ozutsumi, Y. Yamamoto, Y. Tokunaga, H. Saisho, T. Matsubara and S. Ikeda, *J. Synchrotron Radiation*, **5** (1998) 1162.

[3] T. Takayama, *Nucl. Instrum. Methods,* **B24/25** (1987) 420.

[4] Y. Yamamoto, I. Sakai, T. Mitsuhashi, D. Amano and H. Iwasaki, *Nucl. Instrum. Methods,* **A 467-468** (2001) 921-924.

[5] Y. Yamamoto, T. Hori, I. Sakai, K. Yadomi and H. Iwasaki, *Nucl. Instrum. Methods,* **A 533** (2004) 505-508.

STATUS OF THE BEAMLINES

BL-1

Beamline for Extreme Ultraviolet Spectroscopy

Beamline 1 (BL-1) is a beamline for extreme ultraviolet (EUV) spectroscopy. This beamline originally designed and constructed in the Photon Factory was donated in the SR Center of Ritsumeikan University. It was installed at BL-1 with minimum modifications in 2010.

BL-1 consists have a quadrant slit, a pre-focusing mirror, a monochromator, a post-focusing mirror, and experimental port A and B. The whole system was constructed on a base plate of 1 m height. This beamline is designed to accept the direct beam of 10 $\text{mrad}^H \times 3\ \text{mrad}^V$ and to deflect it vertically into the 1 m Seya-Namioka type monochromator.

This beamline has two experimental ports. A photoelectron spectroscopy system Phoibos 100 (SPECS ltd.) was installed at Port A. A EUV irradiation and reflectance measurement system are installed to port B that located up-stream of the port A. Port B can be used to any other experiments by temporal arrangement of the experimental equipment.

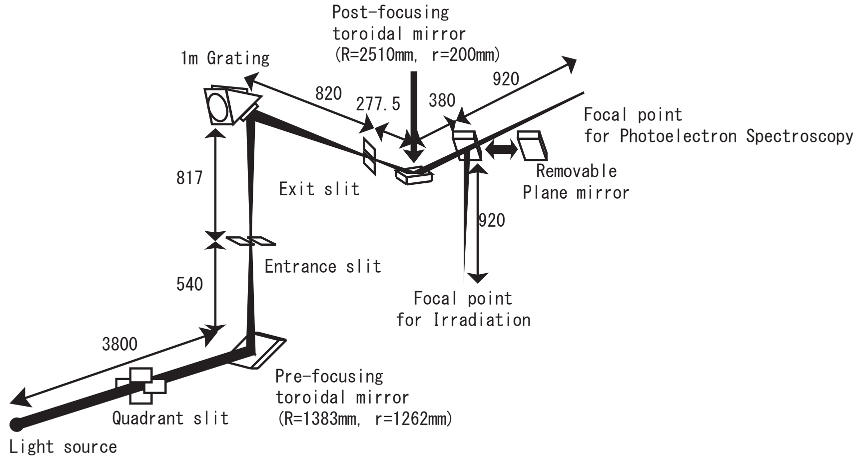

Figure 1: Optical path of BL-1

Specification
Energy range: 5 ~ 50 eV
Energy resolution: $E/\Delta E > 600$ with 50 μm slit width
Photon flux: $1\times10^{11} \sim 1\times10^{12}$ photon/s /200mA
Beam size: 4 mm^H x 2mm^V at sample point
Mirror: pre-focusing mirror (troidal, Au/Si), post-focusing mirror (troidal, Pt/Cu)
Monochromator: 1m grating Seya-Namioka monochromator
Three in-situ exchangeable grating
(Lb = 38, 96, 160 nm), 1200 line / mm
Filter: MgF_2 filter, which can be inserted by straight feedthrough
Measurement:
Photoelectron spectroscopy (UHV condition, Phoibos 100 (SPECS))
EUV irradiation, EUV reflectance (normal incident)

BL-2

Soft X-ray Absorption Spectroscopy

BL-2 is for Ultra soft X-ray beamline for X-ray Absorption Fine Structure (XAFS) spectroscopy. It consists of 4 varied-line-spacing plane gratings which provide ultra-soft X-rays (10^{10}-10^{9} photons) from 35 to 1000 eV [1], Li-K edge to Ni-L edge (Figure 1). The beam size at the sample position is about 0.6mm^{H} × 1.5mm^{V}. The outline of BL-2 is shown in Figure 2.

3 detection modes can be used for XAFS measurements; Total Electron Yield (TEY) and Partial Electron Yield (PEY) and Fluorescence Yield (FY). These are operated simultaneously by the sample current, MCP, and SDD with large detection area (80mm^{2}), respectively. The transfer vessel system [2], common to BL-10, 11 and 13 can be used for samples unstable in air.

[1] H. Ishii et al. Rev. Sci. Instrum. 73, 1541 (2002)

[2] K. Nakanishi, S. Yagi and T. Ohta, IEEJ Trans. EIS 130, 1762 (2010)

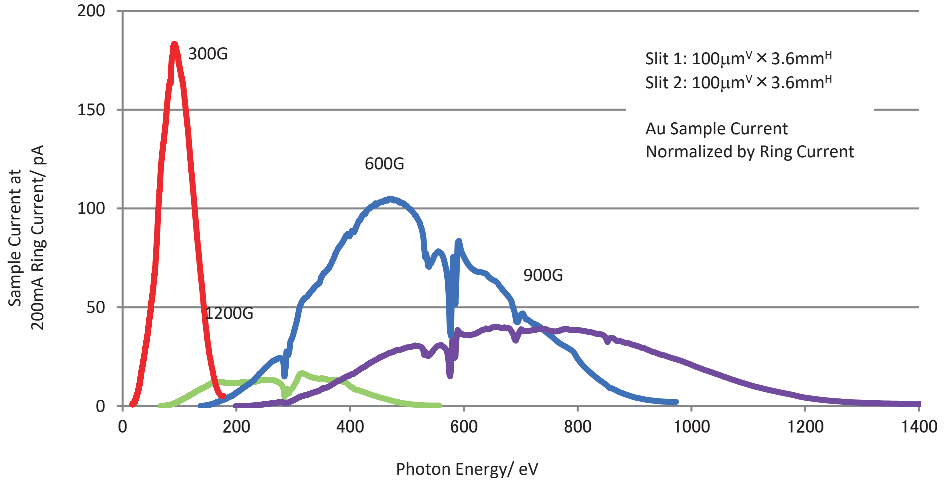

Figure 1 Sample currents from a gold plate measured at BL-2

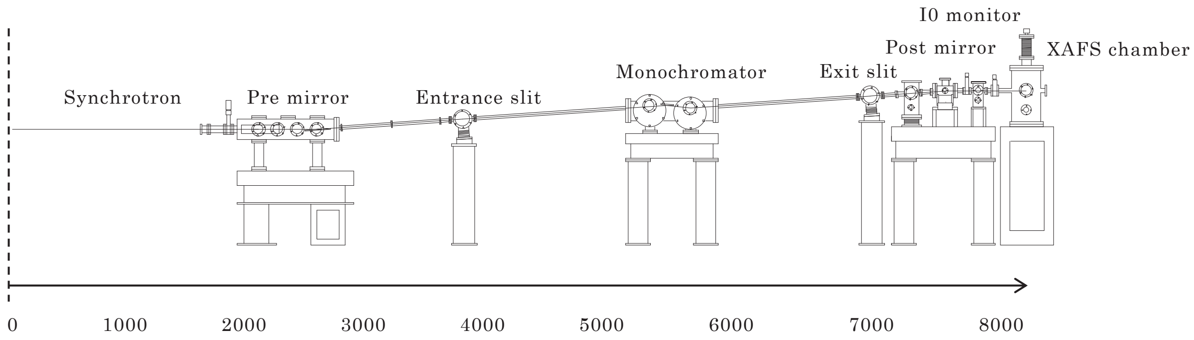

Figure 2 Layout of BL-2

BL-3

X-Ray Absorption Fine Structure (XAFS) Spectroscopy

BL-3 is a general-purpose beamline for XAFS measurements using focused hard X-rays. The overall view and inside the experimental hutch of BL-3 are shown in Figure 1. The outline of BL-3 is shown in Figure 2. White X-rays from the synchrotron are monochromatized by a double-crystal monochromator, and are focused by the Pt-coated toroidal mirror located at 4.5 m from the light source point. The focus size (FWHM) in the experimental hatch is 1 mm (V) × 2 mm (H). The Si crystal in the Golovchenko type monochromator has the size of 30 mm × 30 mm and is larger than that of BL-4. The details of the monochromator are described in the section of BL-4. The large horizontal acceptance at the first monochromator crystal and the application of the focusing mirror contribute to the high X-ray flux at the sample position. The X-ray intensity at BL-3 is about one order larger than that of BL-4. The available energy range of monochromatic X-rays is 3.4-9.1 keV for Si(220) and 2.1-7.6 keV for Si(111). The higher side of the energy range is limited by the cut-off energy of the focusing mirror.

The control system for conventional XAFS measurements was renewed in 2010. The graphical user interface of the control program and the output file format are common with that of BL-4, and are also compatible with those of the Photon Factory (KEK). The quick-scanning XAFS system was installed in 2010 for the transmission mode. The monochromator is continuously scanned during the measurement of a XAFS spectrum.

The standard detector is ionization chamber for the conventional transmission measurements, and various kinds of detection gas are equipped at the experimental hatch. The three-elements solid state detector (SSD) of Ge is available for the fluorescence measurements. The florescence-yield XAFS measurements are very effective for dilute solutions or thin film samples. The XAFS measurements are possible for dilute solutions with the concentration of about 100 ppm and thin films with the sample thickness of about 100 nm.

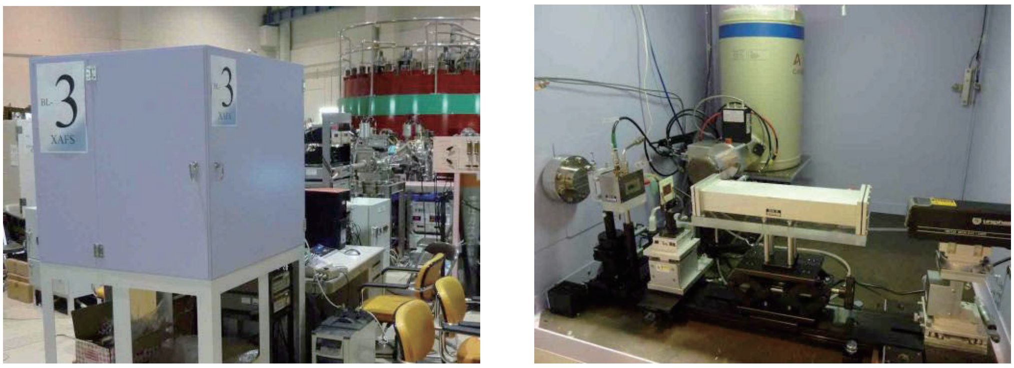

(a) Overall view (b) Inside the experimental hutch

Figure 1 Photo of BL-3

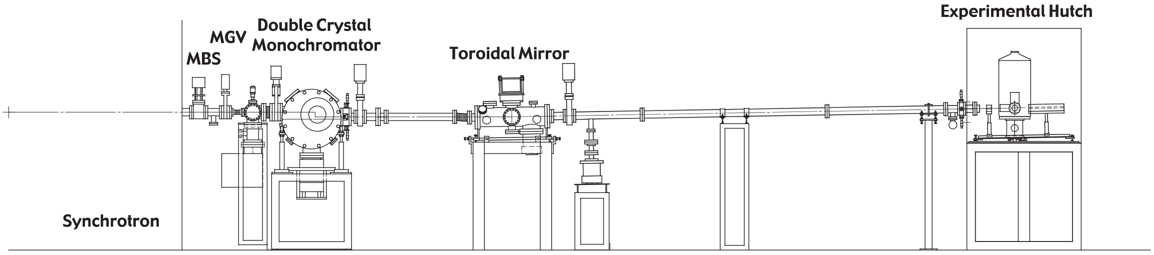

Figure 2 Outline of BL-3.

BL-4

X-Ray Absorption Fine Structure (XAFS) Spectroscopy

BL-4 shown in Figure 1 is a general-purpose beamline for XAFS measurements using unfocused hard X-rays. Figure 2 shows the outline of BL-4. White X-rays are monochromatized by a double-crystal monochromator of the Golovchenko type. Both crystals move along the mechanical guide when the main axis of monochromator is rotated, and the position of exit beam is independent from the X-ray energy. The accessible angle of the monochromator is from 15° to 75°, and thus the available X-ray energy is 1.8-3.5 keV with InSb(111), 3.5-11 keV with Ge(220), and 3.3-11 keV with Si(220). The energy range covers the K edges of 3d transition metals and the L edges of lanthanides. The dimension of the crystal is 20 mm × 20 mm, and the X-ray beam size is normally 10 mm(H) × 1 mm(V) in the experimental hutch.

The ionization chambers with the path length of 4.5 and 31 cm are available for conventional transmission measurements. Some detection gases, N_2 (100 %), N_2 (85 %) + Ar (15 %), N_2 (50 %) + Ar (50 %), and Ar (100 %), can be chosen for the effective detection. The graphical user interface of the control program and the output file format are common with that of BL-3, and are also compatible with those of the Photon Factory (KEK). The quick-scanning XAFS system has been installed for the transmission mode.

The XAFS imaging measurements are also possible at BL-4 by using a two-dimensional detector and the wide monochromatic X-rays. The chemical state of a target element can be selectively analyzed in the area of 5 mm (V) × 10 mm (H) with the spatial resolution of 6.5 μm × 6.5 μm. This system is very powerful for heterogeneous and dynamically changing samples, such as electrodes of battery and solid catalysts.

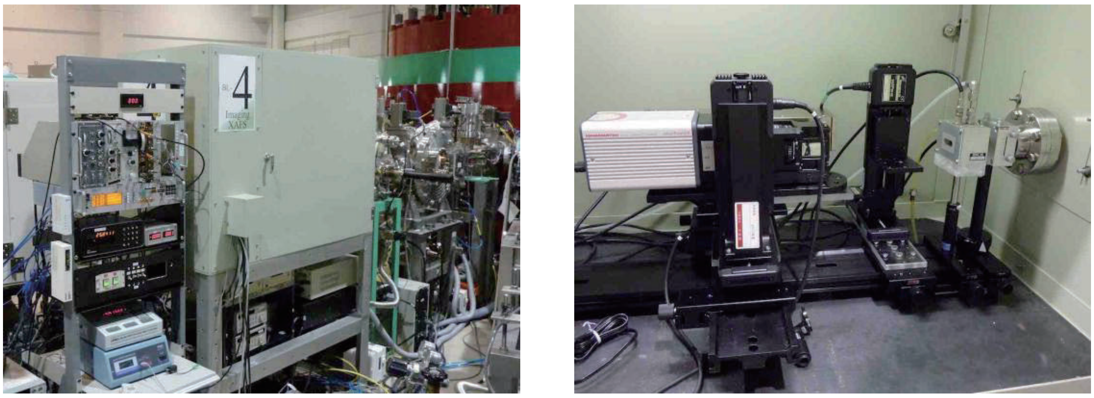

(a) Overall view (b) Inside the experimental hutch

Figure 1 Photo of BL-4.

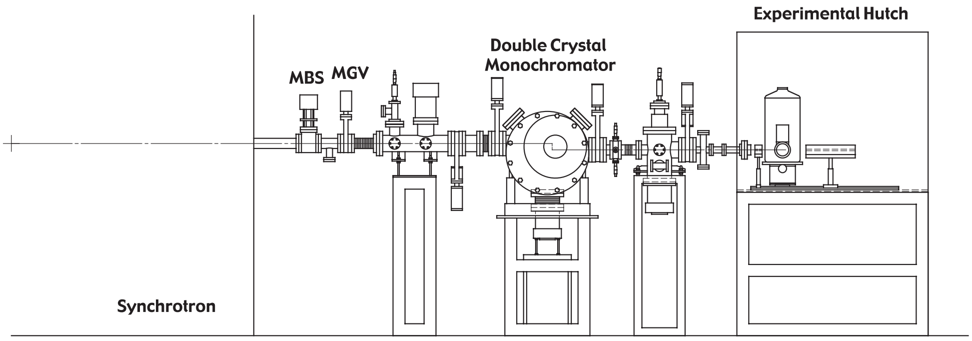

Figure 2 Outline of BL-4.

BL-5

Dispersive X-Ray Absorption Fine Structure (DXAFS) Spectroscopy

BL-5 is a XAFS beamline for time-resolved measurements using dispersive optics with a white X-ray beam and a polychromator. Figure 1 shows the outline of BL-5. A white X-rays are introduced into the experimental hatch and are monochromatized by a bent crystal polychromator. The wavelength-dispersed X-rays are focused at the sample position, and the transmitted X-rays are diverged again. The X-ray intensities are measured using a position-sensitive detector, and the whole X-ray energy range is covered by a single detection at the same time. A XAFS spectrum is thus simultaneously measured without any mechanical movements such as the monochromator scan. The time-resolution of DXAFS measurements depends on the sample conditions. It has been confirmed that a few seconds of the exposure for one spectrum is enough for the XANES analysis at the K edge of 3d metal elements. The measurable absorption edges are limited by the accessible range of the 2θ bench in the experimental hatch and by the available bent crystal as the polychromator. The time-resolved DXAFS technique is very useful to analyze the dynamic behavior of chemical reactions not only in solutions but also in the solid phase. The chemical conversion of supported metal catalysts is a promising target of this beamline.

In addition to the conventional DXAFS system, a new DXAFS optics has been developed in BL-5 (Figure 2). The space- and time-resolved analysis is possible using the Vertically DXAFS (VDXAFS) instrument installed at BL-5. Furthermore, the R&D for multi-element time-resolved DXAFS measurement is in progress to monitor simultaneously at two absorption edges for the analysis of the correlated chemical conversions of two elements. The development of these instruments is supported by the RISING & RISING-II project (NEDO), and they are expected to apply to the analysis of electrochemical reactions in lithium ion secondary batteries.

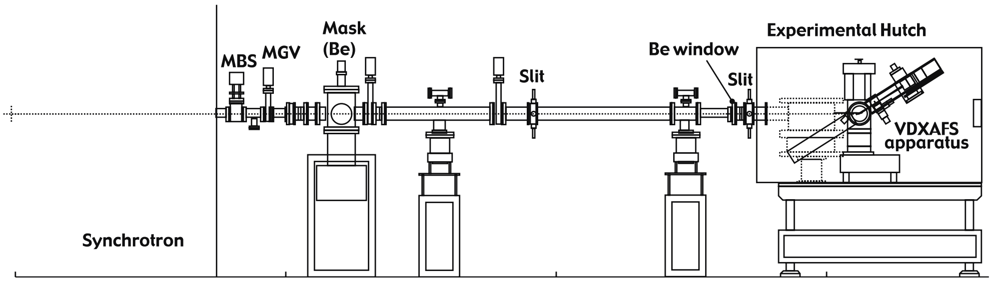

Figure 1 Outline of BL-5.

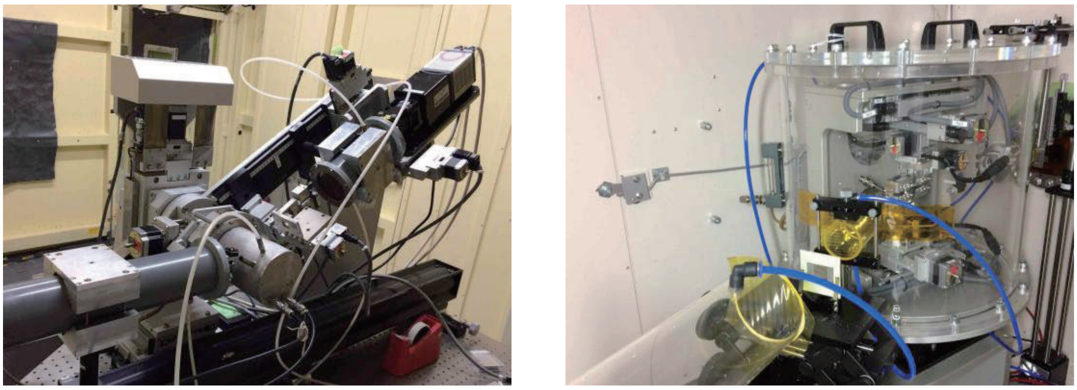

(a) VDXAFS instrument

(b) Double-element DXAFS instrument

Figure 2 DXAFS techniques developed at BL-5.

BL-7

Linearly-Polarized Photoelectron Spectroscopy

VUV, soft X-ray beamline BL-7 is dedicated for solid and surface science. The range of photon energy covered by a monochromator with four spherical gratings is 10-160 eV. A schematic diagram of the beamline is shown in Fig. 1. The first toroidal mirror M0 collimates SR horizontally. A couple of a plane mirror (M1) and a spherical grating G disperses and focuses SR on the exit slit (S2). The optical path employs a 160° deviation angle and use one of four spherical gratings, G2, Gl, G3, and G4 with a radius of curvature of 2000 mm with the groove densities of 300, 600, 1200, and 2400 lines/mm which are designed to cover the energy range 10-20 eV, 20-40 eV, 40-80 eV, and 80-160 eV, respectively. Monochromatic light is focused on the sample position by a toroidal mirror M2. The beam size on the sample is about 1.2 and 0.3 mm in horizontal and vertical, respectively. The calculated photon energy resolution ΔE/E is 500-100 with the photon flux in the order of 10^{10} photons/s/300 mA.

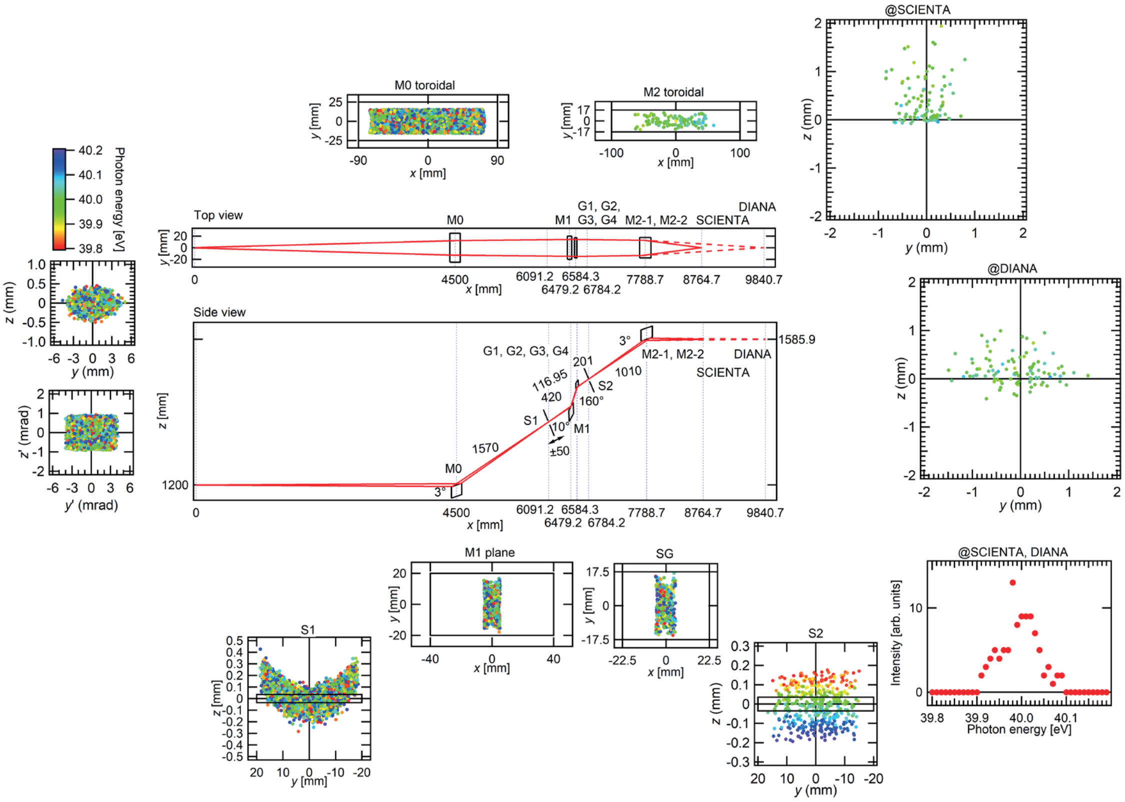

Fig. 1 Optical arrangement of the BL-7. M0, M1, M2: mirrors; S1, S2: entrance and exit slits; G1-4: spherical gratings.

A hemispherical electron energy analyzer (SCIENTA SES2002) and two-dimensional display-type analyzer (DIANA) are tandemly installed at the end station. At the SCIENTA chamber, photoelectron spectroscopy (PES) measurements are conveniently performed to obtain valence-band and core-level spectra. A position-resolved PES, angle-resolved PES, and X-ray PES using Mg and Al Kα sources are also conducted. Utilizing DIANA, two-dimensional PES measurements are performed to obtain a three-dimensional band structure in a wide reciprocal space (±2.3 $Å^{-1}$ at kinetic energy of 36 eV), which contains new information on the motion of valence electrons (velocity, direction and mass). A linearly-polarized SR light enables the analysis of the atomic-orbital composition of each band.

BL−8 (SORIS)

Synchrotron Orbital Radiation-Photoelectron Spectroscopy Combined with Ion Scattering

BL-8 named 'SORIS' consists of mainly two modules, (1) SR-photoelectron spectroscopy (PES) and (2) medium energy ion scattering spectroscopy (MEIS). The former provides the information about the electronic states of surface and interfaces and the latter makes it possible to analyze the atomic configurations. In addition, it is equipped with sample preparation chambers for molecular beam epitaxy (MBE) and for sample heating up to 1200℃ under ultrahigh vacuum (UHV: < 2×10^{-8} Pa) and various gas ambiance (O_2 etc). Accordingly, the analyses are basically performed *in situ*.

The PES system is constructed for studies of solid surfaces by photoelectron spectroscopy, X-ray absorption fine structure, and photochemical reactions in the photon energy from 10 to 700 eV. The first cylindrical mirror M0 made of a Si single crystal focuses SR horizontally. A couple of a plane mirror (M1) and a varied−line-spacing plane grating (VSPG) G disperses and focuses SR on the exit slit (S2). Either 400 l/mm VSPG or 1800 l/mm one can be chosen. Monochromatic light is focused on the sample position by a toroidal mirror M2. The beam size on the sample is about 3 and 1 mm in horizontal and vertical, respectively. The calculated photon energy resolution ΔE/E is 5500 at 10 eV, and 1500 at 700 eV. The photon flux at 100 eV was estimated to be 6×10^{11} photons/s/300 mA. A UHV chamber equipped with a high energy resolution photoelectron spectrometer (Special version of PHI model 10−360 Omni Focus III) is installed at the experimental station.

Table 1 Specification of the PES system

Photon energy	5 – 700 eV
Resolution	E/ΔE = 1500 – 5000
Photon flux	10^{10} - 10^{11} Photons/s/300mA
Beam size	SR: 10.5(H)-3(V) mrad^2 Target: 2(H)-1(V) mm^2
Mirror	M0: cylindrical, Si M1: plane, quartz M2: toroidal, quartz
Grating	Varied-line-spacing plane grating (Hitachi, mechanically ruled, 400 and 1800 l/mm)

The MEIS system is comprised by an ion accelerator (5 – 200 keV), a switching magnet and an ion scattering chamber. A duo-plasma ion source of a hollow cathode type generates dense plasma of H, He and Ne and provides intense ion beams with high emittance. The accelerated ion beam is collimated finally to 0.18 mm^H × 2.0 mm^V and the vertical angular spread is ±0.2°. Scattered ion energy are analyzed by a toroidal electrostatic analyzer with an excellent energy resolution of $\Delta E/E=9\times10^{-4}$. With a wide inter-electrode distance of 16 mm and a radius of central curvature is 150 mm, the analyzer accepts scattered ions in a wide energy range of 10 % of the pass energy at fixed applied voltage, giving high statistics in a short acquisition time.

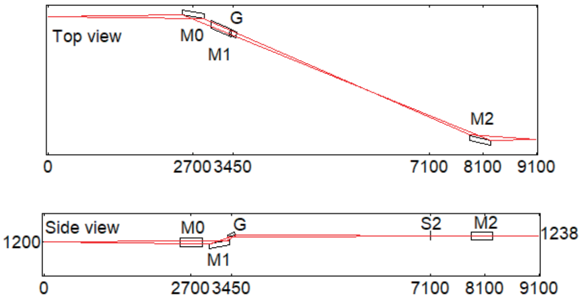

Fig. 1 Optical arrangement of BL-8

Table 2 Specification of the MEIS system

Ion beam	H^+, He^+, Ne^+
Energy	5 – 170 keV
Resolution	E/ΔE = 1000
Beam size	0.18(H)-2.0(V) mm^2
Sample preparation chamber	3 K-cells (Au, Ni, Cu) RHEED
Sample heating	Infrared Radiation under UHV from RT up to 1200℃

BL-10

Tender X-Ray XAFS Beamline

BL-10 is designed for study of X-ray absorption fine structure (XAFS) spectroscopy, using tender X-rays, the most brilliant energy range of the spectrum emitted from the light source, AURORA. It consists of a pre-focusing toroidal mirror, a Golovchenko-type double-crystal monochromator, an I_0 monitor of nickel meshes and a new sample chamber used under high-vacuum (HV) condition. Also, the HV chamber allows us to measure XAFS spectra under atmospheric-pressure (AP) condition by introducing He gas (currently unavailable). The radiation beam with 6 mrad (horizontal) and 2 mrad (vertical) is deflected upward by 1.4 ° and focused at the sample position about 9 m apart from the source point with the 1:1 geometry. The available photon energy covers from about 1000 to 4500 eV (K-edge of Na ~ Ca and L-edge of Zn ~ Sn) by exchanging several monochromatizing crystals. The detection sensitivity limit was improved dramatically by installing a silicon drift detector (SDD, TXD2300H50, Techno X Co.,Ltd.) with the wide detection area of 50 mm^2 (previously, that with detection area of 5 mm^2).

Specification

Photon Energy	about 1000 - 4500 eV
Optical	Be foil (5.1 μm thickness), Ni toroidal mirror (water cooled), Be window (15 μm thickness) Double crystal monochromator: Beryl($10\bar{1}0$), KTP(011), quartz($10\bar{1}0$), InSb(111), Ge(111), Si(111), Ge(220), Si(220).
Beam size	5 mm (horizon)×2 mm (vertical) : focused
Photon flux	about 10^8-10^9 photons/sec
Detecting mode	<HV> TEY mode (sample drain current), PFY mode (SDD) <AP> PFY mode (SDD) (temporarily out of operation)
Other	A transfer vessel system (common to BL-2, 7, 8, 11, 13) for anaerobic or easily-oxidizable samples.

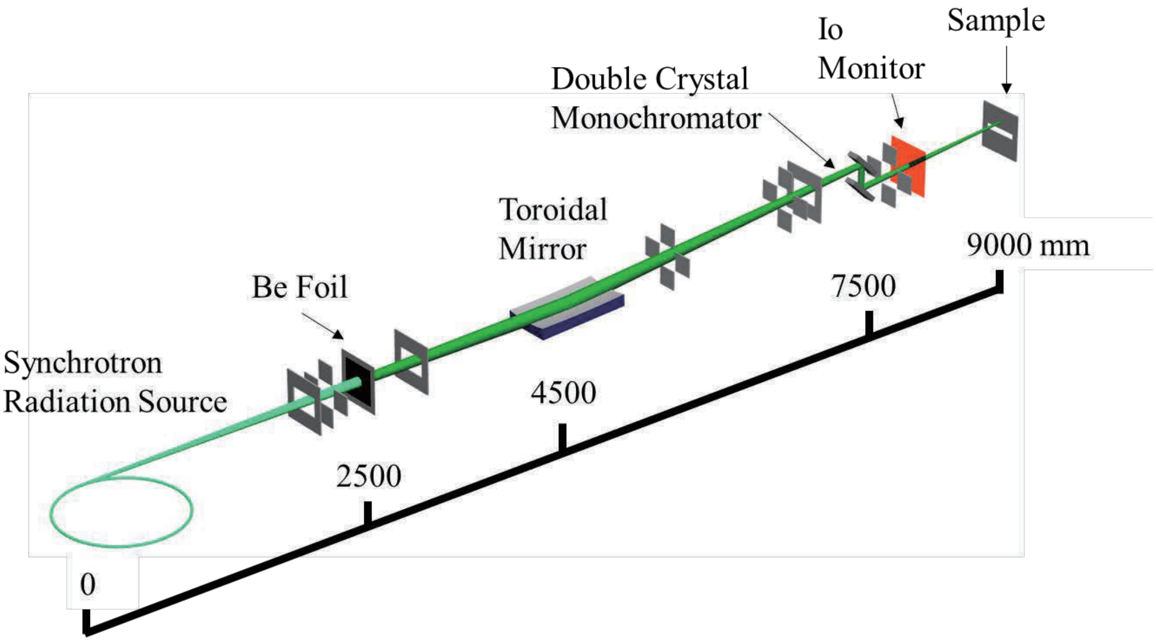

Figure Schematic diagram of BL-10

BL-11

Soft X-ray Absorption Spectroscopy

BL-11 was newly designed and constructed in FY2012, and was open to users in FY2014 for ultra-soft X-ray XAFS experiments. The optical system is basically same as that of BL-2; a set of K-B mirrors, two kinds of spherical mirrors (angle of incidence 87° and 84.5°) selectable depending on the used photon energy range, three kinds of varied-line-spacing plane gratings (300, 600 and 1200 lines/mm) which cover the energy range from 40 to 1,000 eV. The layout of the beamline is shown in the bottom figure. Compared with BL-2, several improvements were added in the design stage. (1) Each grating has a grooved length of 200 mm, double of that in BL-2. BL-11 provides us roughly double photons with two times higher energy resolution than BL-2. (2) Beam size at the sample position is less than 1 mm^2. The same transfer vessel is available as that in BL-2, 10 and 13. Three kinds of detection modes (TEY, PEY and PFY) can be used simultaneously. Very efficient differential pumping system has been also installed at the upstream of the sample chamber for the XAFS experiments under low vacuum conditions.

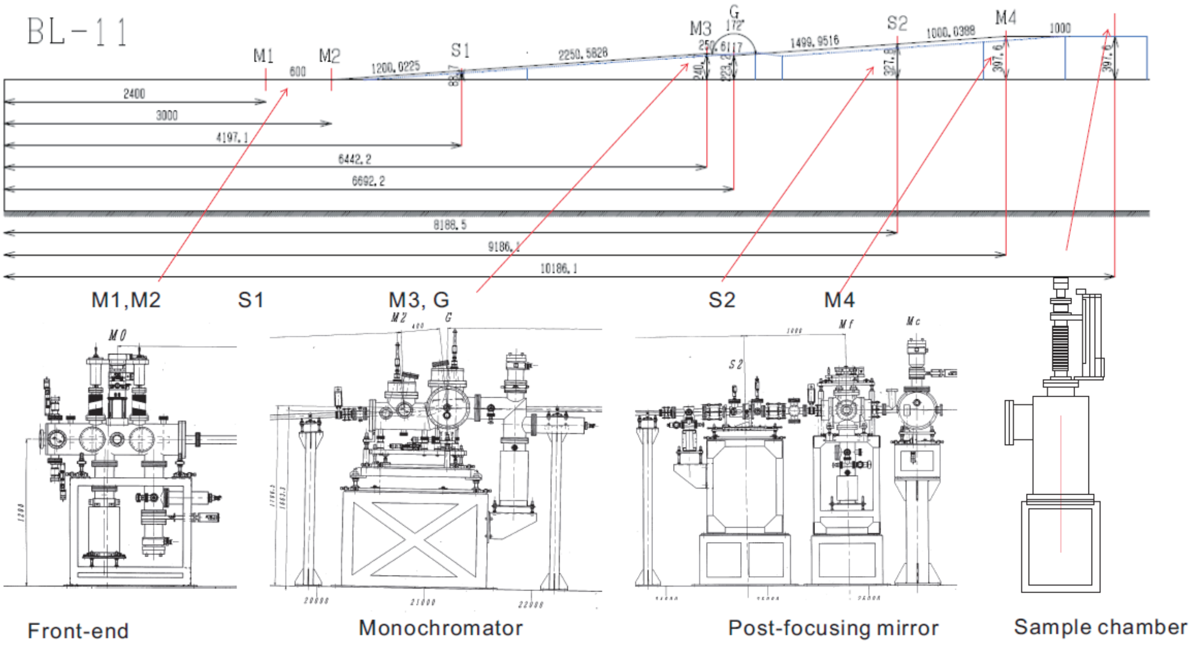

Beamline layout of BL-11

BL-12

Soft X-ray Microscopy

This beamline has been operating since 1995. Advantages of this X-ray microscope station are as follows: (1) a dry or wet specimen is located under atmospheric pressure, (2) for object finding and pre-focusing, a light microscope can be used, (3) multi-wavelength imaging enables, and (4) 3-dimensional observation by nano computed tomography (CT) method. After 2010, a cryogenic CT system was constructed.

This beamline consists of a wedge shaped slit, SiC, SiO_2 plane mirror, and an optical stage. The optical stage is composed of a condenser zone plate (ZP), a pinhole (20 μmϕ), a specimen stage, an objective ZP, and a cooled CCD camera. The two plane mirrors were switched by x-ray wavelength. The SiO_2 is used to reduce higher order diffraction below 2.28 nm. Images are focused with the first-order diffraction. Groove efficiency and absolute efficiency of the condenser ZP are 7.5 % and 3.6 % at 2.5 nm respectively. The spatial resolution is estimated to be below 65 nm (20-80%) from the intensity gradient of its knife-edge profile at 2.0 nm.

For 2-dimensional observation, almost any kind of holder can be mounted in the sample stage, for example, micro grids with carbon substrate, polyimide films, and silicon nitride membranes. For wet samples, a wet cell is prepared. It consists of two thin polyimide films (below 300 nm in thickness) supported by thick ones. Wet samples are placed between the two thin polyimide films and the wet cell is sealed with silicon grease. For 3-dimensional observation, a sealed glass capillary tube was used. Sample was inserted to the capillary tube and observed with CT method. Imaging time is typically 20 – 300 sec.

Specification
Energy range: 280 - 710 eV (wavelength: 4.40 nm - 1.75 nm)
Optical element: wedge shaped slit, SiC and SiO_2 plane mirror,
condenser ZP, objective ZP
Detector: cooled CCD camera
(C4880-21-24WD: Hamamatsu Photonics)
512 pixel × 512 pixel, 24 μm × 24 μm each
Spatial resolution: 65 nm (20~80%) at λ=2.0 nm
Energy resolution: $E/\Delta E = 200$
Scientific applications: Biology, Medical, Polymers, Material sciences,
Environmental sciences, Powder

Table 1: Specification of the condenser and objective zone plate

	condenser ZP	objective ZP 1	objective ZP 2
Diameter (μm)	9,000	84	108
Number of the zones	41,890	311	311
Outermost zone width (nm)	53.7	36	54
Zone material (thickness:μm)	Ge (0.3)	Ta (0.16)	Ta (0.16)
Support material (thickness: μm)	SiN (0.1)	SiN (0.15)	SiN (0.15)

BL-13

Tender X-ray Absorption Spectroscopy

BL-13 is a beamline for soft X-ray Absorption Fine Structure (XAFS) measurements. The layout of the beamline is shown in Fig.1. A water cooled 4 quadrant slits and a Be filter is located at 2.4 m from the source point. The first Ni coated Si toroidal mirror, whose effective size is 500 mm^{L} x 40 mm^{W}, is located at 3 m and deflects the SR beam downward by 1.2°. This mirror can accept SR beam of as large as 10 mrad^{H} x 2.5 mm^{V}. The deflected beam shape and intensity is monitored at 3.5 m from the source point. The quasi-parallel beam is introduced to Golovchenko-type double crystal monochromator (TOYAMA Co. Ltd.). We employed Beryl$(10\bar{1}0)$, KTP(011), InSb(111), Ge(111), Si(111) and Si(220) as monochromatizing crystal pairs in order to cover the wide energy range. The monochromatized beam is deflected upward by 1.2° and focused by the second Ni coated SiO_2 toroidal mirrors, whose effective size is just same as the first one. The monochromatized beam is monitored at 5.8 m and focused at the sample position apart by 6.5 m from the source point. The XAFS spectra can be obtained in two different modes simultaneously; the partial fluorescence yield (PFY) mode with a silicon drift detector and the total electron yield (TEY) mode (sample drain current mode). A transfer vessel system compatible with BL-2, BL-7, BL-8, BL-10 and BL-11 is also installed.

Fig.2 (a) shows beam profiles simulated by SHADOW. The set of the quasi-parabolic mirrors gives almost same beam width as that of parabolic mirrors. Fig.2 (b) shows the intensity distribution in horizontal direction of a beam at the sample position. Here, we obtained this spectrum by scanning ϕ 0.1 mm Au wire at the incident X-ray energy of 2000 eV. We used a Gauss function to fit this spectrum and estimated $2\sigma = 1.20$ mm. This value is almost same as the simulated one. Above results indicate that this optical system gives a small beam size at the sample position.

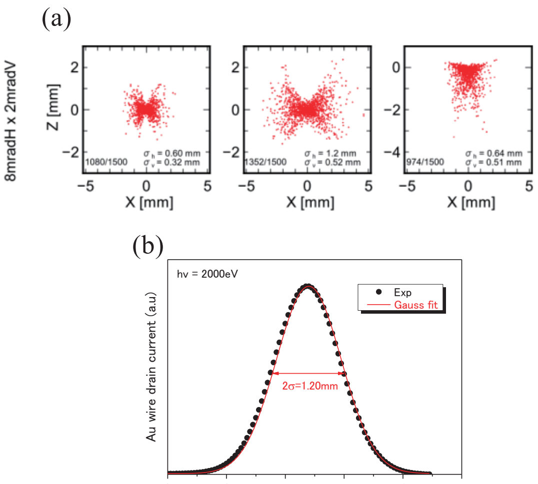

Fig.2 (a)Simulated X-ray beam profiles at the focal point for parabolic mirror, 1:1 toroidal mirror and quasi-parabolic toroidal mirror from left to right. The SR beam divergence is 8mrad^{H} x 2mrad^{V}. (b) The intensity distribution in horizontal direction of a beam at the sample position. Red curve (thick) indicates the best-fitted spectrum.

< Specification >

Photon energy	1000 – 5500 eV
Beam size	2.5(H) × 1.5(V) mm^2
Mirror	Pre-mirror: Ni coated Si toroidal mirror Post-mirror: Ni coated SiO_2 toroidal mirror
Monochromator	Golovchenko-type
Detection mode	TEY mode (sample drain current) PFY mode (SSD)

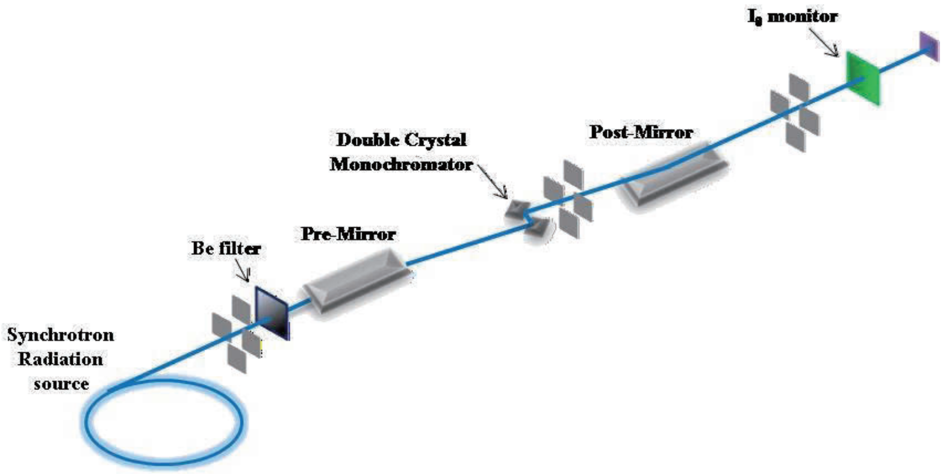

Fig.1 The layout of the soft X-ray double crystal beamline

BL-15

Infrared Microspectroscopy

Infrared microspectroscope (IRMS) with an SR light source is designed for infrared (IR) spectroscopic studies of a microscopic region in various materials since SR light is a higher brilliance than laboratory sources in commercial IRMS. IR photons are collected by a toroidal mirror installed in the ring chamber, whose acceptance angles are 250 mrad (horizontal) and 63 mrad (vertical). The beam is once focused inside a ring port to travel through the narrow port. Another toroidal mirror outside the chamber focuses the beam again in the air part of the beamline via a window (NIR-MIR: BaF_2 or KRS-5, FIR: Diamond). The diverging beam is shaped into a parallel beam with a parabolic mirror, and then introduced into a commercial IRMS equipment. As a result, our IRMS with the SR light (SRMS) has a spatial resolution of ca. 5μm though that of a commercial IRMS is 10μm. And the SRMS has five times intensity than that of the commercial IRMS equipped with the end of this beamline in the MIR region.

BL-15 is currently out of operation due to failure of FTIR.

○Specifications

FTIR Spectrometer: Nicolet 6700 (Thermo Fisher Scientific Inc.)

Beam splitter: XT-KBr (11000 - 350 cm^{-1}) for NIR to MIR, Solid (700 - 20 cm^{-1}) for FIR.

Energy Resolution (typ.): 4 cm^{-1}.

Detector: DLaTGS/KBr (7800 cm^{-1} - 350 cm^{-1}), DLaTGS/PE (700 cm^{-1} - 50 cm^{-1}).

FTIR Microscope: Nicolet Continuμm XL (Thermo Fisher Scientific Inc.)

Optics: 15x (N.A. 0.58), 32x (N.A. 0.65) Cassegrain objectives and condensers.

Detector: 50μmMCT (11000 - 650 cm^{-1}), 1D-arrayed MCT (11000 - 800 cm^{-1}).

Accessories: Semi-spehere Ge ATR unit.

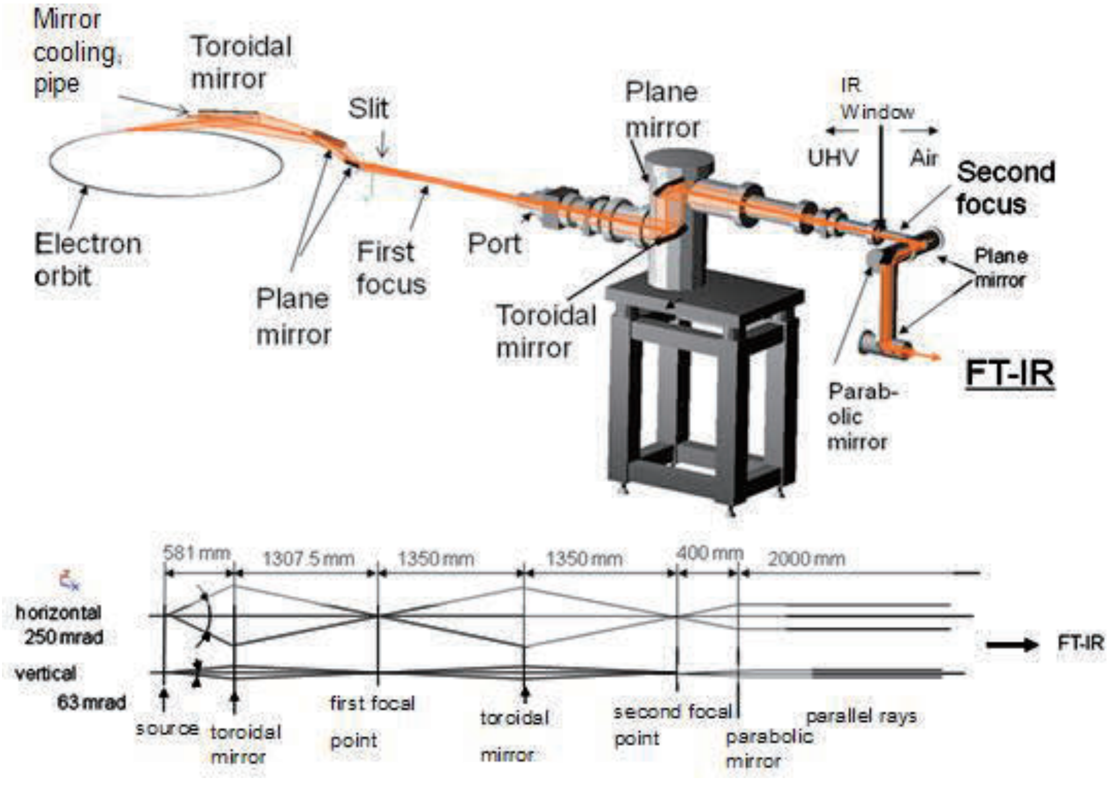

Fig. Schemtic diagrams of the BL-15 and the optical system. IR window is BaF_2 (NIR to MIR) or Diamond (FIR).

SA-1

Scanning Soft and Hard X-Ray Photoemission (SX&HX-ESCA)

Standalone station 1 (SA-1) is an apparatus for scanning soft and hard x-ray photoemission spectroscopy, which is basically a commercial equipment, ULVAC-PHI Quantes. Both soft x-ray photoemission (SXPES) by Al Kα emission (1486.6 eV) and hard x-ray photoemission (HAXPES) by Cr Kα emission (5414.7 eV) can be performed on the same sample. Samples can be introduced through the introduction chamber under air or through the transfer chamber under vacuum or Ar atmosphere. A sample can be fractured by pushing a post glued on the sample with the wobble stick in the preparation chamber. The best energy resolution is such that the width (FWHM) of the Ag $3d_{5/2}$ peak is 0.49 (0.87) eV with SXPES (HAXPES). Both soft x-ray and hard x-ray sources are monochromatized and focused. Typical x-ray settings (spot size, power, high voltage) are (100μm, 25W, 15kV), (50μm, 12.5W, 15kV), (20μm, 4.5W, 15kV), (15μm, 2.5W, 15kV), and (7.5μm, 0.8W, 15kV) for Al Kα source and (100μm, 50W, 20kV), (20μm, 10W, 20kV), and (7.5μm, 0.8W, 15kV) for Cr Kα source. For insulating samples, charge neutralization using low-energy electron beam and/or Ar ion beam can be applied. For sample cleaning and depth profiling, Ar ion sputtering with typical ion current of 30 nA and typical acceleration voltages of 0.5, 1, 2, 3, or 4 kV can be applied to 2×2 or 3×3 mm^2 area. One can perform automatic measurements of several days by making a queue of measurements.

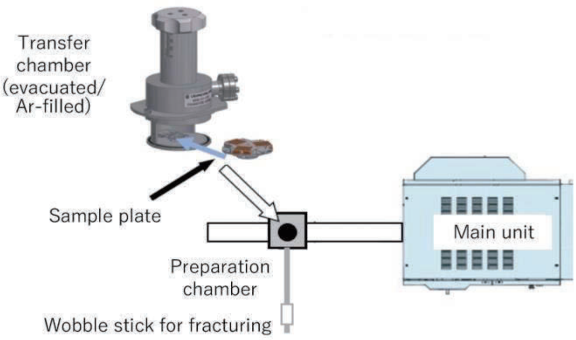

Fig.1 Schematic view of the scanning soft and hard x-ray photoemission apparatus. Using the transfer chamber, up to three SR-type holders can be installed under vacuum or Ar atmosphere.

LIST OF PUBLICATIONS
AWARDS
ACADEMIC DEGREES

LIST OF PUBLICATIONS

General

Papers

[1] K. Asakura: *Operando* X-ray absorption fine structure spectroscopy and its applications to catalysts, Bull. Chem. Soc. Jpn., **99** (2026) uoag043.

Books

[1] 太田俊明: 放射光分析, 日本分析化学会, 共立出版 (2025).

Domestic Meeting

[1] 入澤明典: 立命館大学 SR センターの現状(施設報告), 第 38 回日本放射光学会合同シンポジウム, 仙台, 1 月 (2026).

BL-2, 11

Papers

[1] S. Taniguchi, A. Yamada, T. Ohuchi, K. Ohara, D. Shibata, M. Nishiwaki, J. Matsuoka: Synthesis and structure of anisotropic borosilicate glasses under differential stress at high pressure and temperature, J. Am. Ceram. Soc., **108** (2025) e70040.

[2] D. Shibata, R. Yamamoto, M. Matsumoto, H. Murayama, C. Zhong, K. Shimoda, K. Okazaki, S. Yamashita, Y. Orikasa: Analysis of Degradation Mechanisms in $LiNi_{0.8}Mn_{0.1}Co_{0.1}O_2$ Lithium-ion Battery Cathodes During High-Rate Charge–Discharge Cycling, Electrochemistry, **93** (2025) 063016.

[3] M. Suzuki, I. Hasegawa, T. Watanabe: Characterization of surface ionic arrangements of borate melts induced by structural relaxation, J. Am. Ceram. Soc., **108** (2025) e70068.

[4] M. Harada, A. Saito, H. Nakahira, Y. Mori, S. Kawaguchi: In Situ Observations of Catalytically Active Sites of Cobalt–Manganese Spinel Oxides as Efficient Bifunctional Electrocatalysts for Oxygen Evolution and Reduction Reactions, ACS Appl. Energy Mater., **8** (2025) 13390–13406.

[5] A. Abdel Haleem, H. Enjoji, K. Gu, T. Miwa, Y. Kuroda, Y. Orikasa, T. Uchiyama, Y. Uchimoto, S. Mitsushima: Accelerated Durability Assessment and a Proposed Degradation Mechanism of $NiCoO_x$ OER Catalysts under Simulated Intermittent Renewable Power: Insights from XAS, ACS Appl. Mater. Interfaces, **12** (2025) 61929–61940.

[6] E. Choi, S. Lim, H. Oh, Y. Orikasa, T. Ohta, K. Yim, H.R. Byon: Ultrafast Charging Enabled by Soft Ion Channels on Layered Transition Oxide Cathodes in Aqueous Li-Ion Batteries, Adv. Energy Mater., **16** (2026) e05594.

[7] L. Zhao, Q. Yuan, W. Ren, T. Asada, C. Wu, T. Itoh, S. Ogiu, T. Sanada, S. Yamashita, D. Shibata, Y. Yao: Chemical Imaging of Cathode–Electrolyte Interphase in Sulfide Solid-State Batteries, ACS Energy Lett., **11** (2026) 2668–2676.

Domestic Meeting

[1] 大久保俊祐, 柴田大輔, 鐘承超, 下田景士, 岡崎健一, 折笠有基: ランタンニッケル系ペロブスカイト酸化物の表面電子構造と OER 活性の解析, 第 34 回電極材料研究会, 8 月 (2025).

[2] 入澤明典, 柴田大輔, 今田真, 朝倉清高, 木村真優, 吉岡大祐, 小林洋一: Cu-ZnS の光誘起価数転移, 第 28 回 XAFS 討論会, つくば, 9 月 (2025).

[3] 永井崇之, 岡本吉弘, 柴田大輔, 朝倉清高, 長谷川武彦, 佐藤誠一: 軟 X 線領域 XAFS 測定による模擬廃棄物ガラス評価, 日本原子力学会 2025 年秋の大会, 北九州, 9 月 (2025).

[4] 柴田大輔, 朝倉清高: F K 吸収端位置はどうやって決まるか？, 第 28 回 XAFS 討論会, つくば, 9 月 (2025).

[5] 柴田大輔, 太田俊明, 朝倉清高: 蛍光 X 線収量法による軟 X 線 XAFS スペクトルにおける自己吸収効果の考察 3, 第 28 回 XAFS 討論会, つくば, 9 月 (2025).

[6] 家路豊成, 柴田大輔, 朝倉清高: フッ化物の XANES スペクトルの第一原理計算, 第 28 回 XAFS 討論会, つくば, 9 月 (2025).

[7] 濵田丈翔, 後藤佑太朗, 柴田大輔, 入澤明典, 鐘承超, 下田景士, 岡崎健一, 折笠有基: 高濃度 LiFSI 電解液によるグラファイト負極の高温耐久化機構の解析, 2025 電気化学秋季大会, 9 月 (2025).

[8] 宮浦優希, 下田景士, 鐘承超, 岡崎健一, 折笠有基: 酸化物固体電解質—液体電解質界面抵抗のメカニズム解析, 2025 電気化学秋季大会, 9 月 (2025).

[9] Y. Abiko, K. Kaminaga, A. Kikuchi, S. Maruyama, Y. Matsumoto, H. Murakami, D. Nanasawa, K. Sasaki, H. Setoyama, D. Shibata, K. Suzuki, K. Tanaka, F. Teshima, T. Tobe, S. Yasui: Functionally-Graded Site Engineering, 第 35 回日本 MRS 年次大会, 北九州, 11 月 (2025).

[10] 伊藤仁彦, 大塚裕美, 野村晃敬, 柴田大輔, 朝倉清高: Li-O_2 二次電池におけるレドックスメディエーター機能阻害要因解析, 第 66 回電池討論会, 名古屋, 11 月 (2025).

[11] 大久保俊祐, 柴田大輔, 鐘承超, 下田景士, 岡崎健一, 折笠有基: ランタンニッケル系ペロブスカイト酸化物の酸素発生反応活性解析, 第 49 回電解技術討論会, 11 月 (2025).

[12] 濵田丈翔, 後藤佑太朗, 柴田大輔, 入澤明典, 鐘承超, 下田景士, 岡崎健一, 折笠有基: 高濃度 LiFSI 電解液によるグラファイト負極の高温劣化抑制機構の解析, 第 66 回電池討論会, 11 月 (2025).

[13] 濵田丈翔, 後藤佑太朗, 柴田大輔, 入澤明典, 鐘承超, 下田景士, 岡崎健一, 折笠有基: 高濃度 LiFSI 電解液を用いたグラファイト負極の高温安定性に及ぼす影響とその機構解析, 2025 第 3 回 関西電気化学研究会, 12 月 (2025).

[14] 大久保俊祐, 柴田大輔, 鍾承超, 下田景士, 岡崎健一, 折笠 有基: Ruddlesden-Popper 相ランタンニッケル酸化物の酸素発生反応, 第 45 回水素エネルギー協会, 12 月 (2025).

[15] 入澤明典, 柴田大輔, 今田真, 朝倉清高, 木村真優, 吉岡大祐, 小林洋一: Cu-ZnS NCs の光誘起価数転移, 第 38 回日本放射光学会・放射光科学合同シンポジウム(JSR2025), 仙台, 1 月 (2026).

[16] 朝倉清高, 柴田大輔, フッ素 K 吸収端エネルギーの決定要因: 第 38 回日本放射光学会合同シンポジウム, 仙台, 1 月 (2026).

[17] 山田明寛, 倉田真路, 左近光, 朝見遼太, 柴田大輔, 入澤明典, 西脇瑞紀, 松岡純: 高密度ホウケイ酸塩ガラスの構造変化, 日本セラミックス協会 2026 年年会, 横浜国立大学 3 月 (2026).

[18] 濵田丈翔, 後藤佑太朗, 柴田大輔, 入澤明典, 鐘承超, 下田景士, 岡崎健一, 折笠有基: 高濃度電解液を用いたグラファイト負極の高温耐久化特性と反応メカニズム解析, 電気化学会第 93 回大会, 3 月 (2026).

International Meeting

[1] Yuki Orikasa, Takeru Hamada, Yuta Shiomi, Yutaro Goto, Rinka Yamamoto, Chengchao Zhong, Keiji Shimoda, Ken-ichi Okazaki: Soft X-ray Absorption Spectroscopy Study on Electrode-Electrolyte Interphase of Lithium-ion Battery Electrodes, Pacifichem 2025, December (2025).

[2] Shunsuke Okubo, Daisuke Shibata, Chengchao Zhong, Keiji Shimoda, Ken-ichi Okazaki and Yuki Orikasa: Oxygen Evolution Reaction Activity and Structure Analysis of Lanthanum-Nickel Oxide for Alkaline Water Electrolysis, ICGHET 2026, January (2026).

[3] Yuta Shiomi, Keiji Shimoda, Chengchao Zhong, Ken-ichi Okazaki, Keitaro Sodeyama, Hiroki Oka, Yuki Yamada and Yuki Orikasa: Analysis of the High-Temperature Charge–Discharge Durability Mechanism of NCM Cathodes using Phosphate Ester Electrolytes, ICGHET 2026, January (2026).

BL-3, 4, 5

Papers

[1] E. Novitasari, A. Azuma, K. Ohta, M. Katayama, Y. Niwa, M. Kimura, Y. Inada: Chemical state analysis of size-controlled particles during redox reactions between NiO and metallic Ni, Next Mater., **8** (2025) 100738.

[2] I. Ban, S. Higashidani, H. Watanabe, T. Ogura, Y. Inada: Operando X-ray Diffraction Analysis and DFT Calculations of Ni Cathode Oxidation during Electrochemical CO_2 Reduction, J. Electrochem. Soc., **172** (2025) 054505.

[3] M. Ishii, A. Matsuda, K. Sakamoto, S. Yamashita, Y. Niwa, Y. Inada: Global cross-database search system for X-ray absorption spectra, J. Synchrotron Rad., **32** (2025) 661-668.

[4] K. Obuchi, J. Kitamura, M. Ando, K. Kamo, K. Nakamura, E. Mukayabu, T. Utsunomiya, Y. Kondo, Y. Sasaki, K. Yoshida, Y. Yamada, A. Irizawa, A. Kuwabara, W. Yoshida, K. Asakura, Y. Katayama, M. Nakayama: An Fe^{3+}-Responsive MnO_2/Mn^{2+} Cathode for Zinc-Ion Batteries: Fe^{3+} Incorporated into MnO_2 during Charging Accelerates its Dissolution during Discharging, ACS Appl. Energy Mater., **8** (2025) 15112–15123.

Domestic Meeting

[1] 東亜紗花, 深田恵子, 朝倉清高, 稲田康宏: シリカ担持酸化マンガンの昇温脱酸素過程の in situ XAFS 解析, 第 28 回 XAFS 討論会, つくば, 9 月 (2025).

[2] 横谷寧々, 鵜飼隼也人, 丹羽尉博, 木村正雄, 稲田康宏: 部分還元した形状制御 Cu_2O 粒子の二次元顕微イメージング XAFS 解析, 第 28 回 XAFS 討論会, つくば, 9 月 (2025).

[3] 深田恵子, 東亜紗花, 稲田康宏: 炭素担持酸化マンガンの電気化学コンバージョン過程における状態解析, 第 28 回 XAFS 討論会, つくば, 9 月 (2025).

[4] 浦野瑶子, 鵜飼隼也人, 横谷寧々, 稲田康宏: In Situ 転換電子収量 XAFS 法による Cu_2O 粒子表層の還元特性解析, 第 28 回 XAFS 討論会, つくば, 9 月 (2025).

[5] 八馬完樹, 稲田康宏: 炭素担持 ZnO 電極の電気化学的コンバージョン過程に関する XAFS 解析, 第 28 回 XAFS 討論会, つくば, 9 月 (2025).

[6] 稲田康宏, 柴田壮士郎, 高野雅也, 城戸大貴, 木村正雄, 池澤篤憲, 荒井創: Persistent Homology を用いた亜鉛電極面内の反応分布解析と添加剤の影響の検討, 第 28 回 XAFS 討論会, つくば, 9 月 (2025).

[7] 柴田壮士郎, 高野雅也, 城戸大貴, 木村正雄, 池澤篤憲, 荒井創, 稲田康宏: 亜鉛電極面内の反応分布に対する Persistent Homology 解析の有効性の検討, 第 15 回 CSJ 化学フェスタ 2025, 船堀, 10 月 (2025).

[8] 樋口歩未, 柴田壮士郎, 花野翔, 東亜紗花, 太田昂大, 稲田康宏: シリカ担持酸化バナジウムの昇温酸化還元過程における化学状態解析, 第 15 回 CSJ 化学フェスタ 2025, 船堀, 10 月 (2025).

[9] 花野翔, 樋口歩未, 東亜紗花, 太田昂大, 鈴木捷斗, 稲田康宏: シリカ担持クロム触媒の焼成過程の化学状態解析, 第 15 回 CSJ 化学フェスタ 2025, 船堀, 10 月 (2025).

[10] 山崎慶太, 野崎文康, 黄珍光, 松本和彦: トリフィライト型 $NaFePO_4$ の Mn 置換による充放電特性への影響 第 66 回電池討論会(名古屋), 11 月 (2025).

[11] E. Novitasari, K. Ohta, A. Azuma, H. Ukai, Y. Inada: Chemical state analysis of silica-supported Ni catalysts during partial oxidation by in situ XAFS technique, 第 39 回日本放射光学会年会・放射光科学合同シンポジウム, 仙台, 1 月 (2026).

[12] 鵜飼隼也人, 横谷寧々, 丹羽尉博, 木村正雄, 稲田康宏: 顕微 XAFS を用いた八面体型酸化銅(I)粒子の還元挙動解析, 第 39 回日本放射光学会年会・放射光科学合同シンポジウム, 仙台, 1 月 (2026).

[13] 柴田壮士郎, 高野雅也, 城戸大貴, 木村正雄, 池澤篤憲, 荒井創, 稲田康宏: Persistent Homology による亜鉛電極反応分布と添加剤影響の解析, 第 39 回日本放射光学会年会・放射光科学合同シンポジウム, 仙台, 1 月 (2026).

[14] 川口綾香, 稲田康宏: In situ 二次元イメージング XAFS による炭素担持 NiO 電極の反応分布解析, 第 39 回日本放射光学会年会・放射光科学合同シンポジウム, 仙台, 1 月 (2026).

[15] 野崎文康, 山崎慶太, 稲田康宏, 折笠有基, 黄珍光, 松本和彦: トリフィライト型 $NaMn_xFe_{1-x}PO_4$ の充放電特性, 電気化学会第 93 回大会, 野田, 3 月 (2026).

BL-7

Papers

[1] T. Fujii, D. Hakozaki, A. Tsuji, M. Takizawa, J. Murata: Maskless soft lithography for fabricating micro- and nanoscale Ag structures via solid-state electrochemical etching using a polymer electrolyte membrane for optoelectronic and sensing applications, Materials Advances, **6** (2025) 5424-5438.

[2] S. Hayakawa, M. Takizawa, D. Hakozaki, J. Murata: Liquid-free electrochemical approach for direct patterning of ITO films with polymer electrolyte stamps for flexible transparent electrodes, Applied Surface Science, **716** (2026) 164674-1-12.

[3] A. Ochi, K. Shibamoto, Y. Toyotake, D. Fujioka, F. Yokoyama, H. Okanishi, T. Imai, D. Fujita, R. Aono, M. Inoue, M. Takizawa, R. Tobe, Y. Kanai, T. Imai, H. Mihara: Biosynthesis and export of membrane-enveloped selenium nanoparticles by *Escherichia coli*, Environmental Science and Technology, **60** (2026) 4213-4227.

International Meeting

[1] Tatsuya Fujii, Daishi Hakozaki, Atsuki Tsuji, Masaru Takizawa, Junji Murata: Maskless soft lithography for fabricating micro- and nanoscale Ag structures via solid-state electrochemical etching using a polymer electrolyte membrane, 40th ASPE Annual Meeting, P-2-4, California, USA, November (2025).

BL-8

Papers

[1] S. Entani, M. Honda, M. Takizawa, M. Kohda: Single-layer graphene oxide film grown on α-Al_2O_3(0001) for use as an adsorbent, Beilstein Journal of Nanotechnology, **16** (2025) 1082-1087.

Domestic Meeting

[1] 圓谷志郎, 滝沢優, 好田誠: 高エネルギーイオン照射法による窒化炭化ホウ素の作製, 2025 年 第 86 回応用物理学会秋季学術講演会, 名古屋, 9 月 (2025).

[2] 藤木柾成, 前島尚行, 滝沢優: $SrTiO_3$(100)上のペンタセン薄膜の分子配向角度の膜厚依存性, 2025 年 第 86 回応用物理学会秋季学術講演会, 名古屋, 9 月 (2025).

[3] 堀凜太郎, 長谷川友里, 前島尚行, 滝沢優: 還元された Rutile TiO_2(110)上の Pentacene 薄膜の分子配向分析, 2025 年 第 86 回応用物理学会秋季学術講演会, 名古屋, 9 月 (2025).

[4] 荒木一慶, 前島尚行, 滝沢優: 紫外線照射による多層カーボンナノチューブの欠陥形成, 2025 年 第 86 回応用物理学会秋季学術講演会, 名古屋, 9 月 (2025).

[5] 有本太郎: NEXAFS による VUV 処理ポリマー材料表面の分析, 第 28 回 XAFS 討論会, つくば, 9 月 (2025).

[6] Yuri Hasegawa, Rintaro Hori, Naoyuki Maejima, Masaru Takizawa: Electronic state and adsorption geometry of pentacene on reduced rutile-TiO_2(110), JVSS2025, 2P09, Tsukuba, Nov. (2025).

BL-10, 13

Papers

[1] T. Fujii, D. Hakozaki, A. Tsuji, M. Takizawa, J. Murata: Maskless soft lithography for fabricating micro- and nanoscale Ag structures via solid-state electrochemical etching using a polymer electrolyte membrane for optoelectronic and sensing applications, Materials Advances, **6** (2025) 5424-5438.

[2] S. Zhang, J. Hwang, K. Murakami, C. Zhong, T. Yaji, Y. Orikasa, K. Matsumoto: Overlooked issues on oxidation state analysis in electrode materials by X-ray photoelectron spectroscopy, J. Power Sources, **644** (2025) 237093.

[3] M. Shinoda, K. Matsunoshita, M. Nakayama, S. Hiroi, K. Ohara, M. Abe, N. Ishiguro, Y. Takahashi, G. Hasegawa, N. Kuwata, T. Iwama, T. Masuda, K. Suzuki, H. Ishii, Y.-C. Shao, D. Shibata, A. Irizawa, T. Ohta, I. Konuma, T. Ohno, Y. Ugata, N. Yabuuchi: Activation of Anionic Redox for Stoichiometric and Li-Excess Metal Sulfides through Structural Disordering: Joint Experimental and Theoretical Study, J. Am. Chem. Soc., **147** (2025) 26238–26253.

[4] N. Wada, K. Akiyama, Y. Yamashita, T. Yaji, K. Kojima, T. Asahi: Glass compositional dependence of In+-center concentration and fluorescence spectral properties in In^{3+}-doped and Mn^{2+}-co-doped phosphate glasses, Optical Materials, **165** (2025) 117165.

[5] S. Kashiwakura, A. Okamoto, S. Kosai, M. Takizawa, E. Yamasue: A Promising Silicothermic Route for Low-Temperature, Byproduct-Free Production of White Phosphorus Using Silicon Waste, ACS Sustainable Chemistry & Engineering, **13** (2025) 21537–2154.

[6] S. Hayakawa, M. Takizawa, D. Hakozaki, J. Murata: Liquid-free electrochemical approach for direct patterning of ITO films with polymer electrolyte stamps for flexible transparent electrodes, Applied Surface Science, **716** (2026) 164674.

[7] T. Takeuchi, Y. Hinuma, K. Ohara, H. Kageyama, K. Nakanishi, T. Ohta, S. Fujinami, H. Kiuchi, H. Sakaebe: Analysis of the charge/discharge mechanism of an Fe-containing Li_2S positive electrode material and its visualization by computational simulation, Dalton Trans., **55** (2026) 4128-4138.

[8] A. Ochi, K. Shibamoto, Y. Toyotake, D. Fujioka, F. Yokoyama, H. Okanishi, T. Imai, D. Fujita, R. Aono, M. Inoue, M. Takizawa, R. Tobe, Y. Kanai, T. Imai, H. Mihara: Biosynthesis and Export of Membrane-Enveloped Selenium Nanoparticles by *Escherichia coli*, Environ. Sci. Technol., **60** (2026) 4213–4227.

[9] K. Osada, A. Yamada, K. Ohara, S. Yoshida, J. Matsuoka: Deformability of Mg-aluminosilicate glass under high pressure and shear stress: dynamic coordination change of Al^{3+}, Phys. Chem. Chem. Phys., **28** (2026) 10474-10485.

[10] S. Matsumoto, K. Ohbayashi, T. Yaji, S. Kudo, J.-I. Hayashi, Y. Orikasa, A. Kitajou: Electrochemical Characteristics of SiO_2/C Prepared from Rice Husk and Its Model Materials as Anodes for Lithium-Ion Batteries, Electrochemistry, Accepted.

[11] Y. Ijichi, K. Sakata, T. Kashiwabara, Y. Takahashi, T. Ohno: Mg K-edge XAFS analysis of biogenic aragonite, Chemistry Letters, Accepted.

International Meeting

[1] Mao Matsumoto, Chengchao Zhong, Keiji Shimoda, Ken-ichi Okazaki, Yuki Orikasa: X-Ray CT Analysis of Mechanical Interface between Silicon Particle and Solid Electrolyte during Charge-Discharge, 247th ECSMeeting, Motreal, May (2025).

[2] Anna Ochi: Characterization of membrane-encapsulated selenium nanoparticles and their membrane-dependent export by *Escherichia coli*, 13th International Symposium on Selenium in Biology and Medicine (ISSBM 13), Daejeon, October (2025).

[3] Mao Matsumoto, Arata Matsumoto, Nodoka Ishikawa, Kei Hirabayashi, Yuya Sakka, Yuki Orikasa: Analysis of Silicon-Anode Degradation Mechanisms in All-solid-state Batteries via X-ray Nano-CT, ACEPS-13 (Invited lecture), Bengaluru, January (2026).

Domestic Meeting

[1] 家路豊成, 柴田大輔, 朝倉清高: フッ化物の XANES スペクトルの第一原理計算, 第 28 回 XAFS 討論会, つくば, 9 月 (2025).

[2] 折笠有基, 平林慶, 松本新大, 松本真緒, 作花勇也: 放射光 X 線解析による次世代蓄電池の充放電機構解明, 日本セラミックス協会 第 38 回秋季シンポジウム (依頼講演), 前橋, 9 月 (2025).

[3] 石川和花, 家路豊成, 鐘承超, 下田景士, 岡崎健一, 折笠有基: 全固体電池におけるマイクロシリコン負極の粒径依存性解析, 第 15 回 CSJ 化学フェスタ 2025, 東京, 10 月 (2025).

[4] 塩見優太, 下田景士, 鐘承超, 岡崎健一, 袖山慶太郎, 岡弘樹, 山田裕貴, 折笠有基: リン酸エステル溶媒による NCM 正極の高温充放電安定性に及ぼす影響とその機構解析, 2025 年度 第 3 回 関西電気化学研究会, 大阪, 12 月 (2025).

[5] 濵田丈翔, 後藤佑太朗, 柴田大輔, 入澤明典, 鐘承超, 下田景士, 岡崎健一, 折笠有基: 高濃度 LiFSI 電解液を用いたグラファイト負極の高温安定性に及ぼす影響とその機構解析, 2025 年度 第 3 回 関西電気化学研究会, 大阪, 12 月 (2025).

[6] 家路豊成, 朝倉清高: Cl K 吸収端 XAFS スペクトルのエッジシフトの要因, 第 39 回日本放射光学会年会・放射光科学合同シンポジウム, 仙台, 1 月 (2026).

[7] 阿部貴人, 小野寺陽平, 小原真司, 手跡雄太, 増野敦信, 梶原大意, 桑村直人, 廣津昌和, 清水俊介, 吉井丈晴, 大倉利典, 橋本英樹: 非晶質ジルコニアの構造と助触媒への応用, 日本セラミックス協会 2026 年年会, 横浜, 3 月 (2026).

[8] 濵田丈翔, 後藤佑太朗, 柴田大輔, 入澤明典, 鐘承超, 下田景士, 岡崎健一, 折笠有基: 高濃度電解液を用いたグラファイト負極の高温耐久化特性と反応メカニズム解析, 電気化学会第 93 回大会, 野田, 3 月 (2026).

[9] 石川和花, 家路豊成, 下田景士, 岡崎健一, 鐘承超, 折笠有基: 固体電解質および液体電解質を用いたマイクロサイズシリコン負極の充放電挙動, 電気化学会第 93 回大会, 野田, 3 月 (2026).

BL-15

Papers

[1] T. Adachi, H. Imamura, T. Yaji, K. Mochizuki, W. Zhu, S. Shindo, S. Shibata, K. Adachi, T. Yamamoto, F. Oseko, O. Mazda, K. Miura, T. Kawai, G. Pezzotti: Spectroscopic Analysis of the Extracellular Matrix in Naked Mole-Rat Temporomandibular Joints, Gels, **11** (2025) 414.

[2] T. Kawasaki, H. Zen, K. Nogami, K. Hayakawa, T. Sakai, Y. Hayakawa: Direct Analysis of Solid-Phase Carbohydrate Polymers by Infrared Multiphoton Dissociation Reaction Combined with Synchrotron Radiation Infrared Microscopy and Electrospray Ionization Mass Spectrometry, Polymers, **17** (2025) 2273.

International Meeting

[1] Tetsuya Adachi, Kentaro Mochizukic, Toyonari Yaji, Keiji Adachi, Toshiro Yamamoto, Fumishige Oseko, Osam Mazda, Shunichi Shibatae, Kyoko Miura, Wenliang Zhu, Giuseppe Pezzotti: Elucidation of aging resistance in the extremely long-lived naked mole-rats, The 33rd Annual Meeting of The Society for Hard Tissue Regenerative Biology (The 8th Asian Science Seminar in TAIWAN), Taichung, August (2025).

Domestic Meeting

[1] 足立哲也, 望月健太郎, 家路豊成, 足立圭司, 山本俊郎, 大迫文重, 松田修, 柴田俊一, 三浦恭子, 朱文亮, Giuseppe Pezzotti: 超長寿ハダカデバネズミの顎関節における老化耐性の解明, 日本バイオマテリアル学会関西ブロック 第20回若手研究発表会, 枚方, 8月 (2025).

[2] 足立哲也: ラマン分光法とケモメトリックスを組み合わせた生体組織および病原体の解析, 第67回歯科基礎医学会学術大会, 北九州, 9月 (2025).

[3] 足立哲也, 柴田俊一: 老化耐性モデルを用いた顎関節の分子構造解析, 第67回歯科基礎医学会学術大会, 北九州, 9月 (2025).

[4] 足立哲也, 望月健太郎, 足立圭司, 山本俊郎, 大迫文重, 松田修, 朱文亮: 超長寿動物モデルを用いた顎関節の分子構造解析, 第15回4大学連携研究フォーラム, 京都, 11月 (2025).

[5] 足立哲也, 家路豊成, 足立圭司, 山本俊郎, 大迫文重, 松田修, 柴田俊一, 三浦恭子, 朱文亮, Giuseppe Pezzotti: データ駆動型分析を導入した超長寿ハダカデバネズミにおける老化耐性の解明, 第4回細胞シート工学イノベーションフォーラム, 東京, 11月 (2025).

[6] 足立哲也, 足立圭司, 金村成智, 山本俊郎, 大迫文重, 進藤智: 老化耐性モデルを用いた口腔組織の分子構造解析, 日本歯科保存学会2025年度秋季大会 (第163回), 長崎, 11月 (2025).

SA-1

Domestic Meeting

[1] 櫛原岳杜, 宮崎徹也, 中田惟奈, 安田耕大, 宮崎友輔, 大岩郁弥, 松本陽広, 水田幸希, 関山明, 藤原秀紀, 野末悟郎, 濱本論, 山崎篤志, 東谷篤志, 玉作賢治, 矢橋牧名, 石川哲也, 入澤明典, 今田真: $Fe_{82}Ga_{18}$ 単結晶の磁場中硬 X 線光電子分光による価電子帯および内殻光電子スペクトルの観測, 日本物理学会第80回年次大会, 東広島, 9月 (2025).

[2] 松本陽広, 櫛原岳杜, 大岩郁弥, 水田幸希, 尹偉達, 宮川正人, 梅津理恵, 入澤明典, 中田惟奈, 今田真: 焼結体(CrFe)S の硬軟 X 線光電子分光, 日本物理学会第80回年次大会, 東広島, 9月 (2025).

[3] 宮浦優希, 下田景士, 鐘承超, 岡崎健一, 折笠有基: 準固体電池におけるモデル系酸化物固体電解質–液体電解質界面の抵抗解析, 第66回電池討論会, 11月 (2025).

[4] 塩見優太, 下田景士, 鐘承超, 岡崎健一, 袖山慶太郎, 岡弘樹, 山田裕貴, 折笠有基: リン酸エステル溶媒による NCM 正極高温充放電耐久性向上機構の解析, 第66回電池討論会, 11月 (2025).

[5] 塩見優太, 下田景士, 鐘承超, 岡崎健一, 袖山慶太郎, 岡弘樹, 山田裕貴, 折笠有基: リン酸エステル溶媒による NCM 正極の高温充放電安定性に及ぼす影響とその機構解析, 2025年度 第3回 関西電気化学研究会, 12月 (2025).

[6] 宮浦優希, 下田景士, 鐘承超, 岡崎健一, 折笠有基: 複合電解質およびそのモデル系における固体電解質–液体電解質界面でのリチウムイオン輸送解析, 電気化学会第93回大会, 3月 (2026).

International Meeting

[1] K. Sakamoto: Electronic structure of a nitride superconductor TiN thin film, TJ-CGAC 2025, 台湾 新竹市, May (2025).

AWARDS

[1] 学生講演賞
中村雅史(京都大学大学院理学研究科): X線分光と第一原理計算による多元素合金触媒の電子構造–物性相関の定量評価, 日本化学会第105春季年会, 4月 (2025).

[2] 日本XAFS研究会学生奨励賞
東亜紗花(立命館大学生命科学研究科): シリカ担持酸化マンガンの昇温脱酸素過程の in situ XAFS 解析, 日本XAFS研究会, 9月 (2025).

[3] Springer-Nature Best Presentation Award
越智杏奈(立命館大学生命科学部): Characterization of membrane-encapsulated selenium nanoparticles and their membrane-dependent export by *Escherichia coli*, ISSBM 13, 10月 (2025).

[4] 関西電気化学奨励賞
濵田丈翔(立命館大学生命科学研究科): 高濃度 LiFSI 電解液を用いたグラファイト負極の高温安定性に及ぼす影響とその機構解析, 電気化学会関西支部, 12月 (2025).

[5] 関西電気化学奨励賞
塩見優太(立命館大学生命科学研究科): リン酸エステル溶媒による NCM 正極の高温充放電安定性に及ぼす影響とその機構解析, 電気化学会関西支部, 12月 (2025).

[6] Oral presentation award
後藤祐太朗(立命館大学生命科学研究科): Analysis of Solid Electrolyte Interphase in Lithium Metal Battery Anode at Elevated Temperatures, International Conference on Green Hydrogen and Energy Technology, ICGHET 2026, 1月 (2026).

[7] Poster award
塩見優太(立命館大学生命科学研究科): Analysis of the High-Temperature Charge–Discharge Durability Mechanism of NCM Cathodes using Phosphate Ester Electrolytes, International Conference on Green Hydrogen and Energy Technology, ICGHET 2026, 1月 (2026).

[8] 優秀学生講演賞
石川和花(立命館大学生命科学研究科): 固体電解質および液体電解質を用いたマイクロサイズシリコン負極の充放電挙動, 電気化学会第93回大会, 3月 (2026).

ACADEMIC DEGREES

博士(Doctor)

博士(理学) 柴田 大輔(立命館大学)	蛍光軟 X 線吸収分光における自己吸収補正手法の開発と電池材料への応用
D. Sc. Daisuke SHIBATA (Ritsumeikan Univ.)	A Development of Self-Absorption Correction Technique in Fluorescence Soft X-ray Absorption Spectroscopy and Its Application to Battery Materials

修士(Master)

修士(理学) 荒木 一慶 (立命館大学)	紫外光照射による多層カーボンナノチューブ表面の電子状態変化
M. Sc. Ikkei ARAKI (Ritsumeikan Univ.)	Surface electronic changes of multi-walled carbon nanotubes induced by ultraviolet irradiation
修士(理学) 會野 陽平 (立命館大学)	Ar$^+$スパッタリング SrTiO$_3$ 上 Pentacene の分子配向分析
M. Sc. Yohei KAINO (Ritsumeikan Univ.)	Molecular orientation analysis of pentacene on Ar$^+$-sputtered SrTiO$_3$ surfaces
修士(理学) 堀 凜太郎 (立命館大学)	TiO$_2$(110)上に蒸着したペンタセンの分子配向への蒸着速度の影響
M. Sc. Rintaro HORI (Ritsumeikan Univ.)	Effect of deposition rate on molecular orientation of pentacene deposited on TiO$_2$(110)
修士(理学)　櫛原 岳杜 (立命館大学)	硬 X 線光電子分光による Fe$_{82}$Ga$_{18}$磁歪合金単結晶の電子状態の解明
M. Sc. Gakuto KUSHIHARA (Ritsumeikan Univ.)	Electronic States of Magnetostriction Alloy Fe$_{82}$Ga$_{18}$ Single Crystal Studied by Hard X-ray Photoemission
修士(理学)　中谷 優心 (立命館大学)	Sn とその硫化物の電子状態の研究
M. Sc. Yushin NAKATANI (Ritsumeikan Univ.)	Electronic States of Sn and Sulfides
修士(理学)　松本 陽広 (立命館大学)	焼結体(Cr,Fe)S の硬軟 X 線光電子分光と X 線吸収分光
M. Sc. Haruhiro MATSUMOTO (Ritsumeikan Univ.)	Hard and Soft X-ray Photoemission and X-ray Photoabsorption of Sintered (Cr,Fe)S
修士 (工学) 東 亜紗花 (立命館大学)	シリカ担持酸化マンガン触媒の昇温脱酸素過程の化学状態解析
M. Eng. Asaka AZUMA (Ritsumeikan Univ.)	Chemical State Analysis for Deoxygenation Process of Manganese(IV) Oxide Supported on Silica
修士 (工学) 鵜飼 隼也人 (立命館大学)	八面体型酸化銅(I)粒子の還元過程における粒子内反応分布の顕微 XAFS 解析
M. Eng. Hayato UKAI (Ritsumeikan Univ.)	Micro XAFS Analysis of Chemical State Inhomogeneity for Reduction Process of Octahedral Cu$_2$O Particle

修士 (工学) 川口 綾香 (立命館大学)	炭素担持酸化ニッケル電極の電気化学的コンバージョン過程の状態解析
M. Eng. Ayaka KAWAGUCHI (Ritsumeikan Univ.)	Chemical State Analysis for Electrochemical Conversion Processes of Nickel Oxide Supported on Carbon
修士 (工学) 柴田 壮士郎 (立命館大学)	Persistent Homology による ZnO 電極の反応分布解析
M. Eng. Sojiro SHIBATA (Ritsumeikan Univ.)	Analysis of Reaction Distribution of ZnO Electrode via Persistent Homology
修士 (工学) 高野 雅也 (立命館大学)	水系亜鉛負極電池における電極反応の不均一性の解析
M. Eng. Masaya TAKANO (Ritsumeikan Univ.)	Analysis of Inhomogeneity in Electrode Reactions in Aqueous Zinc Anode Battery
修士 (工学) 樋口 歩未 (立命館大学)	担持酸化バナジウムの昇温酸化還元過程の化学状態解析
M. Eng. Ayumi HIGUCHI (Ritsumeikan Univ.)	Chemical State Analysis for Redox Processes of Supported Vanadium Oxide
修士 (工学) 深田 恵子 (立命館大学)	炭素担持酸化マンガンの電気化学的コンバージョン過程の状態解析
M. Eng. Keiko FUKADA (Ritsumeikan Univ.)	Chemical State Analysis for Electrochemical Conversion Processes of Manganese Oxide Supported on Carbon
修士 (工学) 石黒 雄大 (立命館大学)	オペランド蛍光 X 線分光法によるセリウムイオンラジカルクエンチャーの膜直方向移動パラメータの算出
M. Eng. Yuta ISHIGURO (Ritsumeikan Univ.)	Determination of Through-Plane Migration Parameters of Cerium Ion Radical Quenchers by Operando X-ray Fluorescence Spectroscopy
修士 (工学) 加藤 愛理 (立命館大学)	フッ化物イオンキャリアーを用いた二次電池材料の解析
M. Eng. Airi KATO (Ritsumeikan Univ.)	Analysis of Secondary Battery Materials Using a Fluoride Ion Carrier
修士 (工学) 後藤 佑太朗 (立命館大学)	高温環境下におけるリチウム析出溶解反応後の銅集電体被膜解析
M. Eng. Yutaro GOTO (Ritsumeikan Univ.)	Analysis of Copper Current Collector Coatings after Lithium Deposition/Dissolution Reactions under High-Temperature Conditions
修士 (工学) 正躰 剛成 (立命館大学)	新規フッ化硫化物 $LaBaF_3S$ の合成とフッ化物イオン伝導性評価
M. Eng. Takanari SHOTAI (Ritsumeikan Univ.)	Synthesis of Novel Fluoride Sulfide $LaBaF_3S$ and Evaluation of Its Fluoride Ion Conductivity

修士 (工学) 花原 瑠希也 (立命館大学)	オペランド XRF による CeO_2 ラジカルクエンチャーの溶解挙動解析
M. Eng. Rukiya HANAHARA (Ritsumeikan Univ.)	Analysis of the Dissolution Behavior of CeO_2 Radical Quenchers by Operando XRF
修士 (工学) 平井 進次郎 (立命館大学)	$Ln_{1-x}Ba_{2+x}F_{3-x}S_2$ (Ln = ランタノイド)の結晶構造解析とイオン伝導率評価
M. Eng. Shinjiro HIRAI (Ritsumeikan Univ.)	Crystal Structure Analysis and Ionic Conductivity Evaluation of $Ln_{1-x}Ba_{2+x}F_{3-x}S_2$ (Ln = Lanthanoid)
修士 (工学) 平林 慶 (立命館大学)	X 線 CT 法を用いた炭素負極へのアルカリ金属イオン挿入に伴う粒子形態変化の解析
M. Eng. Kei HIRABAYASHI (Ritsumeikan Univ.)	Analysis of Particle Morphology Changes Associated with Alkali Metal Ion Insertion into Carbon Negative Electrodes Using X-ray CT
修士 (工学) LIU Shixuan (立命館大学)	孤立電子対導入がフッ化硫化物 $LaSr_2F_3S_2$ の結晶構造と導電率に与える影響
M. Eng. Shixuan LIU (Ritsumeikan Univ.)	Effect of Lone-Pair Electron Introduction on the Crystal Structure and Conductivity of Fluoride Sulfide $LaSr_2F_3S_2$
修士 (工学) 宮城 翔 (立命館大学)	全固体リチウムイオン電池を用いたコンバージョン型正極材料 $AgCuF_3$ の特性評価
M. Eng. Sho MIYAGI (Ritsumeikan Univ.)	Characterization of the Conversion-Type Cathode Material $AgCuF_3$ Using All-Solid-State Lithium-Ion Batteries

---

MEMOIRS OF THE SR CENTER
RITSUMEIKAN UNIVERSITY
No. 28, Jun 2026

Publisher THE SR CENTER, RITSUMEIKAN UNIVERSITY
Director Kiyotaka Asakura

Address 1-1-1, Noji-Higashi, Kusatsu, Shiga 525-8577, Japan
Tel:+81-77-561-2802 Fax:+81-77-561-2811
E-mail:sr1@st.ritsumei.ac.jp
URL:http://www.ritsumei.ac.jp/acd/re/src

Printing house HOKUTO PRINT CO.,LTD
Address 38-2, Shimogamotakagicho
Sakyoku, Kyoto 606-8540, Japan

立命館大学 SRセンター

滋賀県草津市野路東1-1-1